The origin of stilpnomelane lutite layers in Banded Iron Formations from the West Transvaal Basin, South Africa

A.R.W. (Aart) van der Waal[1]

[1] *Faculty of Earth Sciences, Utrecht University, Budapestlaan 4, 3584 CD Utrecht, The Netherlands.*

Master Thesis in Earth Sciences

First Supervisor: dr. P.R.D. (Paul) Mason, Utrecht University

Second Supervisor: dr. H. (Harilaos) Tsikos, Rhodes University, South Africa

Abstract

Banded iron formations (BIFs) provide a record of chemical changes in the oceans during the first accumulation of atmospheric oxygen during the Paleoproterozoic great oxygenation event (GOE). They frequently contain cm- to m-scale shaly intervals called stilpnomelane lutites that are of poorly constrained origin. Various hypotheses exist to explain their genesis, including: volcanism, sea-level variations and biological processes. In this study, I investigated the origin of lutites from the ~2.43 Ga Griquatown BIF in the Western Transvaal Basin, South Africa using samples obtained from drill cores. I conducted chemical analysis of bulk rock samples involving major- and trace element XRF and ICP-MS measurements, mineralogical XRD measurements, (in)organic carbon and quadruple sulphur isotope analysis. The main mineralogy of stilpnomelane lutite consists of stilpnomelane, biotite, magnetite, quartz, siderite, ankerite and pyrite as well as various minor mineral phases. The samples are composed mainly of SiO_2 and Fe_2O_3 (60-90 wt%) with lesser amounts of Al_2O_3, MgO, CaO and K_2O. Shale normalized rare earth element and yttrium (REY) plots lack strong La and Ce anomalies while Eu anomalies vary. Large variability was also observed for the degree of LREE enrichment. The fluctuation in REY depends strongly on the mixing of the marine component with a felsic component. Trace element variability indicated that this component originates from distal felsic volcanism and that it represents ash fall following episodic eruptions. Quadruple sulphur isotope analysis, together with total organic carbon (TOC) contents, showed that microbial sulphate reduction was also influencing the deposition of stilpnomelane lutites. An increase of $\delta^{34}S$ with decreasing age indicates that deposition occurred in a closed basin with Rayleigh fractionation governing the isotopic composition of sulphur. Mass independent fractionation (MIF) of sulphur isotopes indicate that the entire Griquatown BIF was deposited during the onset of the GOE when sulphur MIF continued to be produced or recycled in near-surface environments. Furthermore, variations in sulphur MIF slopes reveal temporal changes in Archean atmospheric chemistry.

Utrecht University

I: Table of Contents

II: Introduction

Introduction to Banded Iron Formations

Banded iron formations (BIF) are sedimentary deposits which are globally distributed. They consist of alternating bands of iron-rich (20-50 wt% Fe) and iron poor, Si rich, mineral layers (40-50 wt% SiO_2; Posth et al., 2011). The major BIFs are found in South Africa (Transvaal Supergroup), Australia (Hamersley Group), North America (Labrador, Lake Superior, Gunflint and Biwabik IFs), Ukraine (Krivoy Rog Supergroup), Greenland (Isua Greenstone Belt) and Brazil (Carajas Formation and Urucum region; Klein, 2005). BIFs were mainly deposited throughout the Archean and Paleoproterozoic with a small re-emergence during the Neoproterozoic (Fig. 1). They can be categorized in two types based on their depositional environment, the Algoma and Superior type BIF. Algoma types are generally small and are thought to be related to volcanic activity. Superior type BIF have a vast lateral extent and can be hundreds of metres thick (e.g. Hamersley and Transvaal BIF; Posth et al., 2011). The deposition of this type of BIF is thought to have taken place in shelf-like environments without clear indicators of large scale influence of volcanic processes. The different types of BIF also show a temporal evolution as the Early- and Mid-Archean BIFs as well as Neoproterozoic ones tend to be of the Algoma type, while those of the Neo-Archean and Paleoproterozoic tend to be of Superior type (Beukes and Gutzmer, 2008).

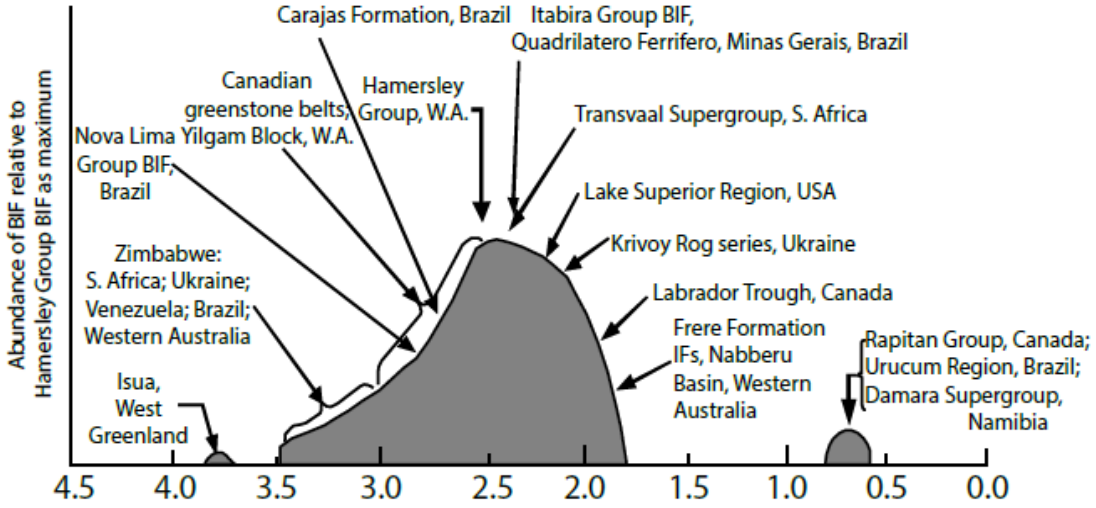

Figure 1: Schematic of the temporal evolution of BIF deposition (redrawn from: Klein, 2005).

While BIFs have been dated as far back as 3.8 Ga, the Isua Greenstone Belt in Greenland, a major peak in BIF deposition occurred around 2.6-2.4 Ga (Fig. 1; e.g. Klein, 2005; Beukes and Gutzmer, 2008). During this period extensive iron formations were deposited. Between 2.4 and 1.8 Ga the amount of BIF deposition decreased, however many smaller scale Algoma and Superior type deposits are present (Bekker et al., 2014). BIF formation halted around 1.8 Ga after which barely any BIFs were deposited for nearly 1 Gyr. The exact reason for the cessation of BIF deposition is not constrained yet, but various hypotheses exist. These include an oxygenated deep ocean (Holland, 1984), a sulphidic deep ocean (Canfield, 1998), mixing of shallow and deep ocean waters as a result of a meteorite impact (Slack and Cannon, 2009) and variability in ocean redox state while it still remained more reducing than the Phanerozoic oceans (Planavsky et al., 2011). Around 750 Ma BIFs reappeared, which has been related to over-active oxygenic photosynthesis which is in turn held responsible for the occurrence of at least three Snowball Earth events (Stern et al., 2006). During these Snowball Earths the oceans were covered by thick ice sheets, meaning they could not interact with the oxygenated atmosphere. This resulted in a gradual reduction of the oxidation potential of the oceans until eventually the oceans became reducing again, allowing ferrous iron to accumulate in ocean waters. With melting ice sheets the oceans became once again able to interact with the atmosphere and the increasing oxidation levels of the oceans resulted in the deposition of BIFs (Stern

et al., 2006). Aside from these BIFs related to Snowball Earth events, no large scale iron formation deposits have been reported since the Paleoproterozoic around 1.8 Ga.

In this study I will focus on the approximately 2.4 Gy old Griquatown Iron Formation, which is part of the Transvaal Supergroup in South Africa. The Griquatown BIF is an approximately 200m thick sequence that forms a part of the Asbestos Hills subgroup in the Ghaap Group of the Transvaal Supergroup in South Africa where it overlies the Kuruman BIF and is overlain by the Makganyene diamictite of the Postmasburg Group (Fig. 2; Beukes, 1984). The contact between the Makganyene diamictite and Griquatown BIF is still under investigation. The Griquatown BIF consists of the Danielskuil, Skietfontein and Pietersberg members (Beukes, 1984). The age close to the base of the Griquatown BIF has been determined to be 2432±31 yr based on U/Pb ages from zircons (Mapeo et al., 2006). It is impossible to infer an age at the top of the Griquatown BIF, the transition to the Makganyene diamictite is unclear and there are no minerals present that allow for age determination. This diamictite is thought to be the remnant of an Archean Snowball Earth event, the Huronian Glaciation (Kopp et al., 2005). While it is impossible to get an accurate estimate of the age of the top of the Griquatown BIF, we can look at the order of magnitude of time that has passed during deposition of the Griquatown BIF based on the age of the layers overlying the Makganyene diamictite. The Ongeluk Lava directly overlying the diamictite has been dated by zircons and baddleyite in the sub-volcanic sills, yielding an age of approximately 2.43 Ga (Gumsley et al., 2015). High up in the stratigraphy we find the Mooidraai dolomite which has been dated to 2394±26Ma (Bau et al., 1999). This small window of time between the Ongeluk Lava and the zircons found near the base of the Griquatown BIF indicates that the deposition of the BIF occurred on a relatively short time-scale.

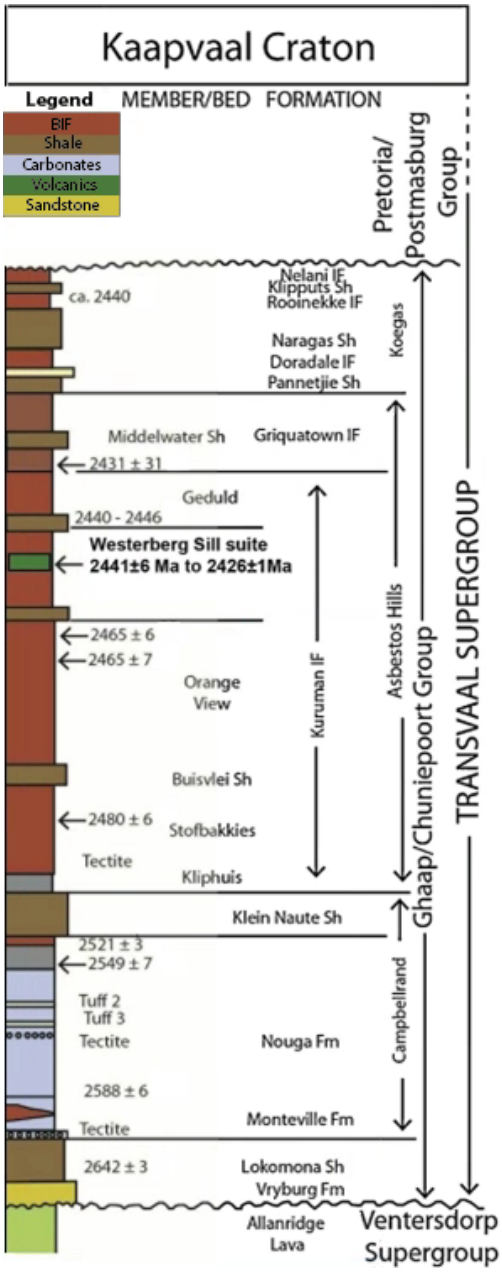

Figure 2: Stratigraphic representation of the Transvaal Supergroup (edited from Kampmann et al. (2015)).

<u>The Deposition of Banded Iron Formations</u>

The deposition of BIFs relies on the oxidation of Fe(II) to Fe(III) somewhere in the water column. The source of the Fe(II) in the Archean ocean has been constrained as being mainly hydrothermal, based on the positive Eu anomaly in REE data (Bolhar et al., 2005). The Fe(II) supplied by hydrothermal vents was not removed due to (1) low sulphide and sulphate concentrations in the Archean ocean (Habicht et al., 2002) and (2) the atmosphere lacking sufficient oxidation potential to produce Fe(III). The inability of the Archean system to oxidise Fe(II) to Fe(III) resulted in a ferruginous ocean (Bekker et al., 2004). To deposit the BIFs an oxidative potential will have to be generated to oxidise the iron. The processes that govern the deposition of BIFs are still not fully understood and four major hypotheses exist to explain BIF deposition.

The first hypothesis is that the formation of BIFs is a response to the initiation of a rapid, global, rise in atmospheric oxygen, the Great Oxygenation Event (GOE; Bekker et al., 2004). This is based on the fact that there is a large increase in BIF deposition around 2.5-2.4 Ga which is roughly coeval with the GOE, dated between 2.45 and 2.32 Ga (Farquhar et al., 2011). This available free oxygen would be

able to oxidise the upper layers, thereby oxidising the Fe(II) to insoluble Fe(III). This would be possible by a combination of Fe-cycling in the oceans supplying the surface layers with Fe(II) and the increasing vertical extent of the oxidised surface layer in the Paleoproterozoic ocean. This means that the post-GOE BIFs are enriched in hematite compared to the pre-GOE ones as there is an increased availability of ferric iron (Bekker et al., 2014). The large amount of pre-GOE BIF deposition implies that there must have been sufficient oxygen production to precipitate BIFs before oxygen could accumulate in the atmosphere. The consensus is that the oxygen responsible for the pre-GOE deposition of BIFs was the result of anoxygenic photosynthesis (Bekker et al., 2014). For some pre-GOE BIFs there have been studies regarding the oxidation mechanisms of the Fe (e.g. Anbar et al., 2007). These studies show temporary local increases in O_2 which are traced using isotopic variations in redox-sensitive elements and they have been found at 2.7 Ga and as far back as 3.0 Ga (Anbar et al., 2007; Crowe et al., 2013). Rising O_2-levels are accompanied by increases in organic carbon concentrations, indicating that there is a microbial source for the pre-GOE oxygen.

Prior to the GOE, the atmosphere contained very little oxygen, with atmospheric oxygen concentrations less than 10^{-5} times that of present atmospheric levels (PAL; Pavlov and Kasting, 2002). This meant that there was insufficient oxygen to generate an ozone layer which allowed UV radiation to reach the surface of the Earth without any obstruction. The energy of the UV radiation should theoretically be sufficient to oxidise the ferrous iron to ferric iron (Anbar and Holland, 1992). Subsequent hydrolysis generated ferric hydroxides which precipitated from the seawater to form the BIFs. This process might have played a significant role, because the oxidation of Fe(II) through UV radiation occurs at wavelengths of 300-450 nm (Bekker et al., 2014). In this wavelength region the sun is more intense and the seawater more transparent compared to other wavelengths. It has been determined that the oxidation rate of Fe(II) by UV-radiation in an anoxic atmosphere is around $0.5 mol \cdot m^{-2} \cdot yr^{-1}$ (Francois, 1986). This flux would be sufficient to provide enough ferric iron to meet the sedimentation rates inferred for the Hamersley basin at 3-4m per Myr (Pickard, 2003), although other authors state that sedimentation rates could be as high as 33m per Myr (Bekker et al., 2014). Furthermore, Konhauser et al. (2007) argue that the effects of photochemical oxidation of ferrous iron are negligible as the dissolved ferrous iron instead forms amorphous mineral phases or siderite in their experiments. This implies that it is possible for Fe(II)-minerals to be deposited on a significant scale during the deposition of the BIFs and that complete oxidation to Fe(III) minerals is not required for BIF deposition.

Another hypothesis is that, since the majority of the ferrous iron supplied to the Archean oceans was supplied by hydrothermal vents, the genesis of BIFs can be directly related to periods of enhanced mantle plume activity (Isley and Abbott, 1999). They used geochronology to link the timing of mantle plume events with those of BIF deposition and found that there is a significant correlation between the two of them. It has been suggested that this correlation exists because enhanced plume activity would be accompanied by enhanced hydrothermal activity, which would supply more Fe(II) to the oceans and provide favourable conditions for BIF deposition as ferrous iron concentrations increase (Isley and Abbott, 1999; Bekker et al., 2010).

Other authors advocate that the main cause for the oxidation of the surface layers of the ocean and subsequent oxidation of Fe(II) to Fe(III) were microorganisms instead of abiotic processes (e.g. Beukes, 1984; Konhauser et al., 2002). The oxidation rates for Fe(II) generated by microbes in low-oxygen systems can be up to 50 time faster than the oxidation rates found for abiotic processes. There are three pathways for microorganisms to be capable of iron oxidation: photosynthesis, metabolic oxidation and anoxygenic phototrophy (Posth et al., 2008; Bekker et al., 2014). The presence of oxygen producing photosynthetic microorganisms would result oxygen production, which would oxygenate the surface layers of the Archean ocean and thereby oxidise the ferruginous iron to ferric iron. The type of organism that would produce this oxygen would most likely be photosynthetic cyanobacteria (Scott et al., 2011). However, there has been no conclusive evidence to

advocate for the evolution of these organisms at the times the BIFs were deposited as the evidence provided could also be the result of contamination (Brocks, 2011).

Metabolic iron oxidation can take place in three different manners depending on the available reducing agents. The reducing agent can be either CO_2 during microaerophilic (Eq. 1) and anoxygenic photosynthetic (Eq. 2) or NO_3^- during nitrate-dependent Fe(II) oxidation (Eq. 3; Bekker et al., 2014).

$$6Fe(II) + 0.5O_2 + CO_2 + 16H_2O \leftrightarrow [CH_2O] + 6Fe(OH)_3 + 12H^+ \quad \text{(Eq. 1)}$$

$$4Fe(II) + CO_2 + 11H_2O \leftrightarrow [CH_2O] + 4Fe(OH)_3 + 8H^+ \quad \text{(Eq. 2)}$$

$$10Fe(II) + 2NO_3^- + 24H_2O \rightarrow 10Fe(OH)_3 + N_2 + 18H^+ \quad \text{(Eq. 3)}$$

The different pathways all rely on a similar reaction where Fe(II) is oxidised to Fe(III) and subsequently hydrolysed to form ferric hydroxide. However, a complication for NO_3^--dependent oxidation is that multiple types of microbes are required (Bekker et al., 2014; Posth et al., 2014). The remnants of microbially mediated Fe-oxidation have been widely reported in Proterozoic BIFs, but not yet in Archean BIFs (Bekker et al., 2014). However, based on the REE patterns for Archean BIFs it is likely that, if metabolic Fe(II) oxidizing microbes are present, they are either anoxic or microaerophilic (Planavsky et al., 2010).

The presence of Fe(II)-oxidizing photoautotrophs could have also supplied the ferric iron to the oceans . These microorganisms will oxidise Fe(II) while reducing dissolved bicarbonate under the influence of light (Eq. 4; Posth et al., 2008).

$$4Fe(II) + HCO_3^- + 10H_2O + hv \rightarrow 4Fe(OH)_3 + [CH_2O] + 7H^+ \quad \text{(Eq. 4)}$$

Experimental results have shown that these organisms thrive in conditions which mimic Archean oceanic composition and conditions. It was found that, by varying the temperature, these organisms are capable of forming biogenic Fe(III)-minerals that will be deposited in Fe-rich layers (Posth et al., 2008). This occurs at temperatures between 20 and 55°C. For temperatures below 20°C these microbes become inactive and there will be no large scale biotic iron oxidation, instead there will be deposition of Si-rich layers (Posth et al., 2008). Therefore they argue that the seasonal variations in seawater temperature could explain the formation of BIFs as well as their banding.

Banded Iron Formations: Mineralogy and Metamorphism

The present-day BIFs contain a vast array of Fe-rich minerals such as Fe-oxides (magnetite and hematite), Fe-silicates (riebeckite, minnesotaite, clinochlore and stilpnomelane) and Fe-carbonates (siderite and ankerite; Table 1). The siliceous bands contain mainly chert and minor Fe-hosting minerals. There are also traces of sulphate and phosphate minerals such as pyrite, apatite and monazite (Webb et al., 2003; Bekker et al., 2014). Most of these minerals are thought to be secondary minerals. As such they did not form upon deposition, but instead they have formed during diagenesis or metamorphic events. The primary BIF mineralogy has not been established with certainty. However, they are thought to be ferric (oxy)hydroxides such as goethite and green rusts. These green rusts are a mixture of large amounts of different Fe-oxyhydroxides with different Fe(II) and Fe(III) abundances (Beukes and Gutzmer, 2008). Other authors also argue for primary deposition of siderite and greenalite (e.g. Klein, 2005; Raiswell et al., 2011; Posth et al., 2014). During early diagenesis these Fe-hydroxides would react to form magnetite and hematite. During later stages of diagenesis the greenalite would react to form the low PT Fe-silicates like minnesotaite, riebeckite and stilpnomelane.

Mineral	Chemical Composition
Magnetite	Fe_3O_4
Hematite	Fe_2O_3
Goethite	FeOOH
Minnesotaite	$Fe_3Si_4O_{10}(OH)_2$
Siderite	$FeCO_3$
Ankerite	$CaFe(CO_3)_2$
Stilpnomelane	$K_5Fe^{2+}{}_{33}Mg_{15}Si_{64}Al_8O_{168}(OH)_{45}\cdot 12H_2O$
Riebeckite	$Na_2Fe^{2+}{}_3Fe^{3+}{}_2SiO_8O_{22}(OH)_2$
Clinochlore	$Fe_2Mg_3Al_2Si_3O_{10}(OH)_8$

Table 1: Chemical composition of the main Fe-bearing minerals found in BIFs. Compositions from Webb et al. (2003).

Figure 3: The evolution of the major mineral assemblage of BIFs during diagenesis and metamorphism (Klein, 2005).

Using Ge/Si ratios it has been shown that the Fe and Si in BIFs have separate sources (Hamade et al., 2003). Posth et al. (2008) advocate for changes in microbial activity to supply the silica. Another explanation is that the silica became adsorbed onto the surfaces of the Fe-hydroxides as a result of organic matter scavenging of silica from the Archean Si-saturated oceans (Maliva et al., 2005). They argue that the dissolved Si(IV) gets adsorbed onto the Fe-hydroxides as the dissolved Fe(II) in the surface layers of the ocean is oxidised. The oxidation causes ferric oxyhydroxide particles to form and sink through the water column. As they sink through the water column, the dissolved Si adsorbs to the surface. When the Fe-oxyhydroxide particles reach the reducing bottom layers of the ocean. As the Fe-particles are reduced, the Si will be desorbed and concentrated in the pore space (Fischer and Knoll, 2009). Subsequent diagenetic processes will liberate the Si from the pore space and allow it to form chert layers. Post-depositional metamorphism will result in the formation of Fe-carbonates and various Fe-silicates (Bekker et al., 2014).

For the Griquatown BIF, the lower Skietfontein and Danielskuil members consist mainly of siderite and greenalite lutites. The upper Pieterberg member contains chert-banded greenalite lutites (Beukes, 1984). Based on the mineralogy it was concluded that there has been at least one low-grade metamorphic event with little to no deformation between 2357 and 2239 Ma (Beukes and Klein, 1990). The evolution of BIF mineralogy is highly variable depending on the PT conditions during metamorphism (Fig. 3). For drill core CN-109 (Fig. 6) which was sampled close to the sampling location, approximately 50 km northwest of the town of Kuruman, the major minerals found were: chert, magnetite, ankerite, siderite, riebeckite, stilpnomelane and minnesotaite (Miyano and Beukes, 1984). Based on this assemblage it was concluded that there were late diagenetic to low grade metamorphic conditions with temperatures of at most 170°C and pressures below 2kbar for the Griquatown formation, reflecting late diagenetic to low-grade metamorphic conditions (Beukes and Klein, 1990; Fig. 3). The Griquatown BIF also contains granules which are mainly made up of Fe-silicate and Fe-carbonate minerals, wherein Fe-oxides are almost absent (Beukes and Klein, 1990).

Bekker et al. (2014) compared the granules from the Griquatown BIF with those of post-GOE BIFs where the granules are predominantly hematitic or hematite coated. They argue that a change in the composition of the granules advocates for a different depositional model for pre-GOE BIFs compared to post-GOE BIFs.

Stilpnomelane Lutites

The vast majority of the BIF sequence is made up of layers of iron-rich material interbedded with silica rich chert layers. However, there are also some layers within BIFs that do not consist of either of the two main components these are the black shale or stilpnomelane lutite layers. These layers were first noted in the earliest BIF studies, but were ignored as they comprised only a few thin layers in vast iron formations. The stilpnomelane lutite layers themselves are often of a cm- or sub-cm scale. However, within the Griquatown BIF three larger m-thick stilpnomelane lutite intervals have been identified (Fig. 5). A first detailed description was given by Beukes (1984) who investigated them in the Transvaal Supergroup and dubbed the layers stilpnomelane lutite based on their mineral assemblage. These beds have a relatively high SiO_2 content of 25-55% and also contain significant total iron ($Fe_2O_3^T$ = 20-50%; This study). Carbonate rich stilpnomelane lutite samples contain a large LOI fraction, up to 15 wt%, which is made up of sulphur and carbon of which stilpnomelane lutites can contain significant amounts of carbon (up to 8 wt%) and sulphur (up to 12 wt%) (Beukes and Gutzmer, 2008; This study). Beukes (1984) found that there is a cyclicity in the deposition of stilpnomelane lutite layers (Fig. 4). Following the deposition of the stilpnomelane lutite, the Si concentration first increases and subsequently decreases steadily until another stilpnomelane lutite layer is deposited. Mineral assemblage studies of the stilpnomelane lutite beds show that there are cuspate mineral shards and K-feldspar present in the beds (Beukes, 1984). A more detailed mineral assemblage was given by Webb et al. (2003) who concluded that the major components were quartz, stilpnomelane and K-feldspar. Minor components were ankerite, siderite, clinochlore, biotite and pyrite.

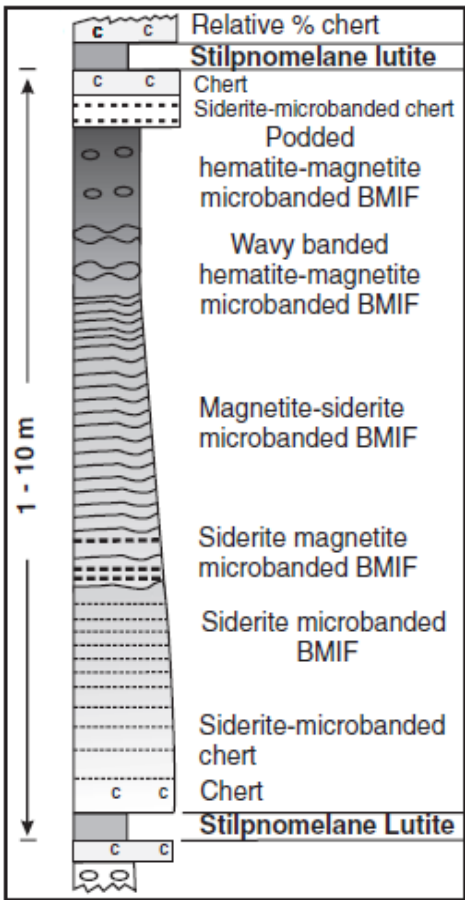

Figure 4: Stilpnomelane Lutite depositional cyclicity. Horizontal axis is relative % chert, not grain size. Edited from Beukes and Gutzmer (2008).

The cyclicity of the shale bands had also been observed in the Hamersley basin in Australia. Here the shale bands are present on a larger scale than in the West Transvaal basin, meaning they are more extensively studied (e.g. Webb et al., 2003; Pickard et al., 2004). Based on the mineralogy and microstructures four different types of shale sub-types were defined; Stilpnomelane-rich mudrocks, stilpnomelane-rich tuffaceous mudrocks, carbonaceous mudrocks and calcareous mudrocks (Pickard et al., 2004). By combining the cyclicity of the lutite deposits with the internal micro-structures of specific stilpnomelane lutites Hassler et al. (2011) were able to link the layers in the Kuruman BIF in South Africa with those of the Dales Gorge member in the Hamersley basin in Australia. This correlation is used to propose that West Transvaal basin and the Hamersley basin were part of a single large basin at the time of BIF deposition (Hassler et al., 2011). This is supported by the stratigraphic successions in both basins where both textural and age correlations have been found (Beukes and Gutzmer, 2008). This has led to the proposal of a supercontinent assembly during the late Archean, Vaalbara (Hassler et al., 2011). On the other hand, paleomagnetic data indicates a break-up of the Vaalbara supercontinent prior to the deposition of the Griquatown IF (de Kock et al.,

2009). However, magnetic overprinting during later orogenic events may have affected paleomagnetic datasets (Kampmann et al., 2015).
The processes that govern the formation of stilpnomelane lutite beds are still uncertain, but there are multiple hypotheses. The first hypothesis was proposed by Beukes (1984) who argued that based on the presence cuspate mineral shards and K-feldspar as well as the lateral continuity and extent of the stilpnomelane lutite beds, a single volcanic event had to be responsible for these layers. He argued that the beds are the result of explosive volcanic eruptions and that they represent the lapilli and volcanic ash deposits. This could also explain the chert layers that over- and underlie the stilpnomelane lutite as their silica enrichment can be explained as extra Si being sourced from a hydrothermal vent during the eruption or the leaching of silica during the devitrification of the ash deposit. The deposition of the stilpnomelane lutite would have taken place below the storm wave base, thus a medium- to deepwater environment. Another hypothesis argues that the presence of volcaniclastics is only an indicator that there is distal volcanic activity that is coeval with the deposition of these layers instead of being the main source of the deposited material (Pickard et al., 2004). They advocate that the sediments will mainly be derived from shelf-sourced material which has been deposited into the deeper parts of the basin through turbidites. In this model the cyclicity is explained as being a result of the accumulation of material during regular BIF deposition. The deposition of stilpnomelane lutite occurs when the amount of accumulated material is sufficient to trigger turbidites. During the time the material is accumulating after a turbidite event, the BIF is deposited.

Krapez et al., (2003) propose two different depositional mechanisms for stilpnomelane lutite beds. Some of these beds contain detrital zircons and are inferred to be turbiditic in origin. Other stilpnomelane lutites do not contain this detrital input and could have settled through the water column as hemipelagites. The deposition of stilpnomelane lutites through turbidites would require the accumulation of material, explaining the cyclicity of their deposition. The stilpnomelane lutites that have settled through the water column will be deposited during the early stages of regression, when the water depth is greatest. This fits well with the absence of detrital material. They contain volcaniclastics due to distal volcanism. Subsequent shallowing would introduce detrital material. This is related to the proximity to a continental sediment supply. During a high sea-level, the shelf is below sea-level and sediment is deposited on the shelf. Without detrital influences, the deposition of the BIF will take place within the basin. On the other hand, during low sea-level the shelf will be exposed and get eroded. This means that the source of the sediment is closer to deeper regions of the basin. With cycles of sea-level rise and fall this will result in cyclic deposits where stilpnomelane lutite beds will be deposited during sea-level highs. This makes it possible to explain the cyclicity using sea-level variations and turbidite events.

While these abiotic processes can explain the deposition of the stilpnomelane lutites, there are also some biological factors that will have to be taken into account. Previous studies (e.g. Anbar et al., 2007) find that the stilpnomelane lutite layers are occasionally enriched in organic carbon, which would imply that there is a significant source of organic carbon production involved in the deposition of these layers. The presence of microbes would require nutrients, in particular trace elements such as V and Mo, to allow for increased nitrogen fixation and thus increased primary productivity (Bekker et al., 2014). They argue that these trace metals would be provided by the volcanic and hydrothermal activity, implying that microbial nutrients and ferrous iron could have the same source.

In this study I will focus on the mineralogical and geochemical characteristics of the stilpnomelane lutite layers found in the Griquatown and Kuruman BIFs of the West Transvaal basin in South Africa. I will look at both major and trace element composition as well as carbon and sulphur content. Furthermore, quadruple sulphur isotope analysis will be used to infer time constraints on the deposition of the Griquatown BIF. By doing this I aim to provide an explanation for the genesis and evolution of the stilpnomelane lutites as well as a depositional timeframe for the Griquatown BIF.

III: Geochemical Concepts

Post-depositional Alteration

Rare Earth Elements + Yttrium (REY) plots are a widespread and commonly used tool to tackle many different BIF related geochemical problems (e.g. Beukes and Klein, 1990; Bolhar et al., 2005; Planavsky et al., 2010; Bekker et al., 2014). In the case of BIFs they can be used to obtain a substantial amount of information about its genesis and the Archean ocean in general. The main assumption about conducting REY studies of BIFs is that the fractionation of REY during the precipitation of the BIF constituting minerals is minimal and does not affect the REY patterns (Bekker et al., 2010). This assumption has been validated in both experimental work and by looking at present-day hydrothermal systems (Sherrell et al, 1999). Because there is negligible fractionation of the REY during precipitation, the REY patterns that are found are assumed to be representative of the seawater composition at the time of deposition. However, post-depositional deformation and metamorphism is capable of altering the REY patterns in BIFs after its deposition. This might happen under metamorphic conditions that are of amphibolite facies or higher or during large amounts of fluid-rock interactions (Bekker et al., 2010). In the case of the Griquatown iron formation, the conditions did not exceed late diagenetic to low-grade metamorphic facies and there is very little structural deformation (Beukes, 1984). Furthermore, there are no clear indicators for large scale fluid-rock interactions (Miyano and Beukes, 1984). The lack of high-grade metamorphic conditions and the absence of large scale fluid-rock interaction indicates that there is no reason to assume that the REY patterns of the Griquatown BIF have changed since deposition.

Justification of Normalization Scheme

REY plots of BIFs are able to provide a wealth of information. The behaviour of the different elements will give insight into the conditions in the Archean oceans and BIF genesis. The anomalies that are related to seawater characteristics are best quantified in a shale-normalised REY diagram. There are various reference shales available for normalisation. The two which are most commonly used in BIF studies are the North American Shale Composite (NASC; e.g. Beukes and Klein, 1990; Pickard, 2003) and Post-Archean Australian Shale (PAAS; e.g. Bolhar et al., 2005; Planavsky et al., 2010). Other less used reference materials include CI-chondrite (e.g. Alibert and McCulloch, 1993; Cabral et al., 2013), primitive mantle (Pickard, 2003) and Mud of Queensland (MUQ; Bolhar et al., 2005). For species specific BIF studies a total BIF composition reference composition may be used (Horstmann and Halbich, 1995). This yields a wide variety of reference materials used in BIF studies which makes direct comparison difficult. So, choosing appropriate reference material is crucial, picking a reference material that does not reflect your samples can result in large discrepancies in the results and faulty interpretation of the data. It is argued by Bolhar et al. (2004) that shale-normalised REY diagrams are best for observing BIFs as they are most capable of recording anomalies caused by processes taking place in seawater. This leaves us with two possibilities, NASC and PAAS, which are very similar in composition. When the compositions of NASC (Wronkiewicz and Condie, 1987; Birdwell, 2012) and PAAS (Pourmand et al., 2012) are compared, we can see that PAAS is enriched in LREE and depleted in HREE compared to NASC. This would indicate that NASC more closely represents BIFs, as they tend to be relatively depleted in LREE and enriched in HREE (Bau and Dulski, 1996). However, the REY abundances in NASC are mostly representative of the Earth's post-Precambrian continental crust (Gromet et al., 1984), making it less suitable for normalization of the BIF samples. Therefore PAAS will be the reference material that is used in this study. This reference material was first proposed by Nance and Taylor (1976) who were looking for an average REE composition of the upper continental crust. I will be using the recently revised values for the PAAS reference material as posed by Pourmand et al. (2012).

Rare Earth Elements

Since all REY are trivalent they should behave very similar with only small differences as a result of a decreasing ionic radius with increasing atomic number. However, the REY patterns for both modern

and ancient seawater have shown that other processes affect the abundance of certain REY. Now I will look at the elements that most commonly yield anomalous abundances and explain them.

The first element that displays behaviour which deviates from what is expected is the lightest of the REY, lanthanum. The positive La anomaly is related to the electron configuration of the atom and not so much to environmental factors (De Baar et al., 1991). It was found that La has an increased stability compared to other light rare earth elements (LREE) because its 4f electron shell is empty. As a result it is more stable in solution and thus it behaves more like the heavy rare earth elements (HREE). Similar reasoning also applies to the smaller scale anomalies for Gd and Tb (Bolhar et al., 2004). These REY are often slightly enriched in REY-diagrams for present-day seawater. Their small anomalies have also been attributed to the internal 4f electron shell configuration (De Baar et al., 1985). This electron configuration decreases the stability of particle complexes that involve Gd and Tb compared to complexes involving surrounding REY (Bolhar et al., 2004). As a result Gd and Tb may become enriched in solution compared to the surrounding elements.

The positive La anomaly is not as often discussed as that of the neighbouring element Ce, because Ce has an anomaly that is much more important when it comes to constraining processes in the Archean ocean. The Ce anomaly is one of the most pronounced anomalies in seawater. This anomaly is related to the redox state of the ocean because Ce is one of two redox sensitive REYs, Eu being the other. In the presence of an oxidiser the standard Ce(III) can be oxidised to Ce(IV), which is less soluble due to its higher charge. This decreased solubility results in higher Ce precipitation (Bolhar et al., 2004). As the Ce(IV) settles through the water column, it will be scavenged by particles, preferentially Fe- and Mn-oxyhydroxides, that are also precipitating (Bekker et al., 2014). This results in a dissolved Ce concentration that decreases with depth as more and more of the Ce(IV) will be scavenged by particle complexes as it spends more time in the water column. This process has been shown to have taken place and it is supported by geochemical analysis of the sunken particles, which reveal a positive Ce anomaly (Bolhar et al., 2004). Negative Ce-anomalies have been reported for Paleoproterozoic BIFs of ages ~1.8 Ga (Planavsky et al., 2009). However, Archean BIFs often lack the negative Ce-anomaly which implies that Archean oceans were anoxic as well as reducing (Planavsky et al., 2010). Since there is no oxidation potential to oxidise the Ce(III), the Ce anomaly would be smaller or even absent in Archean times (Bau and Dulski, 1996; Bolhar et al., 2005). Ce(III) is readily oxidised under conditions that are almost identical to those under which Mn(II) is oxidised (Bekker et al., 2014), therefore the absence or presence of this anomaly can give us an indication of the redox conditions in the Archean oceans.

The other redox sensitive element, Eu, also shows anomalous behaviour in seawater. Whereas Ce can get oxidised, Eu can get reduced from Eu(III) to Eu(II). Since reduced Eu(II) is more soluble than the standard Eu(III), the seawater signal will display a positive Eu. However, reduction of Eu(III) only takes place in high temperature hydrothermal systems where temperatures are above 250°C and the redox potential is sufficiently low (Bekker et al., 2014). The Eu(II) that is dissolved in the hydrothermal system at these temperatures originates from the dissolution of plagioclase under these conditions. This means that a positive Eu anomaly is indicative of a large influence of a hydrothermal source on the water composition. This also constrains the major source of the Fe that was supplied to the Archean oceans to form the BIFs. Bau and Dulski (1996) link the magnitude of the Eu anomaly to the age of the iron formation, arguing that, as time progresses, the mantle will cool down and the amount of hydrothermal activity will decrease. This will result in a smaller Eu anomaly as less reduced Eu is being provided to the oceans by hydrothermal systems. On the contrary, Bekker et al. (2014) state that this can also be the result of increased crustal growth processes and REYs being supplied from a continental source rather than a purely hydrothermal source, because the link between an increased continental influence on the REY signature of BIFs has not been sufficiently explored. Therefore a temporal shift from a hydrothermal to a major continental Eu source can also decrease the positive Eu-anomaly over time.

Yttrium is technically not a REE, however it is often included to provide a comparison with holmium (Ho). This can be done because they are nearly identical from a geochemical perspective; they are both trivalent and have very similar ionic radii (Y = 1.019 Å; Ho = 1.015 Å; Bau, 1996). Therefore their geochemical behaviour should be very similar. But, when Y/Ho ratios are investigated, we can see that they vary with depth and are always super-chondritic. Reference shale and chondritic ratios are very similar at Y/Ho ≈ 26, but BIF Y/Ho ratios often exceed this value (Bau, 1996; Bolhar et al., 2004). For example, Planavsky et al. (2010) reported an average Y/Ho ratio of 39 for their Archean BIFs. The main reason for the discrepancies in their behaviour is related to the redox cycling of Fe(II) and Mn(II) which causes Y/Ho fractionation, generating super-chondritic Y/Ho ratios in the Archean ocean (Bau et al., 1997; Bau and Dulski, 1999). This means that, in shale-normalized REY plots, Y anomalies will always be positive. Furthermore, the Y/Ho ratio decreases with depth which can be explained by preferential incorporation of Y over Ho in particle complexes. Y is preferentially incorporated into newly forming or precipitating Fe-oxide and hydroxide complexes over Ho (Bolhar et al., 2004), because it has a higher stability than Ho due to its electron configuration in the inner 4f shell (Bolhar et al., 2005).

Another common observation for shale normalised REY plots of both modern and ancient seawater is that the LREE are depleted compared to the HREE (e.g. Bau and Dulski, 1996; Bolhar et al., 2004). This can be directly related to the chemical properties of the REY and how these vary with atomic number. The LREE have a larger ionic radius than the HREE as a result of lanthanide contraction, which is the progressive filling of the f-electron shell, thereby reducing its ionic radius with increasing atomic number (Bolhar et al., 2004). The changes in ionic radius affect the solubility and susceptibility to complexation of the different REY which results in more LREE being adsorbed over HREE onto carbonate surfaces during carbonate complexation (Bekker et al., 2014). This results in solution being enriched in over LREE, generating the LREE depleted REY-pattern. These relative enrichments are often indicated using shale-normalized (SN) ratios of LREE/HREE that display minor or no anomalies. Commonly used ratios are $(Sm/Yb)_{SN}$ and $(Pr/Yb)_{SN}$ since these are REY that have a relatively large mass difference and do not show anomalous behaviour during BIF deposition (Bolhar et al., 2004).

Element	Equation
La*[2]	$3Pr - 2Nd$
Ce*[2]	$2Pr - 1Nd$
Eu*[3]	$0.67Sm + 0.33Tb$
Gd*[3]	$0.67Tb + 0.33Sm$
Y*[4]	$0.5Ho + 0.5Er$
Lu*[1]	$2Yb - Tm$

Table 2: The denominators of Eq. 5 for Y and for the elements that have no, or anomalously behaving, neighbouring elements.
[1]Alibo and Nozaki (1999);
[2]Bolhar et al. (2004);
[3]Alexander et al. (2008);
[4]Planavsky et al. (2010)

While it is good to be able to link qualitative observations of REY anomalies to various processes, it is possible to go one step further and quantify these anomalies. For a single element, this is achieved by comparing the observed REY value, with a value that is interpolated from close-by neighbouring elements that do not show anomalous values. This way it is possible to estimate what the value would have been if there would be no anomaly. In the simple case that both neighbouring elements have no anomalies the ratio, for REY number n, is quantified using Eq. 5 (Bolhar et al., 2004).

$$\frac{REE_n}{REE_n^*} = \frac{REE_n}{0.5(REE_{n-1}+REE_{n+1})} \qquad \text{(Eq. 5)}$$

This equation is a ratio of the observed value (REE_n) divided by the interpolated value (REE^*_n). As discussed above, there are various REE that have anomalies and either lack two neighbouring elements (La and Lu) or have neighbouring elements that also contain anomalies (La, Ce, Eu and Gd). For these elements the equations are not as simple as directly neighbouring elements show anomalous behaviour, therefore they cannot be used in order to prevent error propagation. This will increase the error related to the interpolation. Moreover, Y is not included in Equation 5 since it is not a REE, but it is possible to calculate its anomaly. The formulae used to calculate the denominators of Equation 5 for elements which show anomalous behaviour are shown in Table 2.

Sulphur Isotopes

Sulphur consists of four stable isotopes, ^{32}S, ^{33}S, ^{34}S and ^{36}S. Since fractionation of isotopes generally occurs within the decimal places I will be using the delta (δ) notation to indicate fractionation for the sulphur isotope ^{3x}S, where x is 3, 4 or 6 (Eq. 6). ^{32}S is used as denominator for determining the ratio as it is the major isotope of sulphur, accounting for approximately 95% of all S (Seal II, 2006).

$$\delta^{3x}S = 1000\left(\frac{\left(^{3x}S/^{32}S\right)_{sample} - \left(^{3x}S/^{32}S\right)_{CDT}}{\left(^{3x}S/^{32}S\right)_{CDT}}\right) \quad \text{(Eq. 6)}$$

To determine the $\delta^{3x}S$ ratio, reference material will have to be used for normalization. The agreed reference material for sulphur isotopes is the Canyon Diablo Troilite (CDT) for which I will use the ratios determined by Ding et al. (2001).

Due to the high abundance of sulphur and its importance in both biotic and abiotic processes, being able to trace the fractionation of sulphur isotopes has proven instrumental in understanding the ancient sulphur cycle. Almost all of the present-day sulphur fractionation is Mass Dependent Fractionation (MDF). This is based on the slight differences in bond energies between S and O bonds due to different isotopes of sulphur. The MDF is what is shown using the delta notation. However, sulphur fractionation may also take place through mechanisms that were not based on differences in bond energy; this type of sulphur fractionation is called the Mass-Independent Fractionation (MIF). However, prior to the GOE the magnitude of sulphur MIF was larger than it is at present day. The MIF cannot be quantified using the $\delta^{3x}S$ ratios and is instead quantified using $\Delta^{3x}S$ ratios, where x is 3 or 6 (Eq. 7; Farquhar et al., 2000).

$$\Delta^{3x}S = 1000\left(\left(1+\frac{\delta^{3x}S}{1000}\right) - \left(1+\frac{\delta^{34}S}{1000}\right)^{y} - 1\right) \quad \text{(Eq. 7)}$$

This equation shows how the measured mass dependent fractionation $\left(1+\frac{\delta^{3x}S}{1000}\right)$ deviates from the mass-dependent fractionation that is predicted based on the differences in bond energy for the different sulphur isotopes in S-O bonds $\left(\left(1+\frac{\delta^{34}S}{1000}\right)^{y}\right)$. In this part of the equation, the exponent (y) represents the mass-dependent isotope fractionation ratios between $\delta^{3x}S$ and $\delta^{34}S$. For $\Delta^{33}S$ the value for the power is 0.515 and for $\Delta^{36}S$ the value for the exponent is 1.90 (Farquhar et al., 2000).

During MDF the redox state of sulphur is changed, between S(VI), S(IV), S(0) and S(-II), through biotic or abiotic processes during various steps and multiple cycles in order to fractionate the sulphur isotopes. These processes will alter the $\delta^{3x}S$ ratios, but do not affect the $\Delta^{33}S$ and may slightly affect the $\Delta^{36}S$ ratio (Johnston et al., 2007; Kamber and Whitehouse, 2007). The oxidation of the sulphur through its various redox states will take place using various kinds of, mainly abiotic, processes. However, the reduction of S(VI) down to S(-II) can be achieved by both biotic and abiotic reactions. The microbial reduction of sulphur takes place because the SO_4^{2-} ion acts as an electron acceptor for anaerobic respiration, during which it is converted to H_2S (Shen and Buick, 2004). During this process the uptake by the cell will be similar to that of the seawater. However, during reduction inside the cell the ^{32}S-O bond is reacting faster than the ^{34}S-O bond since it has a lower bond energy which means that H_2S is enriched in ^{32}S compared to the ^{34}S-rich sulphur that remains inside the cell. This results in large isotope fractionations of up to 46 ‰ (Shen and Buick, 2004). Furthermore, it has been shown that during the incorporation of S into pyrite, the fractionation is minimal through both biotic and abiotic pathways, <-1‰ (Balci et al., 2007). This means that it should be possible to trace sulphate reducing bacteria back in time based on the sulphur isotope composition of pyrite.

The large fractionation that is caused by microbial sulphate reduction would be ideal to trace if it was the only process capable of generating large amounts of sulphur fractionation. However, there are some other processes which are also capable of fractionating the S isotopes, including sulphur disproportionation reactions and abiotic sulphur isotope fractionation. Sulphur disproportionation microorganisms are capable of oxidizing the sulphur from various reduced states back to S(0) by

reacting with the surrounding water in the presence of Fe-oxyhydroxides. They are able to generate fractionations between 5 and 9 ‰ (Canfield and Thamdrup, 1994). During this process the sulphur can be cycled between oxidation and reduction with each cycle fractionating the sulphur by 5 to 9 ‰. Within the Archean ocean these Fe compounds were very abundant during the deposition of BIFs which means that this process could have a significant influence on the fractionation of S isotopes.

Abiotic sulphur isotope fractionation generally takes place in high-temperature hydrothermal systems with a neutral pH, there can be SO_4^{2-} reduction by Fe-minerals which can result in a fractionation of 20-30‰ (Ohmoto and Goldhaber, 1997). During magmatic hydrolysis where temperatures exceed 400°C it is possible for SO_2 to react with water to form acidic sulphur compounds which can fractionate the sulphur isotopes as much as 15-20‰ (Ohmoto and Goldhaber, 1997). Finally, during the diagenetic processes, hydrocarbons can reduce sulphate to form H_2S. This results in fractionations up to 50‰ (Canfield, 2001).

On the other hand, MIF will also fractionate the sulphur isotopes, but not based on bond energies. Instead, this process was mainly dominant in the Archean atmosphere where SO_2 photolysis takes place in an oxygen-free atmosphere as a result of UV radiation (Farquhar et al., 2003). As a result the S is converted to elemental sulphur and sulphate ions (SO_4^{2-}). The $\Delta^{33}S$ are different for both sulphur compounds. The reduced elemental sulphur will display $\Delta^{33}S < 0$ while the oxidised SO_4^{2-} will show $\Delta^{33}S > 0$ (Farquhar et al., 2001). The temporal evolution of $\Delta^{33}S$ has often been linked to the evolution of oxygen in the atmosphere as various studies show that there is significant $\Delta^{33}S$ variation prior to the GOE which gets muted around 2.45 Ga which is attributed to the onset of the GOE (Bekker et al., 2004; Farquhar et al., 2011; Reuschel et al., 2013). Subsequently, at approximately 2.32 Ga the sulphur MIF signal disappears from the geological record (Bekker et al., 2005). This is due the accumulation of sufficiently high concentrations of free O_2 in the atmosphere which resulted in the formation of the ozone (O_3) layer that shields the surface of the Earth from the UV radiation. Hence the MIF could no longer take place and $\Delta^{33}S$ values centred around zero. This means that $\Delta^{33}S$ values can be used to infer whether the deposition of the Griquatown BIF took place pre-, post- or during the onset of the GOE.

IV: Sample Acquisition and Description

Sample Acquisition

Twenty one samples have been recovered from five different cores, capturing the Griquatown and Kuruman BIF, were drilled close to Hotazel (~60 km NW of Kuruman), in the North Cape province, South Africa (Fig. 6; Table 3). These cores were meticulously logged prior to this study (P.B.H. Oonk, personal comm.). During the logging of the cores various stilpnomelane lutite layers were discovered. The samples that I am using are the stilpnomelane lutites that were found. Twelve samples were used from the GASESA-1 core, three from HEX5, three from AARPAN5, two from ERIN3 and one sample was used from the Middelplaats (MP) core. I will mainly be focusing on those found within the Griquatown BIF (Fig. 5). Samples that are not located in the Griquatown BIF are HEX S3 and ARP S1 which come from the Kuruman BIF and sample MP53 which was taken from the Hotazel formation (Fig. 2). There is no log available to pin-point the location of sample MP53 in the MP drilling core. However, the stratigraphic location of this specific sample is described as being found directly below the topmost of the three manganese layers (H. Tsikos, personal comm.).

Core	Coordinates
GASESA-1	27° 05'53.45" S; 23° 01'57.26" E
HEX5	27° 05'02.05" S; 23° 05'47.43" E
ERIN03	27° 09'07.26" S; 23° 12'57.04" E
AARPAN5	27° 04'31.45" S; 23° 14'14.20" E
MP	27° 21'28.43" S; 22° 56'01.59" E

Table 3: Exact coordinates of drilling sites for sample acquisition (P.B.H. Oonk, personal comm.).

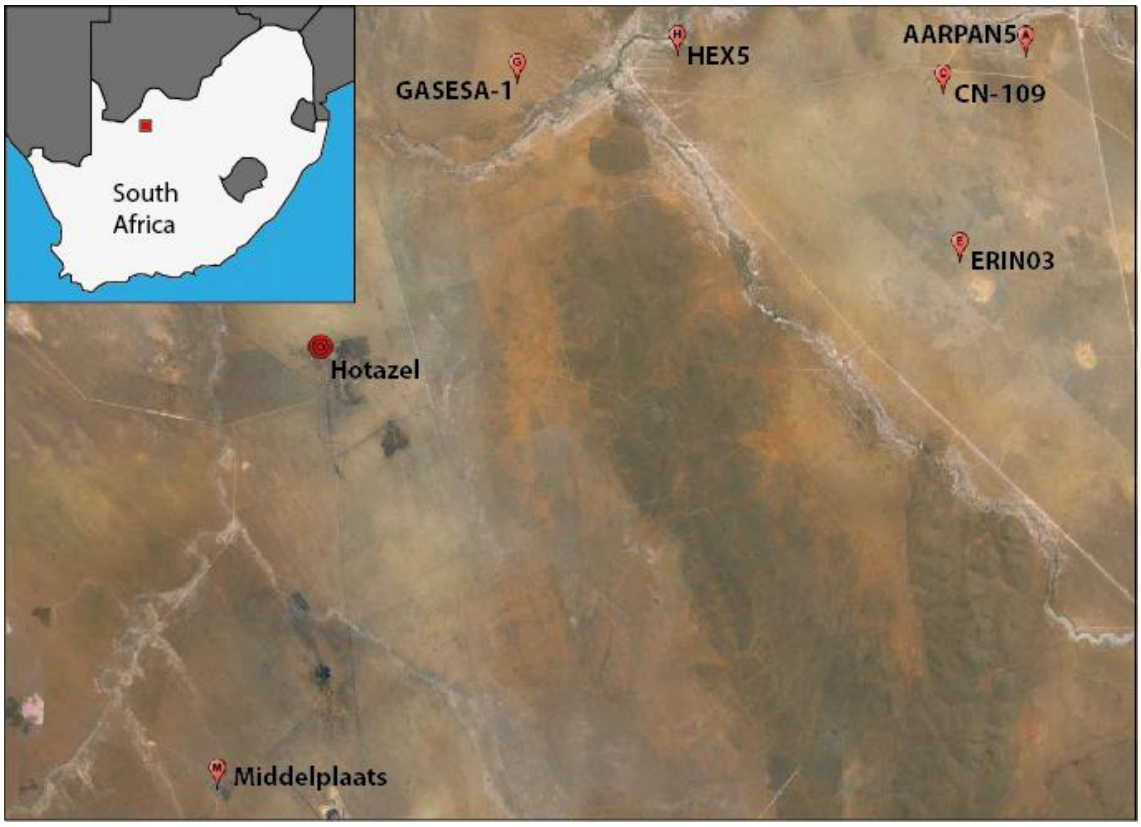

Figure 6: Locations for the cores used in this research and the approximate location of the core CN-109 from Beukes and Klein (1990).

Sample Description

The majority of the samples are very similar to each other in that they are dark-coloured, fine-grained, mudstones with possible mineral veins (Table 4). Samples that clearly deviate from this are GAS S9, GAS S12 and MP53 (Fig. 7a-c). Figure 7a shows the pyrite veining in the upper piece of sample GAS S9 as well as variations in layer thickness that are related to a vein of a grey-to-white coloured mineral being present in the lower piece of the sample. Sample GAS S12 shows a large variability in textures, mineralogy and colouring (Fig. 7b). Its appearance is completely different from the other samples which are usually, except for GAS S9, thinly bedded while in this sample the bedding is very irregular. Finally, sample MP53 appears compositionally different. It does not conform with the dark-brown or black colours that are characteristic for the other samples, instead it has a red-to-purple colour (Fig. 7c).

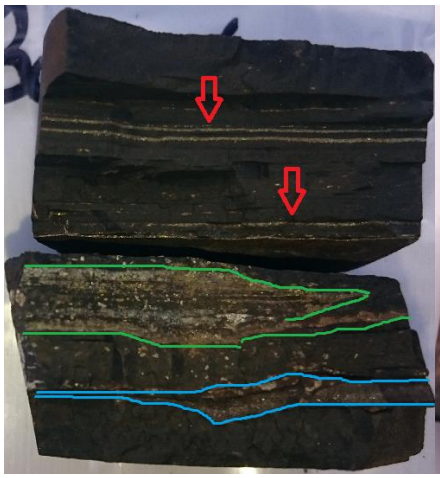

Figure 7a: Sample GAS S9

Figure 7b: Sample GAS S12

Figure 7c: Sample MP53

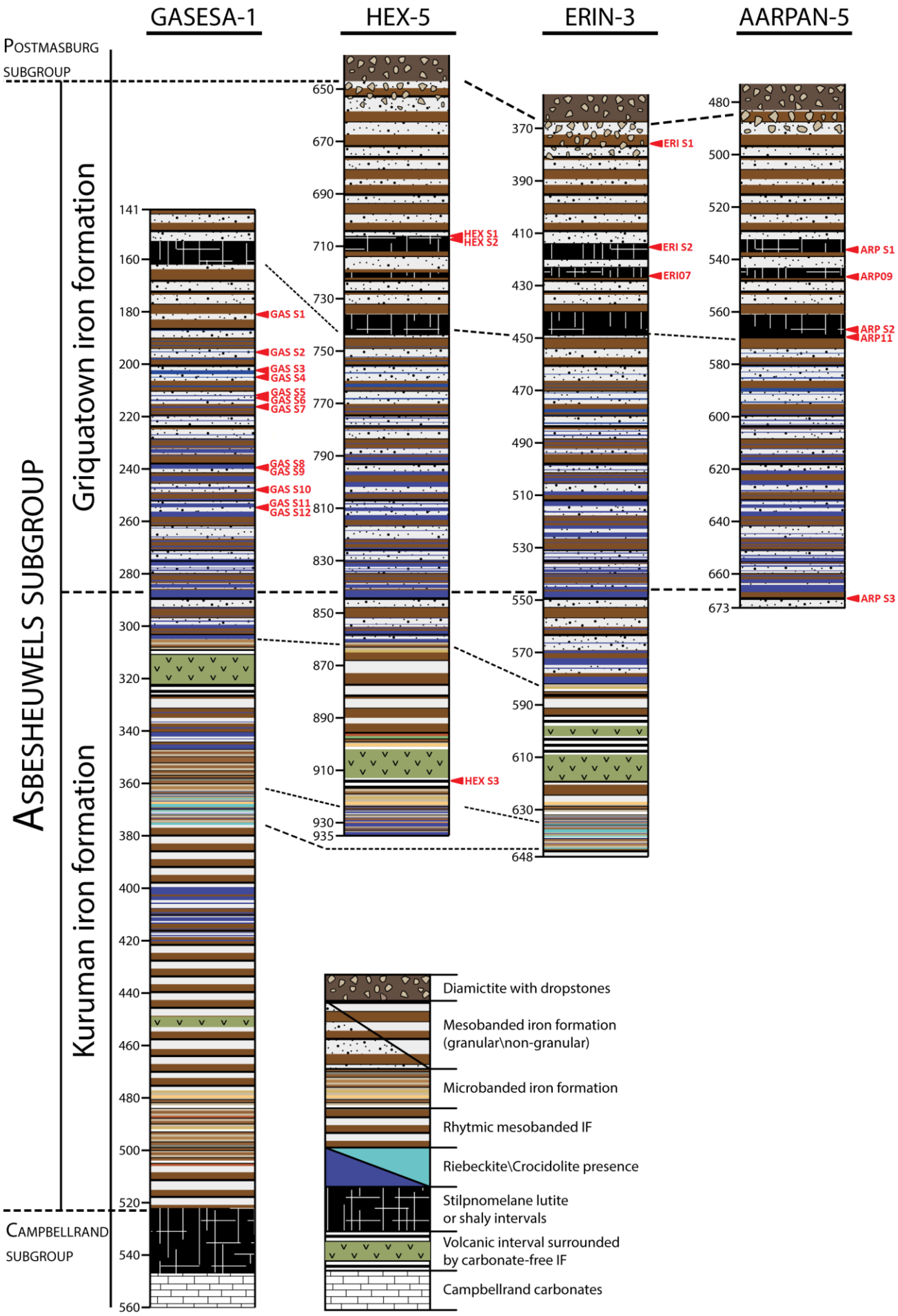

Figure 5: Stratigraphic columns for the drill cores from which the samples were derived. Red arrows indicate the stratigraphic positioning of the samples. Samples ERI07, ARP09 and ARP11 are samples from another study but are included here as their sulphur isotopic composition was determined in this study (P.B.H. Oonk, personal comm.).

Sample	Brief sample description	Powder Colour
GAS S1	Dark-coloured, fine-grained, mudstone. Has two calcite veins	Olive grey
GAS S2	Dark-coloured, fine-grained, mudstone.	Greyish-brown
GAS S3	Dark-coloured, fine-grained, thinly bedded mudstone.	Grey
GAS S4	Dark-coloured, fine-grained, mudstone. Contains ankerite inclusions	Brown
GAS S5	Dark-coloured, fine-grained, thinly bedded mudstone.	Olive grey
GAS S6	Dark-coloured, fine-grained, thinly bedded mudstone.	Grey
GAS S7	Dark-coloured, fine-grained, thinly bedded mudstone.	Dark grey
GAS S8	Dark-coloured, fine-grained, thinly bedded mudstone.	Grey
GAS S9	Dark-coloured, fine-grained, mudstone. Contains very abundant pyrite, both randomly distributed and in veins and its layer thickness varies laterally	Light brown
GAS S10	Dark-coloured, fine-grained, thinly bedded mudstone.	Deep grey
GAS S11	Dark-coloured, fine-grained, thinly bedded mudstone. Consists of three pieces, one of which has non-linear bedding.	Black
GAS S12	Dark-coloured, fine-grained matrix which contains a large heterogeneous mixture of Fe-carbonates, pyrite and quartz in a stilpnomelane matrix	Brown
HEX S1	Dark-coloured, fine-grained, mudstone.	Black
HEX S2	Dark-coloured, fine-grained, mudstone. Contains a pyrite vein	Grey
HEX S3	Dark-coloured, fine-grained, mudstone.	Light grey
ARP S1	Dark-coloured, fine-grained, mudstone.	Grey
ARP S2	Dark-coloured, fine-grained, mudstone.	Light grey
ARP S3	Dark-coloured, fine-grained, mudstone. Contains surface pyrite as well as veins containing pyrite.	Dark grey
ERI S1	Dark-coloured, fine-grained, mudstone. Contains bands of pyrite and ankerite or quartz.	Dark brown
ERI S2	Dark-coloured, fine-grained, mudstone.	Light grey
MP53	Purplish-Black, thinly bedded, fine-grained mudstone. Has a red to purple streak upon polishing.	Purplish-red

Table 4: Sample definition and description. For more detailed descriptions including pictures of the samples the reader is referred to Appendix A. For the original sample names the reader is referred to Appendix H.

V: Analytical Techniques

Sample Preparation

The samples were selected from drill cores and brought back to Utrecht University (UU) for analysis. First the samples were polished to remove the exposed surface layer to remove the weathering. Exceptions were made for samples ARP S3 and GAS S12, where one side was not polished to preserve the surface pyrite (Fig. 8a). Furthermore, a part of sample GAS S12 containing a secondary calcite vein was sawn off using a diamond saw to prevent the secondary calcite vein affecting the geochemistry (Fig. 8b). After polishing, the samples were crushed into smaller, sub-cm, pieces on an anvil using a steel mallet. Subsequently they were ground down to powder using a Herzog HP-MA tungsten carbide (WC) grinder at the Gemeenschappelijk Milieulaboratorium (GML) facility. The use of WC has implications on the elements that I can use for data interpretation. Certain elements will have to be excluded from the data analysis

Figure 8a: Sample ARP S3. Surface pyrite was preserved for further analysis.

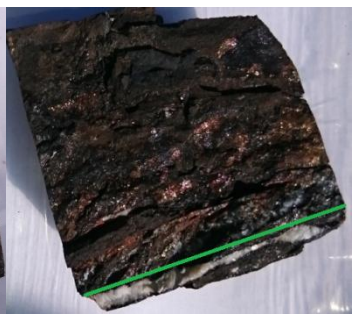

Figure 8b: Sample GAS S12. Pink spots are weathered surface sulphate minerals. Green line indicates cutting location.

because they may be introduced as contamination from the WC grinder. There might be are significant amounts of contamination for Co and W with up to hundreds of ppm of these elements introduced during grinding (Hickson and Juras, 1986). Elements for which trace amounts, usually below 5 ppm, could be introduced are Sc, Ta and Nb.

X-Ray Diffraction

X-ray diffraction (XRD) analysis was conducted to infer the major mineralogical composition of the stilpnomelane lutites. Approximately 1 g of powder was weighed for all samples and directly introduced into the XRD. The samples were analysed using a cobalt X-ray tube with a wavelength of 1.78897 Å. The 2Θ angles between 5° and 75°, which correspond to atomic plane distances of 1.3 to 20.5 Å, were measured. For XRD the distance between atomic planes is measured following Bragg's law ($n\lambda = 2dsin(\theta)$). The reflection of the x-rays will generate peaks at specific angles that we can use to infer mineral specific atomic plane distances. The XRD has a relatively high detection limit of approximately 5 wt% for a specific mineral. However, it is ideal for identifying the major mineralogy of the samples. The XRD is a qualitative method which means that it is impossible to infer exact amounts or fractions of certain minerals present.

ICP-OES and ICP-MS

In preparation for the Inductively Coupled Plasma Optical Emission Spectroscopy (ICP-OES) and Inductively Coupled Plasma Mass Spectrometry (ICP-MS) analyses the samples were digested. This was achieved via the introduction of various acids that break down the bonds present in the minerals. First, approximately 125 mg of sample powder was weighed and placed it in a capped 30 ml Savillex PFA destruction vessel. Subsequently 2.5 ml 48% hydrofluoric acid (HF) and 2.5 ml mixed acid were added. The mixed acid consists of 65% nitric acid (HNO_3) and 72% perchloric acid ($HClO_4$) at a ratio of $HClO_4$:HNO_3 = 3:2. The closed vessels were then left overnight on a hotplate at 90°C. After cooling the samples, the caps were removed and the samples were evaporated on hotplate at 140°C for 3-4 hours. Next 25 ml of 1 M HNO_3 was added and the vessel was closed and left overnight to react on a hotplate at 90°C. When the samples cooled down to room temperature they were weighed to determine the dilution factor. For six samples (GAS S4, GAS S10, GAS S11, GAS S12, HEX S1 and MP53) this digestion procedure was insufficient to dissolve the samples, indicating the presence of possible organic compounds. For these samples another method was required. Following the HF-$HClO_4$-HNO_3 reaction and evaporation the samples were digested in 2.5 ml concentrated hydrogen peroxide (H_2O_2) and 2.5 ml concentrated HCl and subsequently dried. Subsequently 25 ml 1 M HCl was added. Following this digestion all but one of the samples were digested properly. The sample that was not fully digested was GAS S11. The international standard ISE-921 was added during digestion to check for recoveries on ICP-OES and ICP-MS.

Major elements were analysed using ICP-OES analysis whereas minor and trace elements were analysed using ICP-MS. The prepared solutions are introduced to a plasma torch which ionises them via a nebuliser. In ICP-OES we look at the photons that are emitted by ionising and relaxing atoms. These emitted photons have wavelengths which are characteristic for each element. To measure this, the plasma source is combined with a diffraction grating which separates the photons based on wavelength. These wavelengths are analysed, together with the intensity of the light, using a charge-coupled device (CCD) to infer the element and its abundance. For ICP-MS the plasma torch is coupled to a mass spectrometer. As the samples are ionised, they will travel through the mass spectrometer which separates the ions using a ThermoFischer Scientific X-series quadrupole mass spectrometer, based on their mass-to-charge ratio. Subsequently the ionised atoms collide with a detector at the end of the instrument, where the amount of counts are proportional to the elemental abundance.

X-Ray Fluorescence

X-ray fluorescence (XRF) was used to determine the major and trace element composition of the stilpnomelane lutites. Major elements were analysed via a fusion bead method and trace elements

were analysed using pressed-powder pellets. For the fusion beads, 2 g of sample was weighed into a ceramic container. These were placed in a Leco TGA710 Thermo-gravimetric Analyser (TGA) where they were heated to 1000°C in multiple temperature steps to oxidise the samples and determine the loss on ignition (LOI). After oxidation, 0.6 g of sample was weighed and mixed with 6 g lithium borate ($Li_2B_4O_7$) and lithium iodide (LiI) in a sample cup. Subsequently the samples were placed in a Herzog HAG-S which heated the samples up to 1400°C. This way the samples were transformed to homogeneous fusion beads. The pressed-powder pellets were prepared by weighing 10 g of sample in sample cups. Two samples, HEX S1 and ERI S2, were not analysed because there was insufficient sample to make pressed-powder pellets. The samples were subsequently mixed with seven wax tablets, conform the calibration of the XRF, and placed in the Herzog HP-MA sample crusher. The crusher was linked to the Herzog HP-PA pellet producer which made the pressed-powder pellets by applying forces up to 150 kN.

During XRF analysis the sample is bombarded with X-rays. This results in the excitation of electrons in the lower electron shells through the energy absorption of the incident x-rays. Once their energy state reaches a critical level they are ejected from the orbit they are in. This leaves a vacant slot in a lower orbit which will be filled by an electron from a higher orbit since it is energetically more favourable to be in a lower electron shell. As the electron moves to a lower orbit, it will emit energy at a certain wavelength which can be measured. Based on the element characteristic wavelength the elements and their abundances can be identified.

Sulphur and Carbon

Total sulphur (TS), total carbon (TC), total organic carbon (TOC) and total inorganic carbon (TIC) analyses have been conducted using a Leco SC632 sulphur and carbon analyser. For the TC/TS analysis I weighed approximately 200 mg of sample powder in ceramic boats with an internal nickel liner. Calibration was done using two C&S standards, a low C&S powder with 2.3% C and 0.031% S and a high C&S powder with 12.76% C and 0.221% S. For the TIC/TOC analysis 300 mg of sample powder was weighed into a ceramic boat with nickel liner. These were placed in a Thermo Scientific Heraeus M110 muffle furnace where the samples were gradually heated. The temperature was set to 450°C for 30 minutes after which it was increased to 550°C where it remained for another half hour before cooling to room temperature. The heating steps removed the organic carbon and sulphur. The samples were then placed in the LECO SC632 S&C analyser where I analysed the carbon content using the original mass of the samples, in this case the remaining carbon represents the TIC. By subtracting the TIC from the TC the TOC of the samples was determined. To ensure that there were no calibration errors, second CS-analysis was run using 200 mg of sample together with the TIC determination.

Acid Volatile Sulphide/Chromium Reducible Sulphide Extractions

Sulphur isotope data was obtained from sulphur that was extracted using a combined Acid Volatile Sulphide (AVS) and Chromium Reducible Sulphur (CRS) method. A distillation method was used to extract the sulphur from the samples. For these extractions I only used the sulphur rich samples. The sulphur content was predetermined using TS data from the CS-analyser as well as ICP-OES measurements. From these results the samples that were hand-picked for analysis were GAS S9, GAS S11, GAS S12, HEX S1, HEX S2, ARP S1, ARP S2, ARP S3 and ERI S1. On top of these samples, three extra samples from the same cores were analysed as well, ARP09, ARP11 and ERI07 (P.B.H. Oonk, personal comm.). For the distillation method a set-up as shown in Fig. 9 was used. Prior to the extraction, a $CrCl_2$ solution was prepared by dissolving 266 g chromium chloride hexahydrate ($CrCl_3 \cdot 6H_2O$) in deionised water and diluting up to 1 l. Next 450 ml of this solution was mixed with 50 ml HCl in an Erlenmeyer flask containing elemental Zn granules. The atmosphere within the bottle was made anoxic by purging with nitrogen. The solution was left for three hours to allow the Zn to react with the Cr(III) in the $CrCl_3$ to reduce it to Cr(II) and form $CrCl_2$.

The reactions that take place here are redox reactions (Eq. 8 and Eq. 9).

$$Zn + 2\,HCl \rightarrow Zn^{2+} + 2Cl^{-} + H_2 \quad \text{(Eq. 8)}$$

$$2\,CrCl_3 + H_2 \rightarrow 2CrCl_2 + 2Cl^{-} + 2H^{+} \quad \text{(Eq. 9)}$$

The progress of this reaction was tracked by changes in the colour of the solution. Cr(III) solutions are deeply green coloured, while the solution will become blue upon the conversion to Cr(II). After three hours, syringes were filled with 30 ml chromium chloride solution and stored in a refrigerator. This was done to prevent the reaction between the Zn(s) and the Cr(III) to continue as this reaction consumes the H^+ and makes the solution less acidic. The acidity in the solution has to remain high as it is required to generate hydrogen sulphide (H_2S(g)). Next a fraction of the sample was weighed and placed in a 500 ml round bottom flask. The amount of used sample was dependent on the sulphur content of the sample. I used anywhere between 50 mg and 6.0 g. The original sample mass that would be placed in the round-bottom flask was calculated using the ratio between the molar mass of S and that of Ag_2S (0.129), assuming the yield would be *x* mg Ag_2S using Eq. 10. I aimed for a yield of 30 mg, thus making *x* = 30 in Eq. 10.

$$m_{sample} = \frac{0.129x}{10 * wt\%S} \quad \text{(Eq. 10)}$$

The samples were then rinsed with ethanol, which acts as a catalyst. An anoxic atmosphere was created in the flask by purging it with nitrogen for 10 minutes at a constant rate of approximately 2 bubbles per second. This rate was monitored and maintained throughout the experiment. Next 20 ml HCl and 30 ml of the $CrCl_2$ solution were added to the round bottom flask, through a septum, to react with sulphide in the sediments. To allow the reactions to take place, the round-bottom flasks were placed in a heating mantle which was kept at a constant temperature of 85°C, just below the boiling point of the solution. The mixture was stirred and heated constantly to facilitate the sulphide liberation.

$$Cr(II) + S(-I) \rightarrow Cr(III) + S(-II) \quad \text{(Eq. 11)}$$

$$S(-II) + 2H^{+} \rightarrow H_2S\,(g) \quad \text{(Eq. 12)}$$

Equations 11 and 12 are the reactions that explain the chemistry behind how the pyritic sulphide is converted to H_2S(g). The resulting gas rises through a coiled condenser containing H_2O which condenses rising HCl(g) and recycles it back into the round-bottom flask. The remaining H_2S(g) rises through the coiled condenser and goes through two traps. The first trap contains deionised H_2O and acts as an acid trap by removing any remaining acid fumes that have passed through the coiled condenser. Next, the H_2S(g) reaches the sulphide trap. The trap consists of a Zn-acetate solution. This solution is made by dissolving 40 g Zn-acetate in 100 ml deionised H_2O. Next, 30 ml acetic acid is added and the solution is diluted up to 1 l using deionised H_2O. In the sulphide trap, the H_2S reacts with the Zn-acetate to form a white precipitate, zinc sulphide. This reaction was allowed to take place for approximately three hours.

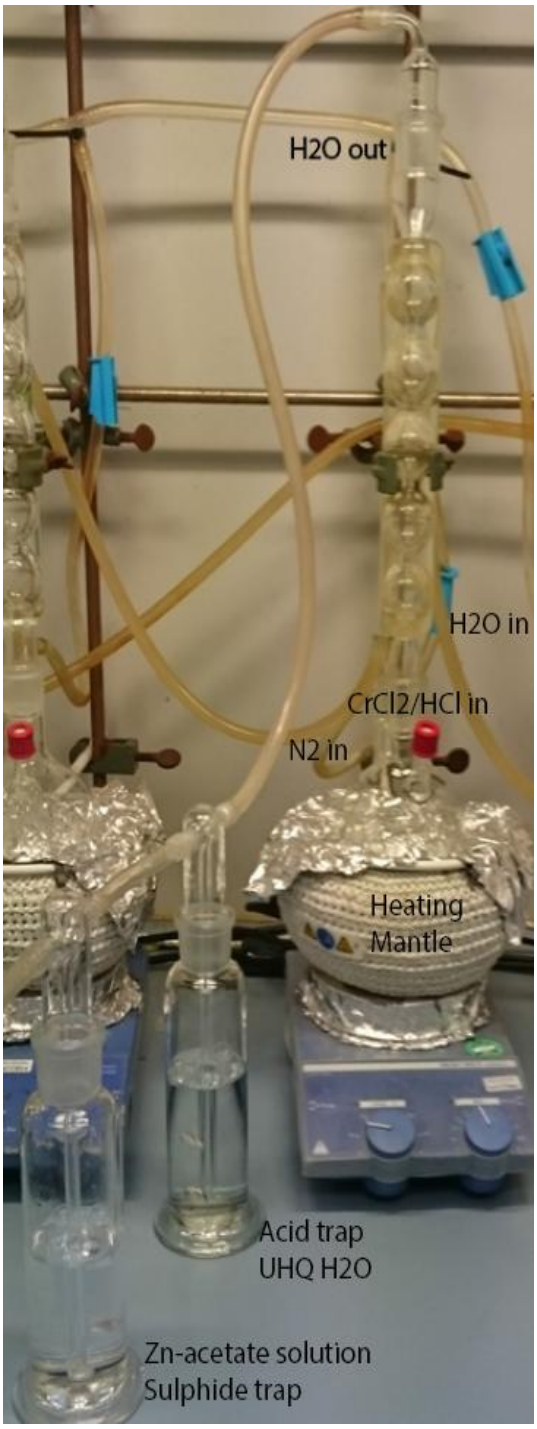

Figure 9: Set-up for one column of S-extractions. In the experiments four of these were used in sequence. The full extraction protocol can be found in Appendix G.

After the extraction was finished, the ZnS solution was transferred to a beaker and 10 ml 0.1M $AgNO_3$ solution was added to the ZnS-solution. The $AgNO_3$-solution was prepared by dissolving 16.99 g $AgNO_3$ in deionised H_2O and diluting to 1 l. The introduction of the $AgNO_3$ solution resulted in the conversion of ZnS to Ag_2S, which will precipitate from the solution. This is marked by an abrupt change in colour of the solution, from milky white to deep black. After complete conversion, the solution was heated to just below boiling point. This will cause the Ag_2S to coagulate, which makes it easier to process during the filtration. The resulting solution and precipitate were filtered using pre-weighed 0.45 micron cellulose nitrate filters. Filtering took place using a membrane pump in combination with a filtration device. First the sample was cleaned using UHQ water. For the next wash a small amount of 1M ammonia solution (NH_4OH) was used to remove any possible contaminants. This solution was prepared by mixing 155 ml 25% NH_4OH with 845 ml H_2O. A third cleaning took place using UHQ water. After the filtration process, the filter was transferred to a plastic Petri dish and placed in a drying oven at 40°C. After drying, the filters were weighed to determine the yield. In order for there to be enough Ag_2S to ensure S-isotope analysis, the sulphur concentrations found in the TS measurements were back-calculated to determine the amount of sample required. Based on these calculations, the amount of sample that was placed in the round bottom flask was varied for each sample. This was done to ensure the yield would be sufficient to be able to salvage 2-3 mg from the filtered material. Since not all material can be recovered from the filters, an excess amount is extracted. Measurements using this technique required between two and three milligrams of Ag_2S. The sulphur isotope extractions and measurements were performed at the Geological and Paleontological institute of the Westfälische Wilhelms Universität Münster. Isotope measurements were done using an elemental analyser isotope ratio Mass Spectrometer (EA-IRMS). Quality control of the quadruple sulphur isotopic measurements was performed using the international reference material IAEA-S1.

VI: Results

Mineralogy

The samples from the Griquatown and Kuruman BIFs have a relatively homogeneous mineralogy (Table 5). Using data from XRD analysis, I was able to identify eleven different major minerals: stilpnomelane, pyrite, magnetite, siderite, ankerite, quartz, calcite, biotite, clinochlore, K-feldspar and talc. In most cases stilpnomelane is the dominant mineral, but in some samples quartz (ARP S1 and ARP S3), siderite (GAS S9 and GAS S12) or biotite (GAS S5, GAS S8 and GAS S11) are most abundant. Pyrite is another very prevalent mineral, it is found in all but one of the samples. The only Fe-oxide found was magnetite, no major hematite fraction was found in the samples from the Kuruman and Griquatown iron formations. Fe-carbonates are common minerals as well, being a major fraction in eleven samples. In all but one of the samples containing Fe-carbonates ankerite is found, but siderite was only identified on five occasions. Various Fe-silicates have also been found; stilpnomelane is present in all samples while biotite was identified in eleven. Clinochlore and talc are among the less common silicates. Based on previous research regarding the mineralogy of BIFs it is likely that the type of talc mineral found is the Fe-bearing talc variant, minnesotaite (Beukes and Klein, 1990; Webb et al., 2003). The presence of biotite in the XRD data correlates well with the physical appearance of the samples, those with more abundant biotite show more distinct layering, while samples without biotite do not. Non-Fe bearing minerals are also found, but the only non-Fe bearing mineral that is found in more than one sample is quartz while calcite (GAS S1) and K-feldspar (ARP S2) only occur in one sample. The mineralogy of sample MP53 is distinctly different from the mineralogy of the other samples as it is dominated by hematite with minor presence of quartz and clinochlore. This can be related to the stratigraphic positioning of MP53, which is found in the younger Hotazel formation. This implies that the depositional environment would have been different during deposition of the Kuruman and Griquatown BIFs compared to the depositional environment during the deposition of the Hotazel formation.

Sample	Stilp	Pyr	Mag	Hem	Sid	Ank	Qtz	Cal	Bt	Cli	Kfs	Talc
GAS S1	X	X	X					X				
GAS S2	X	X	X							X		
GAS S3	X	X	X						X			
GAS S4	X	X	X			X						X
GAS S5	X	X	X		X	X			X			
GAS S6	X	X	X				X		X			
GAS S7	X	X	X						X			
GAS S8	X	X	X						X			
GAS S9	X	X	X		X	X	X		X			
GAS S10	X	X	X				X		X			
GAS S11	X	X	X				X		X			
GAS S12	X	X	X		X	X	X		X			
HEX S1	X	X	X		X	X						
HEX S2	X	X	X			X	X			X		
HEX S3	X	X	X						X	X		
ARP S1	X	X	X			X	X			X		
ARP S2	X	X	X			X	X		X		X	
ARP S3	X	X	X			X	X					
ERI S1	X	X	X			X	X					
ERI S2	X	X	X		X		X			X		
MP53				X			X			X		

Table 5: The major mineralogical composition of the stilpnomelane lutites as inferred from XRD analysis. Stilp = Stilpnomelane, Pyr = Pyrite, Mag = Magnetite, Hem = Hematite, Sid = Siderite, Ank = Ankerite, Qtz = Quartz, Cal = Calcite, Bt = Biotite, Cli = Clinochlore, Kfs = K-feldspar. The fully interpreted XRD patterns can be found in Appendix F.

Major Element Geochemistry

The bulk of the sample is comprised of two compounds, SiO_2 and Fe_2O_3, which together make up between 61.93 and 89.02 wt% (Table 6). Their abundances are inversely related, if the SiO_2 content increases, the Fe_2O_3 content decreases and vice versa. The remainder of the major elements all constitute minor amounts. Al_2O_3, MgO, K_2O, and occasionally CaO are present at 1-10 wt% oxide levels while TiO_2, MnO, Na_2O, P_2O_5 and often CaO are present at sub-1 wt% oxide levels (Table 6). The LOI of the samples is between 2.38 and 6.61 wt%, except for samples with abundant Fe-carbonates which have a LOI between 13.81-15.39 wt%. The high abundances of Fe_2O_3 and SiO_2 are also reflected in the mineralogy as all but one of the observed minerals are bearing at least one of these elements in large amounts, the exception being calcite which was only identified in GAS S1.

The reliability of the results was tested by comparing two independent datasets as well as looking at their respective recoveries. These were computed for ICP-OES and XRF fusion beads by comparing the processed and measured ISE-921 values to their reference values. Recoveries for both XRF and ICP-OES are between 90 and 110% for all elements except for P_2O_5 measured using XRF which has a 117% recovery. For XRF, the average sum of the major element oxides for is 99.3±1.5 wt%, implying that results for both ICP-OES and XRF are reliable. Both datasets were converted to wt% oxide abundances to allow for a direct comparison. For the XRF no distinction was made between Fe(II) and Fe(III), therefore the reported Fe_2O_3 abundance represents the total Fe ($Fe_2O_3^T$). For consistency, ICP-OES Fe-abundances were also converted to Fe_2O_3. However, this implies that all of the Fe in the sample is trivalent which is not the case. The abundant minerals, stilpnomelane, biotite, magnetite, siderite, ankerite and pyrite, all contain significant amounts of divalent Fe. When all Fe is assumed to be divalent and a conversion is applied using the mass-ratios between FeO and Fe_2O_3, which is a more valid but still erroneous assumption. The XRF measurements were preceded by TGA, which completely oxidises the Fe(II). Therefore it is impossible to determine the fraction of divalent Fe after the analysis. Despite the uncertainties associated with it, the Fe_2O_3 values will be used to represent

the Fe-contents of the samples. A comparison of the XRF and ICP-OES results reveals a clear one-to-one correlation. The strong correlation between the two independent analyses implies that the measured abundances are representative values.

Various inter-element correlations were investigated for the major elements (Fig. 10). The $\frac{Fe}{Fe+Si}$ ratio represents the relative abundance of Fe-oxides and carbonates with respect to Fe-silicates. If it is high, Fe-carbonates and Fe-oxides are more abundant than Fe-silicates. The ratio will decrease as Fe-silicates become more abundant since the value for the denominator will increase. This ratio has a negative correlation with the SiO_2 abundance in the sample (Fig. 10a). Negative correlations are observed for almost all plots where Fe_2O_3 is on the x-axis, Fe_2O_3-MgO, Fe_2O_3-Al_2O_3, Fe_2O_3-K_2O and Fe_2O_3-Na_2O (Fig. 10b, c, e and g). On the other hand, plots where Al_2O_3, SiO_2 or MgO are on the x-axis display positive correlations with each other as well as with K_2O and Na_2O (Fig. 10d, f and h). Moreover, TiO_2-Al_2O_3 and CaO-MnO display positive correlations and P_2O_5 correlates well with Fe_2O_3 and SiO_2. The major element trends, specifically those in the $\frac{Fe}{Fe+Si}$-SiO_2 plot, can be used to divide the samples in three different groups based on mineralogical content (Fig. 10a). Samples ERI07, ARP09 and ARP11 were not included in any group as their mineralogy is unknown.

The first group is the largest group, comprising 15 out of 21 samples. The abundant minerals in this group are Fe-silicates. Most of the time stilpnomelane is the abundant Fe-silicate, GAS S1, GAS S2, GAS S3, GAS S4, GAS S6, GAS S7, GAS S10, HEX S2, HEX S3, ARP S1, ERI S1 and ERI S2, but in some cases biotite is more abundant, GAS S5, GAS S8 and GAS S11. There are two samples that have a mineralogy with abundant stilpnomelane, yet have a composition that does not fit in this group due to the other minerals present in these samples. First of all, sample HEX S1 has a large abundance of ankerite which results in the SiO_2 content of this sample fitting better with the Fe-carbonate group. Secondly, sample ARP S2 has a mineralogy dominated by stilpnomelane, but the presence of K-feldspar results in an SiO_2 enrichment and Fe_2O_3 depletion compared to the samples in the Fe-silicate group. This is because K-feldspar is the only non-Fe bearing silicate constituting a major mineral fraction. On the other hand, ARP S1 has quartz as most abundant mineral, but since stilpnomelane and biotite are present in significant amounts as well its major element composition fits well within the Fe-silicate group. As this group contains the majority of the samples, the major element composition of these samples generally fits the average composition of the bulk samples for Fe_2O_3 (30-39 wt%), SiO_2 (43-48 wt%), Al_2O_3 (3.75-7.25 wt%), TiO_2 (0.07-0.33 wt%), MnO (0.05-0.33 wt%), P_2O_5 (<0.15 wt%) and LOI (3.09-6.61 wt%). Since there are more Fe-silicates than Fe-carbonates the MgO (4.53-9.57 wt%) abundances are average-to-high and CaO (0.11-0.66 wt%) are below average, the only exception being ERI S1 which is more enriched in CaO and depleted in MgO because it contains more ankerite than the other samples in this group. The common Fe-silicates are all K-bearing which results in an above average K_2O abundance (1.52-4.49 wt%). The Na_2O abundances are low, but samples with abundant stilpnomelane contain more Na_2O (0.36-0.96 wt%) than samples with abundant biotite (0.25-0.35 wt%).

The second group contains samples with a large Fe-oxide and Fe-carbonate mineral fraction. Abundant pyrite is found to coexist with the ankerite, siderite and magnetite. Samples that fit in this group are GAS S9, GAS S12 and HEX S1. A general composition of this group is that it has low SiO_2 concentrations (26-28 wt%) combined with high Fe_2O_3 abundances (35-48 wt%) and a very high LOI (13.8-15.4 wt%). Low abundances are reported for Al_2O_3 (1.9-3.9 wt%), TiO_2 (0.05-0.25 wt%), MgO (3.5-4.5 wt%), Na_2O (0.15-0.55 wt%) and K_2O (1.0-1.25 wt%). The P_2O_5 abundance fits well with the bulk of the samples and enrichments are found for CaO (0.95-8.31 wt%) and MnO (0.40-0.84 wt%). Sample HEX S1 has a slightly different chemical composition than GAS S9 and GAS S12, because it contains abundant stilpnomelane as well as ankerite, but based on its major element composition it fits better in the Fe-carbonate group.

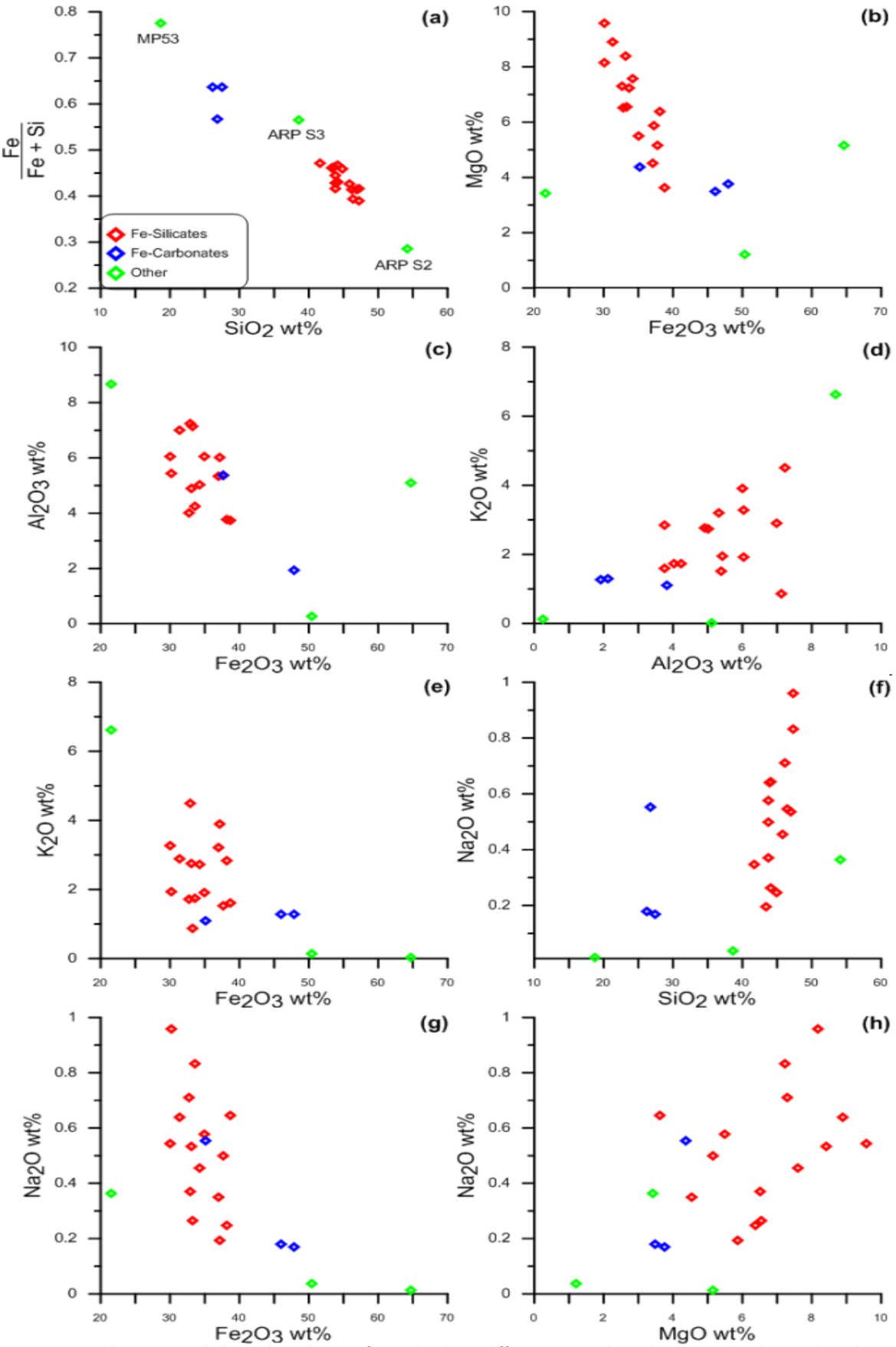

Figure 10: Major element trend plots. The colours refer to the three different mineralogical groups. This division based on mineralogy will be present in all major and trace element plots. Due to their unique mineralogy, the samples from the 'other' group are indicated individually on the SiO_2-$\frac{Fe}{Fe+Si}$ plot. **(10a)**: $\frac{Fe}{Fe+Si}$ vs SiO_2 (wt%) plot. **(10b)**: Fe_2O_3 (wt%) vs. MgO (wt%) plot. **(10c)**: Fe_2O_3 (wt%) vs. Al_2O_3 (wt%) plot. **(10d)**: Al_2O_3 (wt%) vs. K_2O (wt%) plot. **(10e)**: Fe_2O_3 (wt%) vs. K_2O (wt%) plot. **(10f)**: SiO_2 (wt%) vs. Na_2O (wt%) plot. **(10g)**: Fe_2O_3 (wt%) vs. Na_2O (wt%) plot. **(10h)**: MgO (wt%) vs. Na_2O (wt%) plot.

Wt% Oxide	GAS S1	GAS S2	GAS S3	GAS S4	GAS S5	GAS S6	GAS S7	GAS S8	GAS S9	GAS S10	GAS S11	GAS S12	HEX S1	HEX S2	HEX S3	ARP S1	ARP S2	ARP S3	ARP 09	ARP 11	ERI S1	ERI S2	ERI 07	MP53
SiO_2	47.3	47.3	47.0	46.2	44.9	45.8	46.5	43.4	27.4	43.8	41.7	26.2	26.8	43.8	43.9	44.1	54.1	38.6	47.8	51.9	44.1	43.7	47.9	18.7
Al_2O_3	5.43	4.25	4.90	4.02	3.76	5.03	6.05	6.01	1.92	7.24	5.32	2.13	3.84	6.04	7.00	7.13	8.68	0.26	7.26	7.45	3.75	5.38	7.66	5.11
TiO_2	0.14	0.07	0.07	0.11	0.22	0.26	0.11	0.22	0.05	0.16	0.31	0.07	0.27	0.81	0.14	0.57	0.47	0.01	0.39	0.46	0.16	0.33	0.39	0.05
Fe_2O_3	30.2	33.7	33.2	32.7	38.2	34.2	30.1	37.2	47.9	32.9	37.0	46.0	35.1	35.0	31.4	33.3	21.6	50.4	22.1	23.7	38.8	37.7	23.1	64.7
MnO	0.33	0.17	0.05	0.11	0.09	0.04	0.06	0.10	0.67	0.11	0.06	0.41	0.84	0.33	0.09	0.13	0.23	0.17	1.31	0.34	0.31	0.21	1.36	0.26
CaO	0.57	0.16	0.14	0.90	0.23	0.21	0.18	0.14	0.95	0.19	0.14	2.67	8.31	0.66	0.11	0.45	0.26	1.22	1.04	1.11	0.98	0.22	1.29	1.24
MgO	8.17	7.23	8.40	7.29	6.37	7.58	9.57	5.88	3.76	6.51	4.53	3.49	4.37	5.51	8.90	6.56	3.42	2.49	3.87	4.06	3.62	5.16	4.65	5.15
Na_2O	0.96	0.83	0.53	0.71	0.25	0.46	0.54	0.19	0.17	0.37	0.35	0.18	0.55	0.58	0.64	0.26	0.36	0.04	0.27	0.56	0.64	0.50	0.49	0.01
K_2O	1.94	1.74	2.76	1.72	2.83	2.73	3.28	3.90	1.27	4.49	3.20	1.29	1.09	1.91	2.90	0.87	6.62	0.13	5.43	5.34	1.60	1.52	4.43	0.02
P_2O_5	0.01	0.05	0.02	0.04	0.03	0.03	0.01	0.01	0.21	0.02	0.03	0.00	0.07	0.11	0.01	0.12	0.07	0.11	0.08	0.09	0.14	0.07	0.09	0.81
LOI	5.36	4.71	3.66	6.59	3.84	3.64	4.24	3.09	15.39	3.82	6.61	13.81	14.11	4.42	4.68	5.02	2.38	3.76	9.53	5.64	4.93	5.09	8.72	4.19
Sum	100.4	100.2	100.7	100.4	100.7	100.0	100.6	100.2	99.8	99.6	99.3	96.3	95.4	99.1	99.8	98.5	98.3	97.2	99.1	100.6	99.0	99.9	100.1	100.2
TC	0.15	-0.02	-0.01	0.56	0.30	-0.01	-0.01	0.17	3.89	0.28	2.66	3.68	5.23	0.23	-0.01	0.12	0.04	1.09	2.04	0.45	0.48	0.46	1.55	0.18
TIC	0.08	-0.01	-0.03	0.17	0.01	-0.02	-0.02	-0.02	0.06	-0.01	-0.01	0.68	2.35	0.11	-0.02	0.05	0.01	0.64	-	-	0.20	-0.02	-	0.09
TOC	0.07	-0.01	0.02	0.39	0.29	0.01	0.01	0.19	3.83	0.29	2.67	3.00	2.88	0.13	0.02	0.06	0.03	0.45	-	-	0.28	0.47	-	0.09
TS	0.04	0.03	0.03	0.04	0.04	0.04	0.03	0.04	4.07	0.02	0.40	8.45	2.02	0.12	0.03	0.08	0.07	5.67	0.12	0.21	0.91	0.07	0.14	0.05
‰																								
$\delta^{34}S$	-	-	-	-	-	-	-	-	-5.33	-	-0.24	-0.92	21.7	5.86	-	4.38	4.11	9.56	2.34	0.88	4.25	-	2.90	-
$\Delta^{33}S$	-	-	-	-	-	-	-	-	-0.11	-	0.40	0.52	-0.10	1.40	-	0.97	-0.16	0.07	-0.12	-0.20	0.27	-	-0.18	-
$\Delta^{36}S$	-	-	-	-	-	-	-	-	-0.01	-	-1.45	-1.73	0.16	-0.47	-	-0.41	-0.04	-0.22	0.37	0.18	-0.88	-	0.10	-
ppm																								
Li	2.25	2.71	18.5	2.96	8.87	15.93	59.3	5.87	0.95	3.88	5.14	0.44	2.35	18.1	20.6	16.9	8.78	9.32	10.9	24.1	1.61	6.08	14.9	15.6
Be	0.08	2.74	1.75	1.97	1.93	2.29	2.03	2.66	2.43	3.13	1.92	1.53	0.42	0.86	0.11	0.84	0.82	0.30	1.02	0.95	1.14	0.86	0.82	1.31
Sc	2.20	1.38	1.75	4.80	2.77	4.54	1.19	5.34	1.86	3.33	13.6	2.43	9.34	13.5	2.87	0.29	9.94	11.7	7.39	7.16	4.73	5.79	7.30	1.95
V	6.57	17.0	3.86	38.5	20.5	6.13	5.62	50.9	25.0	32.8	68.8	29.5	115	168	4.84	3.99	83.4	130	56.6	53.0	34.0	53.2	54.8	12.1
Cr	6.63	12.0	3.10	23.3	15.0	2.45	1.26	16.7	13.9	16.4	72.4	13.1	76.5	69.2	3.77	2.27	115	75.2	69.9	80.2	33.9	68.6	72.6	11.6
Co	32.1	33.6	17.1	19.1	22.4	15.3	9.63	13.3	17.2	11.2	31.7	35.7	77.4	27.3	7.31	23.2	27.6	32.4	10.4	11.7	21.9	48.1	9.57	34.2
Ni	3.00	5.06	2.26	12.4	13.7	6.09	4.35	66.9	14.1	17.6	170	175	101	36.7	2.43	9.66	40.5	40.9	32.0	30.8	28.4	32.9	31.3	10.1
Cu	2.27	3.81	2.07	3.46	2.93	2.31	1.64	1.51	32.76	2.80	4.75	55.5	34.6	86.1	1.19	14.4	23.4	54.4	26.6	41.1	82.0	26.1	22.2	2.83
Zn	48.1	23.8	23.3	70.9	33.1	31.1	34.3	133	79.4	53.0	84.7	73.6	21.7	43.7	11.2	7.94	26.2	39.1	22.3	16.0	24.0	35.5	29.8	43.2
Rb	190	187	404	167	434	401	481	742	212	760	537	167	83.0	128	331	57.7	202	9.22	168	189	133	88.7	119	2.57
Sr	27.6	17.0	27.2	31.0	13.6	34.7	30.8	17.0	21.1	24.4	18.1	221	25.8	19.4	11.5	10.5	21.0	25.6	30.2	35.9	8.46	7.45	25.6	18.4
Zr	158	53.8	93.6	44.9	102	282	211	118	11.3	75.6	85.2	16.1	65.8	101	185	90.9	95.9	3.08	69.8	113	45.5	64.4	66.3	44.7
Nb	7.12	2.36	8.28	3.27	4.58	11.8	18.3	12.8	1.14	14.3	5.80	1.69	3.40	5.16	6.74	4.83	5.58	0.10	7.60	7.40	2.70	4.03	8.10	3.16
Mo	0.02	0.04	0.12	0.27	0.21	0.68	0.22	0.40	3.81	0.16	2.83	1.03	3.28	0.81	0.07	0.58	0.90	0.34	1.09	1.13	0.40	0.62	0.91	0.38
Cs	48.5	51.2	52.9	31.7	46.9	51.9	52.5	50.3	23.0	51.4	53.8	20.2	14.8	30.1	42.4	14.8	22.0	1.53	16.5	22.1	27.7	24.4	15.3	2.15
Ba	191	96.8	67.3	89.2	39.1	89.3	132	111	32.3	219	155	50.3	65.1	162	183	60.7	380	30.5	355	365	215	114	317	12.5
Hf	4.18	1.67	2.80	1.33	2.06	6.56	6.55	3.44	0.30	2.67	2.26	0.35	1.70	2.70	5.05	2.55	2.80	0.11	2.04	3.29	1.29	1.90	1.99	1.40
Ta	0.47	0.52	0.77	0.23	0.28	0.84	2.05	1.30	0.06	1.31	0.70	0.08	0.41	0.48	0.52	0.03	0.61	0.50	-	-	0.26	0.45	-	0.58
Re	0.01	0.01	0.01	0.01	0.01	0.01	0.01	0.01	0.01	0.01	0.02	0.01	0.03	0.01	0.00	0.01	0.01	0.01	0.05	0.05	0.01	0.01	0.06	0.01
Tl	0.42	0.40	0.80	0.73	0.72	0.90	0.84	0.97	0.98	1.63	1.42	3.16	1.64	0.32	0.47	0.20	0.32	0.19	-	-	0.46	0.25	-	0.43
Pb	5.09	4.00	4.08	5.62	3.77	3.57	4.55	3.88	22.2	6.13	22.0	41.7	30.8	7.86	2.60	5.13	5.44	9.04	3.79	4.09	10.9	3.82	5.87	6.39
Th	8.13	12.6	15.9	3.25	8.84	9.57	32.5	21.2	0.94	24.6	7.91	1.16	5.99	3.69	9.30	6.31	10.2	0.18	7.31	11.0	4.54	6.45	7.34	11.4
U	2.34	1.20	1.41	0.94	1.64	1.08	4.60	4.68	0.34	6.00	2.51	0.33	1.34	0.96	1.63	1.51	2.83	0.06	1.79	2.29	1.41	1.73	1.75	5.17

ppm	GAS S1	GAS S2	GAS S3	GAS S4	GAS S5	GAS S6	GAS S7	GAS S8	GAS S9	GAS S10	GAS S11	GAS S12	HEX S1	HEX S2	HEX S3	ARP S1	ARP S2	ARP S3	ARP 09	ARP 11	ERI S1	ERI S2	ERI 07	MP53
La	6.62	6.04	2.87	11.0	12.6	49.5	37.5	22.0	5.66	30.5	21.9	5.15	2.29	11.1	58.2	15.3	22.0	1.45	16.8	19.5	16.3	6.79	16.2	31.0
Ce	15.3	12.6	6.57	22.7	26.7	119	78.8	44.4	12.1	59.0	44.0	9.99	5.78	24.1	129	31.4	45.8	2.58	30.4	34.2	27.5	14.7	31.3	66.5
Pr	1.89	1.38	0.84	2.80	3.03	14.2	8.64	4.97	1.72	6.19	5.19	1.26	1.01	3.14	15.1	3.83	5.33	0.39	3.86	4.42	2.92	1.83	3.65	8.08
Nd	7.19	4.70	3.47	10.3	10.4	50.3	27.7	16.9	7.76	20.0	19.0	5.11	4.93	12.7	48.2	14.6	18.7	1.99	13.9	15.8	9.76	7.07	13.1	29.2
Sm	1.41	0.77	0.79	1.73	1.56	8.01	4.96	2.87	2.17	3.33	3.17	1.10	1.10	2.98	5.82	3.03	3.31	0.39	2.67	2.95	1.34	1.45	2.54	4.58
Eu	0.23	0.17	0.11	0.29	0.25	1.13	0.28	0.38	0.74	0.49	0.47	0.25	0.26	0.67	0.56	0.60	0.62	0.14	0.59	0.58	0.22	0.30	0.51	0.74
Gd	1.41	0.76	0.79	1.51	1.22	4.87	3.90	2.15	2.74	2.66	2.42	1.18	1.36	3.02	3.20	3.05	2.58	0.53	2.43	2.42	1.25	1.44	2.27	4.06
Tb	0.23	0.10	0.11	0.20	0.14	0.45	0.50	0.23	0.40	0.32	0.26	0.17	0.23	0.43	0.29	0.43	0.31	0.07	0.36	0.33	0.15	0.21	0.34	0.44
Dy	1.66	0.77	0.76	1.43	0.95	2.44	3.24	1.32	2.71	2.09	1.59	1.23	1.96	2.94	1.47	3.12	1.90	0.55	2.12	1.83	1.06	1.51	2.06	2.77
Y	9.24	5.09	3.74	8.46	5.95	11.2	14.3	5.30	15.5	10.5	8.17	8.23	15.2	15.3	5.77	16.4	8.57	4.76	12.3	8.42	8.27	9.26	11.5	24.8
Ho	0.33	0.16	0.13	0.27	0.19	0.42	0.59	0.22	0.50	0.39	0.27	0.25	0.46	0.57	0.24	0.62	0.34	0.11	0.38	0.31	0.22	0.31	0.37	0.54
Er	1.00	0.49	0.35	0.78	0.56	1.25	1.67	0.64	1.33	1.21	0.80	0.76	1.53	1.69	0.66	1.80	0.97	0.31	1.16	0.95	0.66	0.92	1.15	1.45
Tm	0.17	0.09	0.06	0.13	0.10	0.20	0.27	0.12	0.20	0.23	0.15	0.14	0.27	0.27	0.10	0.27	0.15	0.05	0.18	0.15	0.10	0.15	0.18	0.20
Yb	1.12	0.64	0.36	0.88	0.64	1.38	1.78	0.93	1.33	1.72	1.14	1.07	1.96	1.80	0.62	1.75	1.04	0.32	1.14	1.01	0.67	1.00	1.13	1.20
Lu	0.18	0.11	0.06	0.15	0.11	0.21	0.26	0.17	0.21	0.29	0.23	0.20	0.36	0.28	0.09	0.27	0.16	0.05	0.17	0.16	0.11	0.16	0.17	0.20
Ratios																								
La/La*	0.85	0.86	1.02	0.89	0.83	0.73	0.79	0.88	1.38	0.90	0.95	1.18	1.55	1.01	0.69	0.98	0.86	3.51	0.95	0.95	1.07	0.95	0.97	0.85
Ce/Ce*	0.96	0.97	1.02	0.93	0.94	0.92	0.93	0.96	1.05	0.98	0.97	1.02	0.99	0.98	0.86	0.98	0.94	1.22	0.89	0.87	0.99	0.98	0.97	0.93
Pr/Pr*	1.02	1.01	0.99	1.04	1.03	1.04	1.04	1.02	0.98	1.01	1.02	0.99	1.00	1.01	1.09	1.01	1.03	0.94	1.06	1.07	1.01	1.01	1.02	1.04
Nd/Nd*	0.98	1.01	0.94	1.04	1.06	1.05	0.94	1.00	0.86	0.98	1.05	0.97	1.02	0.92	1.10	0.96	0.99	1.13	0.97	0.98	1.08	0.97	0.97	1.07
Sm/Sm*	1.07	0.85	1.27	0.98	0.94	1.02	1.48	1.09	0.77	1.03	1.03	0.92	0.92	0.97	0.96	0.99	0.96	0.67	0.91	0.95	0.89	0.97	0.96	0.96
Eu/Eu*	0.86	1.22	0.73	0.98	0.99	0.98	0.34	0.86	1.71	0.91	0.95	1.22	1.12	1.23	0.69	1.09	1.16	1.78	1.23	1.16	0.95	1.13	1.12	0.99
Gd/Gd*	0.99	1.09	1.06	1.08	1.11	1.11	1.05	1.15	1.13	1.10	1.14	1.07	1.00	1.07	1.07	1.07	1.10	1.22	1.02	1.02	1.17	1.05	0.99	1.22
Tb/Tb*	0.92	0.86	0.93	0.86	0.85	0.80	0.89	0.85	0.92	0.86	0.85	0.91	0.87	0.92	0.80	0.89	0.87	0.83	1.00	1.00	0.82	0.90	1.01	0.83
Dy/Dy*	1.11	1.10	1.13	1.12	1.05	1.01	1.09	1.07	1.11	1.08	1.08	1.08	1.07	1.08	1.00	1.09	1.07	1.11	1.05	1.03	1.06	1.08	1.05	1.03
Y/Y*	1.19	1.55	1.81	1.23	2.06	1.01	1.07	1.89	1.50	1.66	3.13	1.42	1.20	1.38	1.31	1.03	1.25	1.62	1.33	1.52	1.60	1.15	1.52	1.79
Ho/Ho*	0.98	0.97	0.98	0.97	0.98	0.93	0.97	0.92	1.00	0.93	0.92	0.97	1.00	0.99	0.94	1.01	0.97	1.05	0.92	0.90	1.01	1.00	0.93	1.04
Er/Er*	0.96	0.93	0.90	0.93	0.93	0.95	0.94	0.86	0.95	0.90	0.89	0.92	0.96	0.97	0.97	0.98	0.94	0.96	1.00	0.98	0.98	0.96	1.01	0.99
Tm/Tm*	1.05	1.06	1.10	1.07	1.08	1.04	1.05	1.06	1.02	1.05	1.04	1.02	1.06	1.03	1.00	1.04	1.04	1.01	1.05	1.04	1.05	1.05	1.04	1.00
Yb/Yb*	0.97	0.96	0.94	0.91	0.93	0.98	0.99	0.94	0.96	0.98	0.89	0.93	0.92	0.98	0.98	0.96	0.96	1.01	0.97	0.96	0.92	0.94	0.97	0.89
Lu/Lu*	1.06	1.07	1.15	1.21	1.16	1.04	1.01	1.12	1.09	1.03	1.23	1.12	1.17	1.04	1.04	1.08	1.09	0.97	1.06	1.08	1.19	1.12	1.05	1.29
Y/Ho	31.6	41.9	44.8	31.9	54.3	26.2	27.2	48.9	37.4	44.7	82.0	38.0	33.3	36.1	32.8	26.6	31.9	40.9	46.6	47.6	42.0	45.9	45.6	44.6
$(Pr/Yb)_{SN}$	0.50	0.64	0.70	0.94	1.39	3.06	1.44	1.59	0.38	1.07	1.36	0.35	0.15	0.52	7.29	0.65	1.53	0.37	1.00	1.30	1.30	0.54	0.96	2.00
$(Pr/Dy)_{SN}$	0.60	0.94	0.58	1.03	1.68	3.07	1.40	1.98	0.33	1.56	1.72	0.54	0.27	0.56	5.41	0.64	1.47	0.37	0.96	1.27	1.44	0.64	0.93	1.53
$(Dy/Yb)_{SN}$	0.84	0.68	1.20	0.92	0.83	1.00	1.03	0.80	1.16	0.69	0.79	0.65	0.56	0.92	1.35	1.01	1.04	0.98	1.05	1.02	0.90	0.85	1.03	1.31

Table 6: Chemical composition of the stilpnomelane lutites. Major element data was obtained via XRF fusion bead analysis and is reported as weight percent (wt%) oxide. The TC, TIC, TOC and TS data were obtained via CS-analyser and are reported in wt%. Sulphur isotope data was obtained via EA-IRMS following S-extraction and is reported in per mille (‰) values. Delta (δ and Δ) values were determined using Eq. 6 and Eq. 7. Trace element data was obtained mainly using ICP-MS and is reported in parts per million concentration (ppm). For Y values from the XRF pressed powder pellet analysis were used where available, since the recoveries of the ICP-MS and ICP-OES are anomalously low for Y in ICP methods. A detailed description of the recoveries of the various analytical techniques can be found in Appendix B. Full XRF, ICP-OES and ICP-MS data sets can be found in Appendix C, D and E respectively. Values indicated in red are those that are below the detection limit of the respective instrument. Values in blue are those that have values above two times the highest calibration. Both should be taken as indicative value as they may contain an error of analysis larger than 10%. If a value is indicated with a '-', it was not measured. Major and trace element as well as TC/TS data of samples ARP09, ARP11 and ERI07 courtesy of P.B.H. Oonk (personal comm.).

The third group comprises individual samples that do not fit in the Fe-carbonate and Fe-silicate groups. Samples in this group are ARP S2, ARP S3 and MP53. The mineralogy of these different samples varies significantly. ARP S2 has a mineralogy with abundant stilpnomelane, but it does not fit within the Fe-silicate group because it also contains K-feldspar. Due to its mineralogy ARP S2 is enriched in SiO_2, Al_2O_3 and K_2O and depleted in Fe_2O_3 and MgO compared to the Fe-silicate group samples. Sample ARP S3 has a mineralogy dominated by quartz and magnetite with minimal stilpnomelane, resulting in lower SiO_2 and higher Fe_2O_3 contents than Fe-silicates. Together Fe and Si comprise 89.03 wt% of the sample. Since there are nearly no Fe-silicates in this sample it is depleted in Al_2O_3, MgO and K_2O compared to other samples and its TiO_2, MnO, Na_2O and P_2O_5 contents are among the lowest reported (Table 6). An elevated CaO content can be explained by the presence of ankerite. The mineralogy of sample MP53 is comprised mostly of hematite. This is reflected in the composition of the sample which is enriched in Fe_2O_3 an depleted in SiO_2. There is no stilpnomelane or biotite in this sample which is reflected by the very low abundance of K_2O. The average Al_2O_3 and MgO contents are the result of clinochlore, which is the only silicate mineral that is present. There is also a relatively high CaO content compared to the bulk samples, but no carbonate minerals were identified.

Trace Element Geochemistry

Trace element abundances in stilpnomelane lutites are higher than in the rest of the BIF (e.g. Beukes and Klein, 1990; Horstmann and Halbich, 1995). In this study most trace elements are present on a 1-200 ppm scale. The only element consistently below the 1 ppm concentration is Re (4-29 ppb), other elements that are below 1 ppm in some samples are Li, Be, Mo, Tl, Th and U. The most abundant trace element is Rb which is often present in >200 ppm concentrations. Other elements that are occasionally present above 200 ppm are Sr (221 ppm), Zr (282 ppm) and Ba (380 ppm; Table 6). Recoveries were determined using the international reference material ISE-921. This revealed low recoveries for Y and Zr as well as high recoveries for V, Cu, Co and Tl. The sources of these anomalous recoveries are discussed in Appendix B.

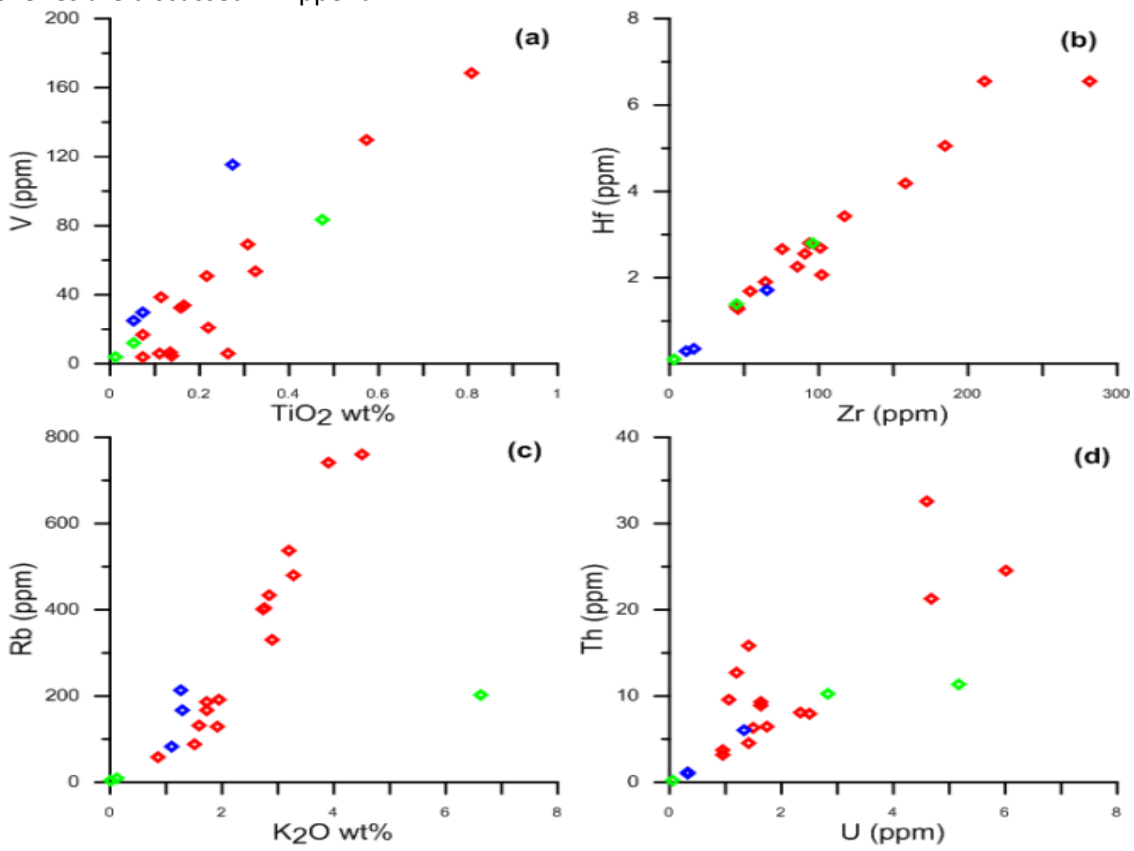

Figure 11: Major-trace and trace-trace element correlations for elements that are both in the same chemical group. **(11a):** Transition metals: TiO_2 (wt%) vs. V (ppm). **(11b):** High-field strength elements (HFSE): Zr (ppm) vs. Hf (ppm). **(11c):** Large ion lithophile elements (LILE): K_2O (wt%) vs. Rb (ppm). One sample deviates from the trend, ARP S2, since it is K-feldspar bearing. **(11d):** HFSE plot: U (ppm) vs. Th (ppm).

Major-trace and trace-trace element correlations are relatively common, but most of these correlations are related to elements that are known to display similar behaviour. Groups of elements that show strong correlations are the transition metals V, Cr and Ti, the large ion lithophile elements (LILE) Rb, K, Cs, Sr and Ba and the high field strength elements (HFSE) Zr, Hf, Th and the REY (Fig. 11). The observed trends can all be explained by similar chemical behaviour of the elements within each of the groups. Correlations between elements within a group may vary based on ionic radius, for example Zr and Hf correlate better with LREE than HREE while Y correlates better with HREE than LREE.

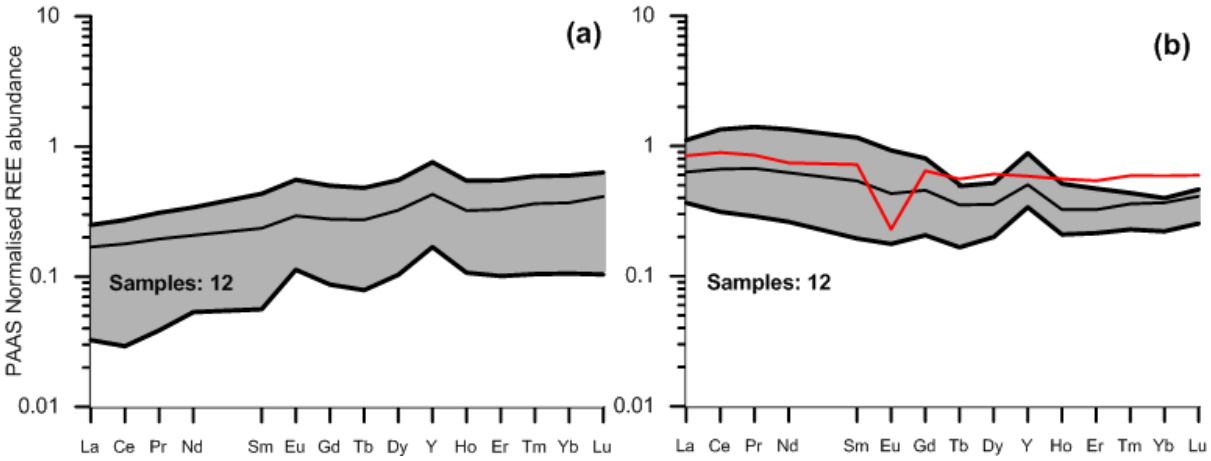

Figure 12: PAAS normalized rare-earth element plots. The shaded areas represent the range between the most enriched and most depleted sample within the group while the middle line represents the average REE composition of the LREE depleted samples. **(12a):** REE composition of LREE depleted samples. **(12b):** REE composition of LREE enriched samples. The red line corresponds with sample GAS S7 which was plotted separately due to its pronounced negative Eu-anomaly $((Eu/Eu^*)_{SN}=0.34)$.

The PAAS normalized REY composition of the samples shows a large variability. There are twelve samples which display a LREE enriched pattern ($(Pr/Yb)_{SN}>1.0$) and twelve which show a LREE depleted pattern ($(Pr/Yb)_{SN}<1.0$; Table 6; Fig. 12). The values range between 0.15 and 3.06 with one sample showing a stronger LREE enrichment, sample HEX S3 with $(Pr/Yb)_{SN}=7.29$. Further examination of $(Pr/Yb)_{SN}$ shows that it correlates well with the sum of REE (∑REE) as well as the shale normalised sum of REE ($(\sum REE)_{SN}$). This correlation is stronger for the non-shale normalised ∑REE ($R^2=0.755$) than for the shale normalised $(\sum REE)_{SN}$ ($R^2=0.425$). The LREE are present in significantly higher absolute abundances than HREE and thus dominate the ∑REE. Subsequent shale normalization removes this effect, but the trend remains. One sample deviates from the trend, which is HEX S3 as it has an anomalously high $(Pr/Yb)_{SN}$ ratio. Comparing the $(Pr/Yb)_{SN}$ ratios with the mineralogy reveals that the most LREE depleted samples are those with a less abundant Fe-silicates and more Fe-carbonates, -oxides and quartz. On the other hand, LREE enriched samples contain more abundant Fe-silicates. There is an apparent relationship between biotite presence and LREE enrichments as all samples without Fe-carbonates and with abundant biotite have $(Pr/Yb)_{SN} > 1$. Dividing the $(Pr/Yb)_{SN}$ ratio in a LREE and a HREE component, $(Pr/Dy)_{SN}$ and $(Dy/Yb)_{SN}$ respectively, shows that the $(Pr/Yb)_{SN}$ is dominated by LREE variability (Fig. 13). This is supported by the REE patterns as PAAS normalized abundances also show an overlap for the HREE abundances for LREE enriched and

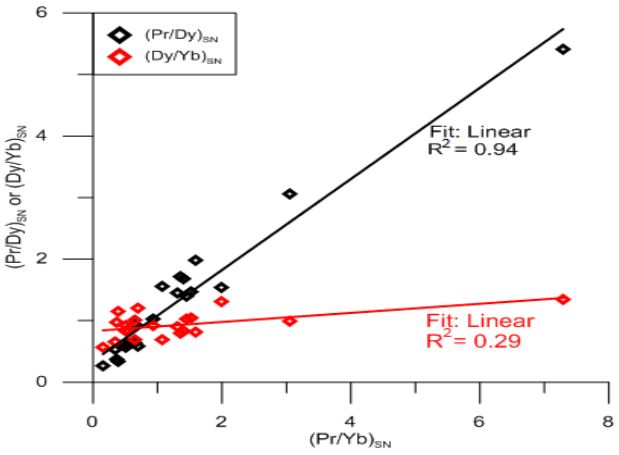

Figure 13: Shale normalised Pr/Yb plotted against the LREE and HREE fraction of the $(Pr/Yb)_{SN}$ ratio with the division between LREE and HREE chosen at Dy.

LREE depleted samples, while LREE abundances vary largely (Fig. 12). When individual elements are observed, both positive and negative anomalies are observed (Table 6). La and Eu have variable abundances displaying both positive and negative anomalies. Positive La anomalies are only observed in samples which are from the Fe-carbonate group (GAS S9, GAS S12, HEX S1) and ARP S3. On the other hand, negative La anomalies are abundant in Fe-silicate group samples. The variability in Eu anomalies cannot be directly related to mineralogical groups. No Ce-anomaly is observed in all but two cases, one positive (ARP S3) and one negative (HEX S3) anomaly were observed. Sm/Sm* ratios indicate that there are Sm anomalies, but the REY plots do not show these anomalies. Since Sm* is determined using Eu abundances, variations in Eu will have a large effect on the Sm/Sm* ratio. Therefore these values do not represent the actual Sm anomaly, but instead show the effects of varying Eu abundances on the Sm anomaly. Small, but consistent, negative anomalies are observed for Tb and Yb while Lu and Gd show small positive anomalies. Yttrium also shows consistent positive anomalies. The observed Y/Ho ratios are always above the chondritic Y/Ho ratio, $(Y/Ho)_{CI} \approx 26$, which corresponds well with that of PAAS $(Y/Ho)_{PAAS} = 25.94$, but not always above the present-day marine Y/Ho, $(Y/Ho)_{Seawater} \geq 44$ (Table 6; Bolhar et al., 2004; Pourmand et al., 2012).

Carbon and Sulphur Content and Quadruple Sulphur Isotopes

The carbon and sulphur (CS) contents of the samples show large variability, with several orders of magnitude differences between samples (Table 6). Sulphur contents are all above the detection limit, but for the carbon content five samples show values below the detection limit. Moreover, for the TIC there are nine samples below the detection limit while the TOC only shows one negative value.

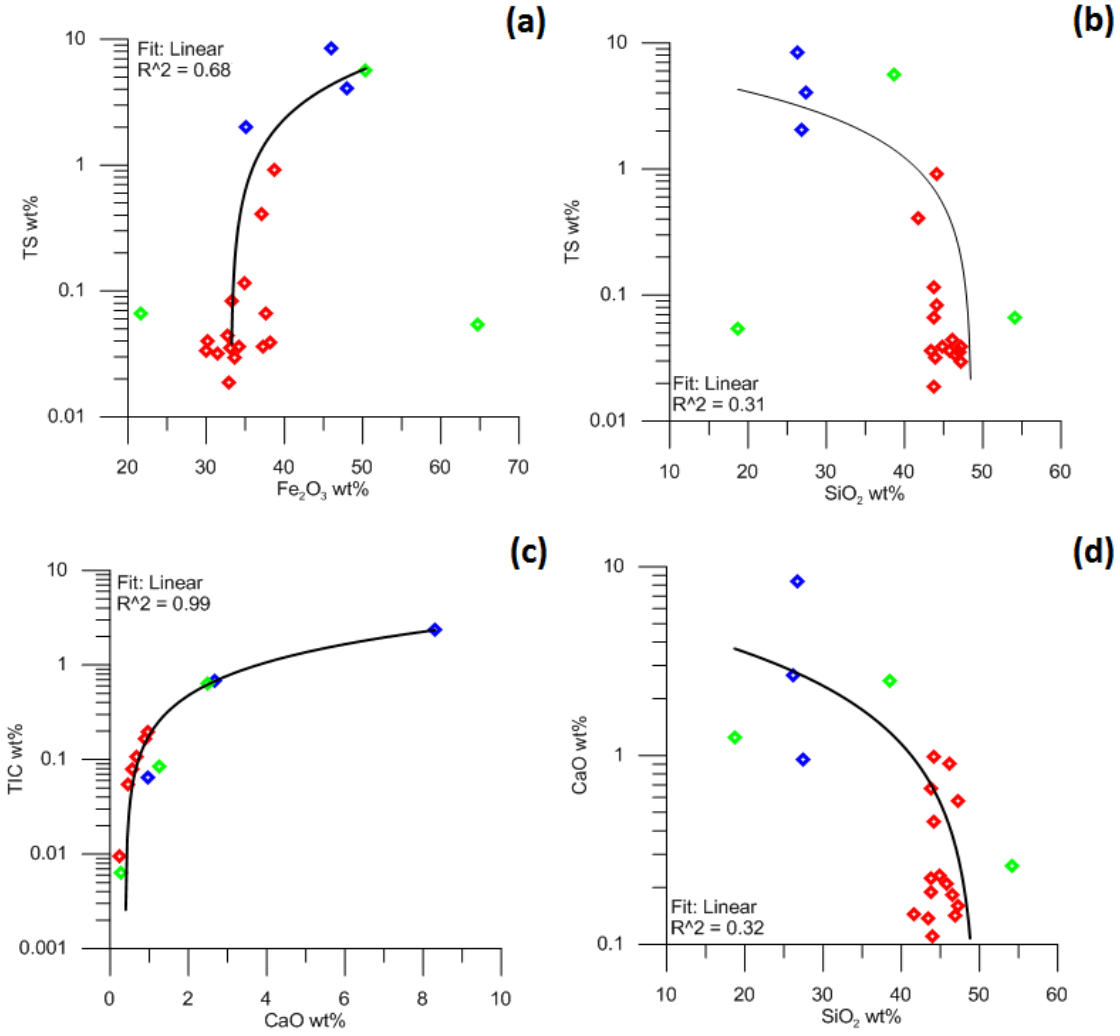

Figure 14: Major element and Major element-CS plots. **(14a):** Fe_2O_3 (wt%) vs. TS (wt%) plot. Sample MP53 does not correlate. **(14b):** SiO_2 (wt%) vs. TS (wt%) plot. Sample MP53 does not correlate. **(14c):** CaO (wt%) vs. TIC (wt%) plot. **(14d):** SiO_2 (wt%) vs. CaO (wt%) plot.

However, since the TOC is determined by subtracting the TIC from the TC, the TOC data is limited to those samples where neither TIC or TC is negative. The quadruple sulphur isotope data contains values for three additional samples, on top of the nine that were selected from this study, which are ARP09, ARP11 and ERI07 (Table 6; P.B.H. Oonk, personal comm.). The CS content correlates well with the mineralogy. Samples with high carbon content are those with abundant Fe-carbonate minerals, ankerite and siderite, while the abundance of pyrite is the main control on the sulphur content. The samples that contain a large fraction of carbonate minerals, GAS S12 and HEX S1, show the highest TIC. This is expected as the carbon is incorporated in the crystal structure of these minerals. The third sample from the Fe-carbonate group, GAS S9, does not show a large TIC fraction (0.06 wt%) but instead shows high TOC (3.83 wt%). Other samples with high organic carbon contents are GAS S4, GAS S10, GAS S11 and ERI S2, all of which contain either no or minimal amounts of ankerite. The sulphur and carbon contents correlate well with some of the major element abundances. Positive correlations are found for Fe_2O_3-TS as well as CaO and MnO with TC, TIC and TOC (Fig. 14a and c). On the other hand, the elements concentrated in Fe-silicates, Al_2O_3, SiO_2, MgO and K_2O, show no or negative correlations with CaO, TC, TS, TIC and TOC (Fig. 14b and d).

Carbon concentrations have been measured with the CS-analyser only, but sulphur concentrations were also determined using ICP-OES. The results from both analyses were compared to test reliability. Using only samples where ICP-OES values were above the detection limit, the sulphur contents almost plot on a one-to-one line. There is a minor misfit up to 0.2 wt%, except for GAS S9 which has a 0.73 wt% misfit, which indicates that the sulphur concentrations are representative values. These values were used to determine the samples used for the sulphur extractions. They were also used for calculating the recovery of these extractions. Recoveries were computed by first

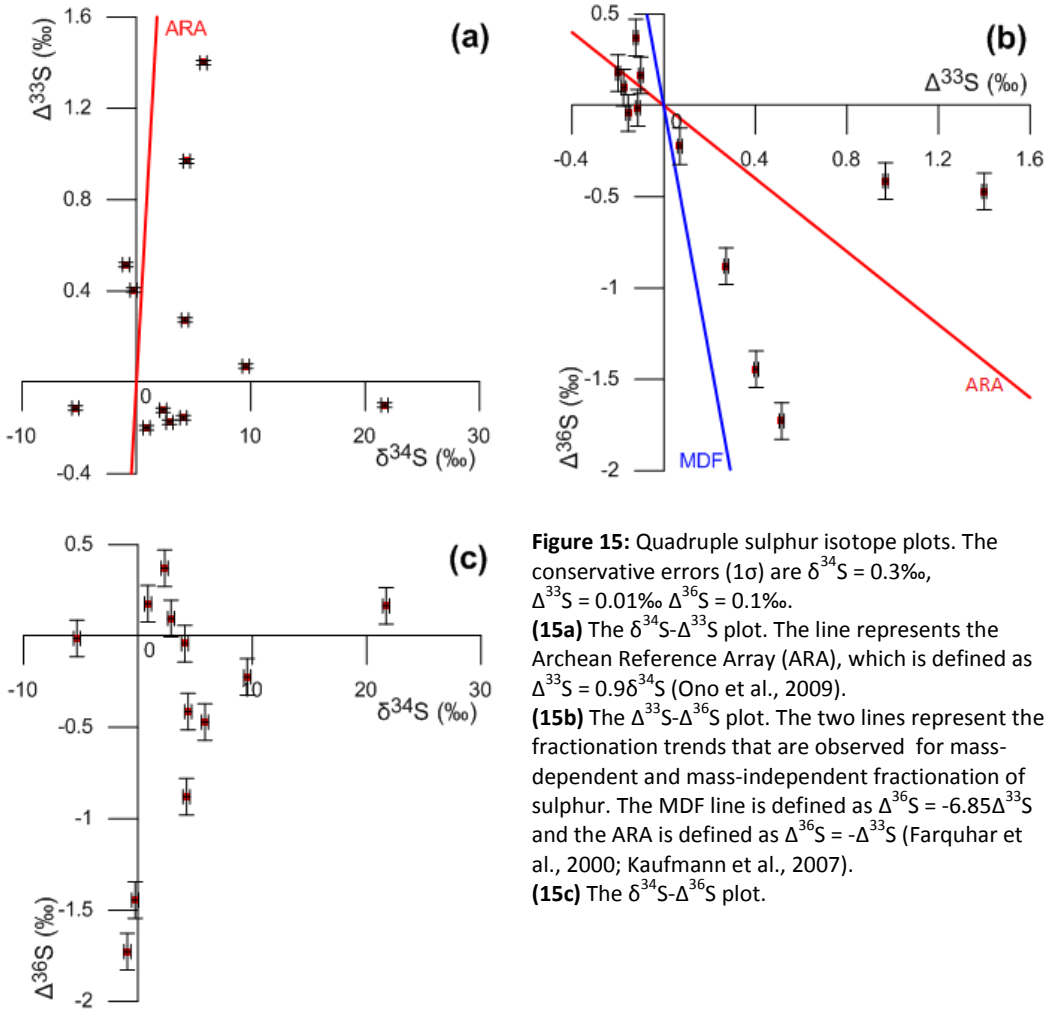

Figure 15: Quadruple sulphur isotope plots. The conservative errors (1σ) are $\delta^{34}S$ = 0.3‰, $\Delta^{33}S$ = 0.01‰ $\Delta^{36}S$ = 0.1‰.
(15a) The $\delta^{34}S$-$\Delta^{33}S$ plot. The line represents the Archean Reference Array (ARA), which is defined as $\Delta^{33}S = 0.9\delta^{34}S$ (Ono et al., 2009).
(15b) The $\Delta^{33}S$-$\Delta^{36}S$ plot. The two lines represent the fractionation trends that are observed for mass-dependent and mass-independent fractionation of sulphur. The MDF line is defined as $\Delta^{36}S = -6.85\Delta^{33}S$ and the ARA is defined as $\Delta^{36}S = -\Delta^{33}S$ (Farquhar et al., 2000; Kaufmann et al., 2007).
(15c) The $\delta^{34}S$-$\Delta^{36}S$ plot.

determining the expected yield by rewriting Equation 10. Since the amount of sample that was placed in the round-bottom flask is a known factor, the expected yield can be calculated. This value represents the amount of Ag_2S that would be retrieved in an ideal situation. The recovery can then be computed by dividing the measured yield over the expected yield. The recoveries that have been obtained for the sulphur extractions in Münster are between 86.7 and 114.1% for all samples except ARP S3, indicating reliable results. Sample ARP S3 had a lower recovery, 60.2%, because it was not heated during extraction. Lower recoveries indicate that only parts of the sulphur was liberated, which could affect the results as the isotopic composition may vary with location in a grain (Gregory et al., 2015). There will always be a scatter in the recoveries which causes them to deviate from 100% as there are errors associated with both the extraction process and the TS data that was used to compute the recoveries.

The quadruple sulphur isotope data shows that there is a large variability in the isotopic composition of the samples (Fig. 15). The MDF isotope ratio, $\delta^{34}S$, displays large variability from slightly negative, GAS S9, to strong positive, HEX S1, values with the majority clustering around zero. The mass independent $\Delta^{33}S$ shows values that are positive or very slightly negative while $\Delta^{36}S$ values are mostly negative with some slightly positive values. In the $\delta^{34}S$-$\Delta^{33}S$ plot most of the samples cluster around the Archean Reference Array (ARA), but the large variability in $\delta^{34}S$ for samples with slightly negative $\Delta^{33}S$ imply the influence of multiple processes on the isotopic composition (Fig. 15a). In the $\Delta^{33}S$-$\Delta^{36}S$ plot the majority of samples cluster around the origin (Fig. 15b). Three samples, GAS S11, GAS S12 and ERI S1, show a $\Delta^{36}S$ depletion compared to MIF. The array between the MIF and MDF reference arrays has a slope $\Delta^{36}S/\Delta^{33}S \approx -3.3$. Furthermore, samples HEX S2 and ARP S1 show $\Delta^{36}S$ enrichment compared to MIF and have a slope $\Delta^{36}S/\Delta^{33}S \approx -0.5$.

VII: Discussion

Mineralogical Composition

The negative correlations for $\frac{Fe}{Fe+Si}$-SiO_2, Fe_2O_3-Al_2O_3 and Fe_2O_3-MgO can all be explained by shifts in mineralogy (Fig. 10a, b and c). The Fe-rich samples are relatively depleted in MgO, Al_2O_3 and SiO_2, their abundances increase as the Fe-content decreases. This indicates that SiO_2-, MgO- and Al_2O_3-poor samples have a mineralogy without abundant Fe-silicates as these are the minerals that incorporate Mg, Al and Si. This is confirmed when the mineralogy (Table 5) is compared with the chemical composition (Table 6). It reveals that samples with abundant Fe-oxides and carbonates have the highest Fe contents and that as the abundance of stilpnomelane and biotite increases, the SiO_2, MgO and Al_2O_3 contents increase at the cost of Fe_2O_3 (Fig. 10a, b and c). Sample MP53 deviates from this trend in the Fe_2O_3-Al_2O_3 and Fe_2O_3-MgO plots because it only contains one Fe-silicate mineral above the XRD detection limit, clinochlore, which differs from the stilpnomelane and biotite found in the other samples. Similarly, ARP S2 does not fit the trend in the Fe_2O_3-MgO plot because it contains abundant K-feldspar which does not incorporate Fe or Mg in its structure. Trends observed in Fe_2O_3-K_2O and Al_2O_3-K_2O plots further strengthen this argument (Fig. 10d and e). The positive trends for Al_2O_3-K_2O are also observed for MgO-K_2O. This, combined with the negative trend for Fe_2O_3-K_2O, indicates the formation of K-bearing Fe-silicates. Since the two most abundant minerals, stilpnomelane and biotite, are K-bearing Fe-silicates these correlations were an expected result. In these plots, MP53 does not fit the trends since it has no major K-bearing minerals. Positive Fe_2O_3-P_2O_5 and negative SiO_2-P_2O_5 correlations can be explained by preferential adsorption of phosphorus on magnetite over Fe-silicate surfaces (Daou et al., 2007).

The XRD results did not show major fractions of Na-bearing silicates, however the correlations for SiO_2-Na_2O, Fe_2O_3-Na_2O and MgO-Na_2O indicate that a Na-bearing silicate is likely present (Fig. 10f, g and h). Within the Fe-silicate group samples, there are positive trends for SiO_2-Na_2O and MgO-Na_2O while a negative correlation is found for Fe_2O_3-Na_2O. This indicates that the Na_2O contents increase as the fraction of Fe-silicates increases. This could suggest the formation of Na-bearing Fe-Mg-

silicates. It is unlikely that these are Al-bearing silicates since there is no correlation between Al_2O_3 and Na_2O ($R^2 = 0.066$). Since the petrography of the samples was not considered in this study, it is impossible to determine the type of Na-silicate with certainty, but based on previous work on the Griquatown and Kuruman BIFs the most likely candidate is Riebeckite (e.g. Beukes and Klein, 1990; Webb et al., 2003; Klein, 2005).

The presence of pyrite and Fe-carbonates can be traced by comparing the major element abundances with TC and TS. The negative correlation for SiO_2-TS and positive correlation for Fe_2O_3-TS are directly related to the relative abundance of pyrite (Fig. 14a and b). The relative abundance of pyrite decreases as the Fe-silicate content increases, which correlates well with the observation that pyrite is more common in samples with abundant Fe-carbonate and -oxide minerals. The presence of carbonates can be traced by looking at CaO-TIC and SiO_2-CaO plots (Fig. 14c and d). MnO-TC, TIC and TOC also show positive correlations, but since CaO and MnO display similar behaviour they are treated as one in the CaO plots. The observed trend in the CaO-TIC plot indicates that the carbon content increases as the CaO content increases which is expected as the carbonate ion (CO_3^{2-}), which is what the TIC mainly represents, is required to form these minerals. Since Ca is one of the constituents of ankerite, this is an expected trend. The negative trends on the SiO_2-TC and SiO_2-CaO plots shows that, as the amount of SiO_2 increases, the amount of Fe-carbonates, and therefore the TIC, decreases. This is supported by the trends observed in the $\frac{Fe}{Fe+Si}$-SiO_2 plot which clearly shows a shift from Fe-carbonates to Fe-silicates with increasing SiO_2 contents (Fig. 10a).

Overprinting of the Primary Signatures

The REY patterns for LREE depleted samples nearly all show no or positive Eu anomalies as well as strongly positive Y anomalies, corresponding with previous studies (e.g. Beukes and Klein, 1990; Bolhar et al., 2005; Cabral et al., 2013). On the other hand, the LREE enriched samples show larger variability as both positive and negative La and Eu anomalies and positive Y anomalies are observed. These lutites have a REY composition that is different from the surrounding BIF, implying either different origin or significant mixing with another component. LREE enriched samples have been reported previously in the Griquatown and Kuruman BIFs albeit rarely (Beukes and Klein, 1990; Pickard, 2003). Since the average stilpnomelane lutite composition is LREE depleted ($(Sm/Yb)_{SN}$ = 0.35; Beukes and Klein, 1990), the LREE enrichment is mostly attributed to a felsic volcanic addition (Pickard, 2003). The absence of a profound negative Ce-anomaly implies that the oceans were still reducing with respect to Ce at the time of deposition. This is supported by the behaviour of MnO as there is a positive correlation between MnO and CaO, implying Mn concentrates in the Fe-carbonates over Fe-silicates. Since Mn substitutes for Ca or Fe(II) in the Fe-carbonates, it has to be present in its reduced Mn(II) state. The presence of the reduced Mn(II) implies that the system is reducing with respect Mn, which has a similar oxidation potential to Ce, and therefore also with respect to Ce (Bekker et al., 2014).

Post-depositional alteration can result in secondary signatures overprinting the primary ones. Easily soluble elements are most susceptible to being remobilized. An element commonly used to trace this in reducing systems is Eu (Bolhar et al., 2004). In near-anoxic and reducing systems, such as the Archean ocean, significant amounts of Eu(II) can be remobilized at temperatures exceeding 200°C (Bau and Dulski, 1996). However, since the metamorphic conditions in the West Transvaal basin were late diagenetic to low-grade metamorphic with temperatures below 170°C and pressures not exceeding 2 kbar (Beukes and Klein, 1990), it is not likely that Eu was remobilized in significant amounts. Another mechanism for Eu remobilization is dissolution as a result of diagenetic reduction (MacRae et al., 1992). However, this is unlikely to have occurred within BIFs since this would also remobilize Fe(II) and therefore affect the rhythmic nature of the Si- and Fe-bands in the BIFs (Bau and Dulski, 1996). Since Eu(II) remobilization in the Griquatown BIF can be ruled out, there is no indication that post-depositional alteration changed primary signatures.

The $(Pr/Yb)_{SN}$ is dominated by the variability in LREE rather than HREE (Fig. 13). Moreover, there is a correlation between the LREE enrichment and the Zr abundance (Fig. 16). The strong correlation (R^2=0.74) implies that there is an additional input of material which, for most samples, causes the large variability in LREE abundances (Bolhar et al., 2004). The LREE dependence of the $(Pr/Yb)_{SN}$ ratio implies that addition of this material has profound effects on LREE and minimal effect on the HREE abundances. Two samples do not fit well within this trend, MP53 and HEX S3. Since MP53 was deposited in the Hotazel formation, it was deposited under different conditions. On the other hand, Sample HEX S3 is found in the Kuruman BIF and still displays an anomalously high $(Pr/Yb)_{SN}$ ratio related to LREE enrichment, $(Pr/Dy)_{SN}$ = 5.41. This could be related to the stratigraphic positioning of the sample as it is located in the upper regions of the Kuruman IF, adjacent to a volcanic interval (Fig. 5). Therefore it might have leached REE from this volcanic unit which would explain low Zr abundance in relation to the LREE enrichment as Zr is highly immobile compared to the REE. However, since the chemical composition of this volcanic deposit is unknown, this hypothesis cannot be tested at present.

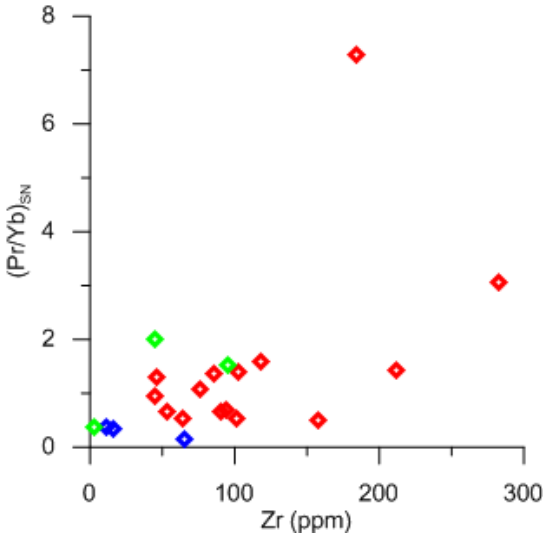

Figure 16: The variability of the LREE enrichment compared to the Zr-abundance. Anomalously LREE enriched samples is HEX S3

The Eu-anomaly decreases as the Zr abundance increases, implying that the Eu-anomaly also controlled by the additional input of material (Fig. 17). Samples with low Zr abundances are the only ones to show the positive Eu-anomaly that is commonly found in BIFs, associated with the hydrothermal input. Only four Fe-silicate group samples show positive Eu-anomalies, while all of the Fe-carbonate and other-group samples from the Griquatown and Kuruman IFs display positive Eu anomalies. Since minor amounts of are capable of altering the primary marine signatures, the shale normalized negative Eu anomalies can be explained by mixing of the marine component with an external input (Bolhar et al., 2004). Based on the magnitude of the negative Eu-anomalies this input must have had a felsic composition (Pecoits et al., 2009). The exception to the trend is sample GAS S6, which has the highest Zr abundance and yet contains no Eu-anomaly (Eu/Eu* = 0.98). An alternative explanation for varying Eu-anomalies is that they are related to changes in hydrothermal input with time (Bau and Dulski, 1996). Temperature variations in hydrothermal systems are capable of generating variable Eu-anomalies. However, if this were the case I would not expect the Eu anomaly to depend on the Zr abundance.

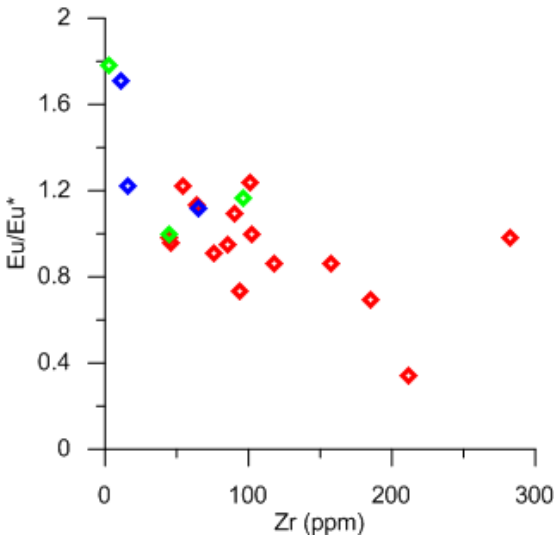

Figure 17: The variability of the Eu-anomaly plotted against the Zr abundance. Sample GAS S6 has the highest Zr contents yet no Eu-anomaly.

A plot of Zr/Cr against Cr/Th shows an inverse relationship (Fig. 18). The presence of high Zr/Cr and low Cr/Th values confirms that the input is felsic in composition (Condie and Wronkiewicz, 1990). Reports of zircons with a felsic volcanogenic origin in the Kuruman and Griquatown BIFs further strengthen the argument that felsic volcanics have had an influence on the deposition of the BIFs

(Pickard, 2003). This additional component may have originated from either the weathering, transport and deposition of terrestrial material or the settling of volcanic ash. Based purely on these trace element ratios it is impossible to distinguish between these sources, since in both cases the material would have a felsic composition. The majority of the late Archean continental crust, as much as 90%, consists of a felsic tonalite-trondhjemite-granodiorite composition (TTG suite; Martin et al., 2005) while the composition of the volcanics is also thought to be primarily felsic (Beukes and Klein, 1990; Pickard, 2003; Beukes and Gutzmer, 2008).

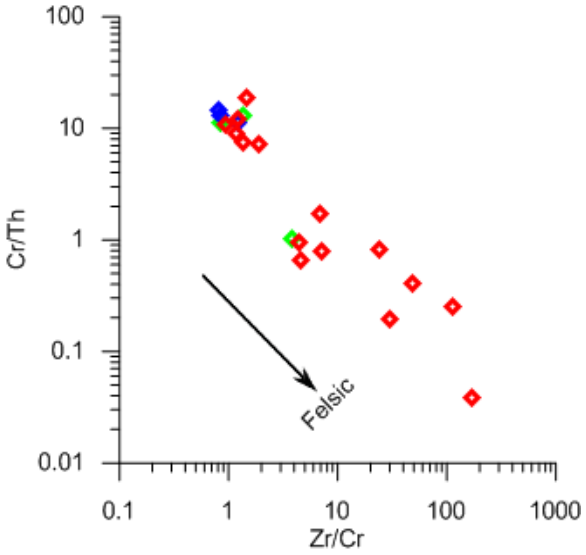

Figure 18: Zr/Cr vs. Cr/Th plot to determine the composition of the mixing component following Condie and Wronkiewicz (1990).

The weathering of continental material would be paired with the transport of heavy trace mineral phases which are resistant to weathering, some only under reducing conditions, such as uraninite (UO_2), molybdenite (MoS_2), chromite ($FeCr_2O_4$), rutile (TiO_2) and zircon ($ZrSiO_4$; Rasmussen and Buick, 1999). The presence of a detrital component would therefore result in increased concentrations of the elements constituting these minerals. But when the degree of felsic input is plotted against the abundances of these trace elements different trends are observed (Fig. 19). The degree of input is represented by Cr/Th as it represents the influence of the felsic component. A lower Cr/Th indicates a stronger felsic component while the ratio will increase as Cr/Th ratios decrease (Condie and Wronkiewicz, 1990). We can see that, as the felsic component becomes larger, the abundances of Ti, V, Cr and Mo decrease while U and Zr abundances increase. The decoupled behaviour for the transition metals and U is therefore a strong indicator that we are not looking at a detrital component. Instead it is likely that these trends are generated by a fractionation process which can be explained in two ways. First of all, it can be the result of fractionation in a magmatic system where the incompatible elements (U and Zr) are enriched compared to the more compatible elements (Ti, V, Cr and Mo) as a result of crystal fractionation in the source magma during the generation of felsic melts. Fractionation may also have taken place in the water column. However, due to the different adsorption behaviour of the elements onto Fe-oxyhydroxides this is unlikely. The transition metals and U are capable of adsorbing to particle surfaces while Zr is not (White and Peterson, 1996; Arnold et al., 1998; O'Loughlin et al., 2003). Since U and the transition metals readily adsorb to the Fe-oxyhydroxides surfaces, similar trends would be expected. However, since U abundances increase and transition metal abundances decrease with increasing felsic input, this implies their behaviour is decoupled and therefore not likely related to adsorption of trace metals to Fe-oxyhydroxide particles.

There is a strong heterogeneity in trace element abundances and REY anomalies within the stratigraphy. This could indicate compositional variability in the source of the felsic material, implying a magmatic source. However, the depth-dependent variability does not rule out a detrital component, because linear relations are observed between Zr and Eu/Eu* and $(Pr/Yb)_{SN}$, implying that the hydrothermal component mixed with a material of which the composition was constant through time. Since the TTG suites are compositionally homogeneous (Martin et al., 2005; Pankhurst et al., 2011), differences in sediment supply through time could explain the variability. The detrital material would subsequently be transported into the basin via turbidites, explaining the cyclicity (Krapez et al., 2003). The vast lateral extent of the lutites can also be explained via both turbiditic and volcanic events. However, if these deposits were the result of turbidites I would expect to see abundant soft-sediment deformation, intercalations of clasts and irregular layering (Simonson, 1985; Krapez et al., 2003). Such features were not observed, indicating that a volcanogenic source of this

material is a more plausible explanation. The absence of sedimentary features such as cross-bedding and oolitic textures in the Griquatown BIF is an indicator that the deposition took place below the storm-wave base (Beukes and Klein, 1990). The presence of K-feldspar in sample ARP S2 is another argument for the deposition of the lutites as volcanic ash beds, because K-feldspar is not formed under the metamorphic conditions that were present in the BIFs (Miyano and Beukes, 1984; Klein, 2005). Furthermore, petrographic studies of stilpnomelane lutite beds from the Kuruman IF have shown that, in those lutites, the K-feldspar is present as cuspate mineral shards (Beukes, 1984). The presence of cuspate shards implies that this is the result of volcanic ash deposits, because if a detrital component was responsible I would not expect to find K-feldspar since it is prone to weathering and would therefore be broken down to clay minerals (Teng et al., 2001).

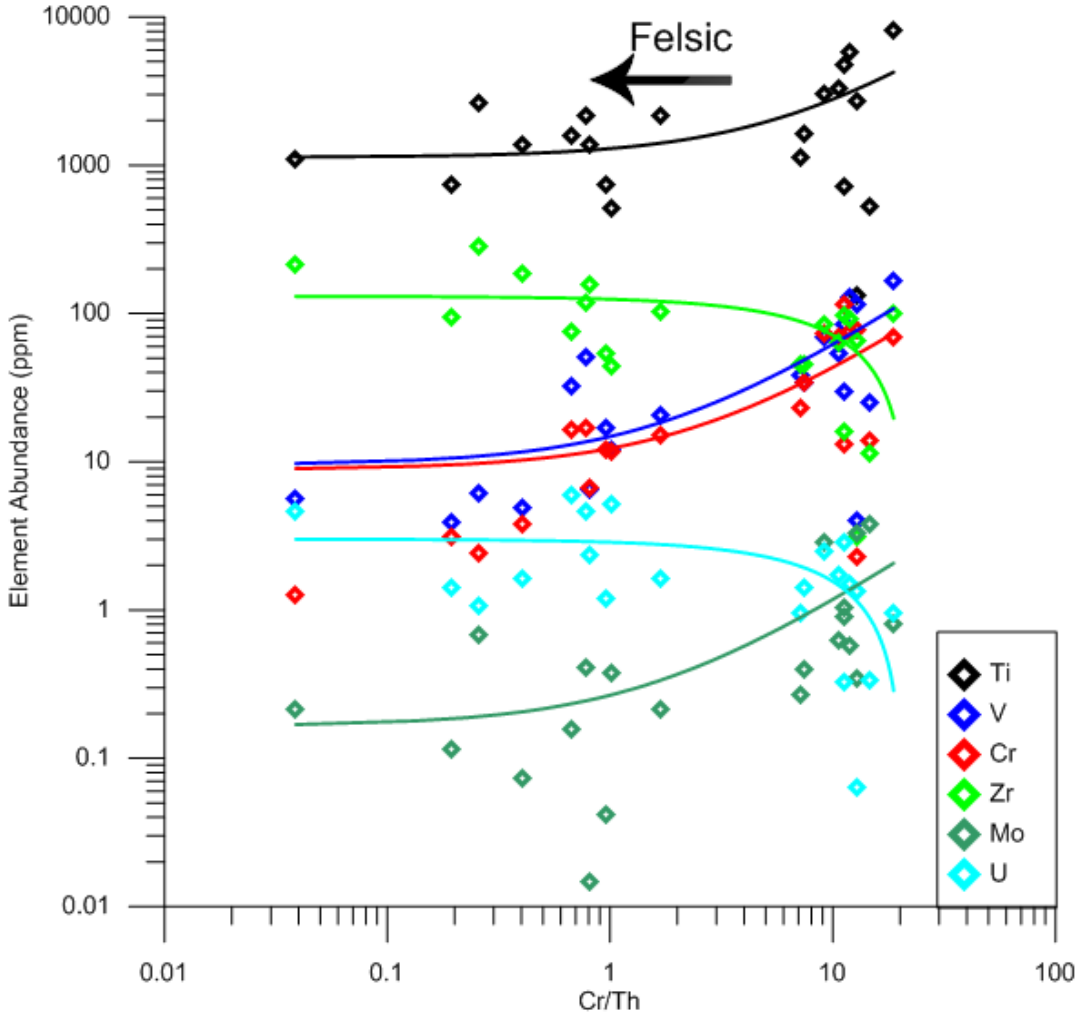

Figure 19: Plot displaying trends in trace element abundance compared to the degree of felsic input.

Since the Australian Hamersley and South African Transvaal basins were connected at the time of deposition, it is possible to compare the REY abundances in the Griquatown BIF with those in the contemporaneously deposited BIF in the Hamersley basin. Radiometric dating showed that the time-equivalents of the Griquatown BIF in the Hamersley basin are the Woongara rhyolite and the Boolgeeda BIF (Martin et al., 2000; Kampmann et al., 2015). This is supported by the study of Beukes and Gutzmer (2008) who argue that stilpnomelane lutites in the lower part of the Griquatown BIF are directly related to the Woongarra rhyolite. Furthermore, at the top of the Boolgeeda BIF glacial diamictites are reported, similar to those found in the Griquatown BIF (Swanner et al., 2013). The introduction of a felsic component related to the emplacement of the Woongarra rhyolite fits my hypothesis regarding the genesis of the stilpnomelane lutites. While it is impossible to directly link the Woongarra rhyolite due a lack of available REY data (Pankhurst et al., 2011), the

contemporaneous deposition makes it a prime target of future investigation regarding the source of the felsic volcanic input. The REE patterns from the Boolgeeda BIF show various similarities with those found in the Griquatown BIF such as the absence of La anomalies, variable Eu anomalies (0.44 ≤ Eu/Eu* ≤ 1.89), positive Y anomalies and variable REE slopes due to LREE variability (Kato and Kimura, 1999; Kato et al., 2006). As in the Griquatown BIF, variability in Eu anomalies is attributed to felsic volcanic input (Kato et al., 2006). There are also some differences with the Griquatown REY patterns. First of all, there is no clear LREE enrichment in Boolgeeda BIF samples. This may be, in part, due to the fact that we are looking at REE abundances from different BIF lithologies while only lutites are taken into account for the Griquatown BIF. Since the lutites are affected by felsic volcanic input they will contain more LREE than the surrounding BIF. Moreover, the Boolgeeda BIF displays a weak but consistent negative Ce anomaly (0.72 ≤ Ce/Ce* ≤ 1.00; Kato et al., 2006) while there are no Ce anomalies observed within the lutites of the Griquatown BIF.

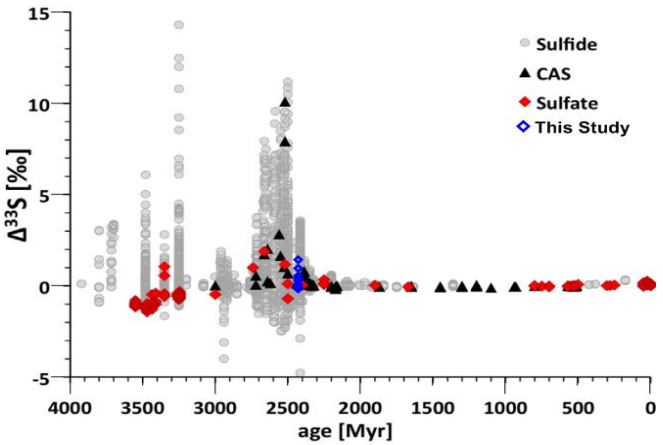

Figure 20: Temporal evolution of sulphur MIF. My data fits well with previous data. Edited from Claire et al. (2014).

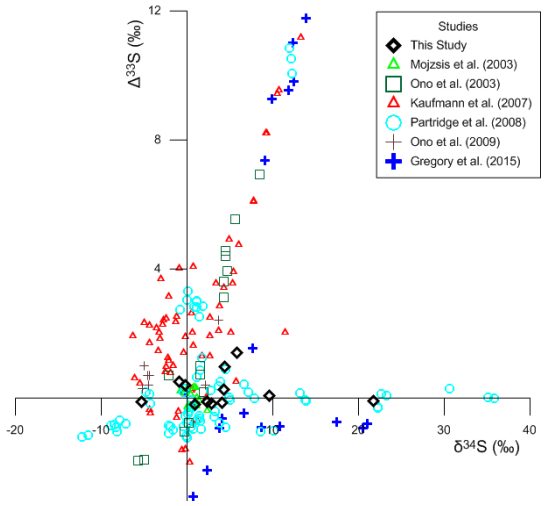

Figure 21: Comparison with previous studies in near-contemporaneous IFs from the 2.5 Ga Mt. McRae shale and 2.46-2.48 Brockman IF (Hamersley basin) and the 2.44-2.48 Kuruman IF (Griqualand West basin; ages from Gregory et al., 2015; Kampmann et al., 2015).

<u>Sulphur MIF: Implications for Atmospheric Composition</u>

During the late Mesoarchean and most of the Neoarchean, there is a spike in the variability of the $\Delta^{33}S$ values to values between -4 to +12‰ which is attributed to the initiation of oxygenic photosynthesis (Izon et al., 2015). This is followed by a global decrease in the range of $\Delta^{33}S$ values from -4 to +12‰ to slightly negative or positive values up to +2‰ which has been dated at 2.46-2.47 Ga (Bekker et al., 2004; Reuschel et al., 2013; Fig. 20). The decreased $\Delta^{33}S$ variability is observed during the later stages of the Neoarchean and early Paleoproterozoic and is associated with the onset of the GOE (Reuschel et al., 2013). My $\Delta^{33}S$ values vary from slightly negative (-0.20‰) to positive (1.40‰), corresponding well with the contemporaneously deposited sediments, in both the Hamersley and Griqualand basins, as well as the age of the Griquatown IF which was dated 2431±31 Ma near the base (Fig. 21; Domagal-Goldman et al., 2008; Kampmann et al., 2015). The MIF signal disappears at 2317±7 Ma, indicating that enough oxygen had accumulated in the atmosphere to cease the MIF of sulphur (Reuschel et al., 2013). The presence of sulphur MIF throughout the entire Griquatown BIF implies that the atmospheric oxygen concentrations were less than 10^{-5} PAL at the time of deposition (Pavlov and Kasting, 2002). It also confirms that the entire BIF was deposited prior to the disappearance of the MIF signal as a result of O_2 accumulation in the atmosphere around 2.32 Ga (Bekker et al., 2004).

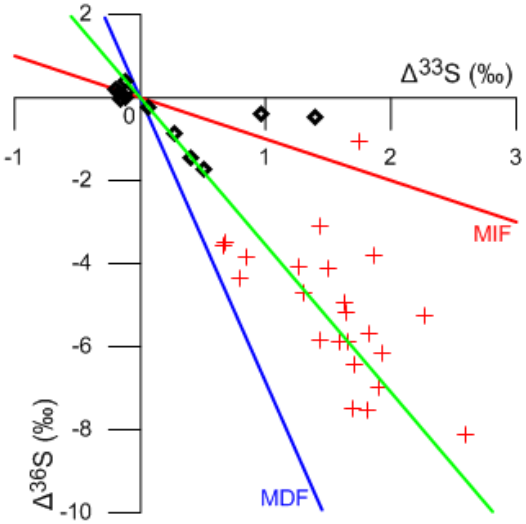

Figure 22: $\Delta^{36}S$-$\Delta^{33}S$ isotope plot displaying the fit of my data (black diamonds) with that of Wacey et al. (2015; Red crosses). The green line represents the fit from Wacey et al. (2015) $\Delta^{36}S/\Delta^{33}S = -3.6$.

The majority of samples in the $\Delta^{33}S$-$\Delta^{36}S$ plots cluster around the volcanic SO_2 composition, but there are some samples which show large variations in the slope of $\Delta^{33}S$-$\Delta^{36}S$. Some of the data shows a $\Delta^{36}S$ depletion, plotting on a line with a slope of $\Delta^{36}S/\Delta^{33}S \approx -3.3$ compared to the ARA (Fig. 15b; Fig. 22). Previous studies have reported a $\Delta^{36}S$ depletion in Neoarchean samples, but these samples plot on a line with a slope $\Delta^{36}S/\Delta^{33}S = -1.5$ (Zerkle et al., 2012; Izon et al., 2015). Numerical models have shown that steeper slopes may arise as a result of changes in atmospheric chemistry, in particular varying methane (CH_4) levels. The CH_4 abundances would increase due to methanogenesis and create an organic haze in the atmosphere, generating a steeper slope up to $\Delta^{36}S/\Delta^{33}S = -1.5$ (Zerkle et al., 2012). However, this is insufficiently steep to explain the $\Delta^{36}S/\Delta^{33}S = -3.3$ that is observed in my results. Heavily depleted $\Delta^{36}S$ isotopic compositions are very scarce and, in the Archean, have only been observed in Paleoarchean pyrites from the 3480 Ma Dresser Formation, $\Delta^{36}S/\Delta^{33}S = -3.6$ (Fig. 22**;** Wacey et al., 2015). A study regarding the 1963 Agung volcanic eruption also revealed a $\Delta^{36}S$ depleted signature, $\Delta^{36}S/\Delta^{33}S = -3.3$ (Baroni et al., 2007). Two possible mechanisms were posed to explain the generation of the $\Delta^{36}S$ depletion in the Archean where either (1) differences in atmospheric chemistry or (2) a second reduced sulphur pool with a different isotopic composition affect the $\Delta^{36}S$-$\Delta^{33}S$ slope (Wacey et al., 2015). However, these hypotheses remain untested and therefore no conclusion can be drawn based on these studies. While field studies have not yet been able to provide an explanation, experimental and theoretical studies regarding sulphur MIF have reported mechanisms capable of generating the observed $\Delta^{36}S/\Delta^{33}S$ trends. Firstly, Johnston et al. (2007) reported shifts in $\Delta^{36}S$ up to ±2‰ as a result of microbial sulphate reduction. These were, however, accompanied by large shifts in $\delta^{34}S$ which are not observed here as the samples with $\Delta^{36}S$ depletion display minimal $\delta^{34}S$ variability (Fig. 15c). Another possible explanation is that the definition of the ARA in the $\Delta^{36}S$-$\Delta^{33}S$ plots is flawed as it is based on SO_2-photolysis over a limited wavelength range, while sulphur MIF is a wavelength dependent process (Farquhar et al., 2007; Lyons, 2009). Lyons (2009) argues that, when multiple wavelengths are taken into account, the MIF reference array can generate slopes of $-1 \leq \Delta^{36}S/\Delta^{33}S \leq -3$ due to photolytic reactions occurring for S_3, excited-state SO_2 and SO on top of regular SO_2. In this case, my data would fit at the steeper end of the slopes predicted by Lyons (2009). However, variability in the slope of the ARA is accompanied by large shifts, up to 100‰, in $\delta^{34}S$ ratios which are not observed. The $\delta^{34}S$ signatures could be muted and/or overridden by subsequent microbial sulphate reduction, however this cannot be tested and validated (Wacey et al., 2015). There are also some $\Delta^{36}S$ enriched samples plot on a line above the ARA with a slope $\Delta^{36}S/\Delta^{33}S \approx -0.5$ (Fig. 22). Pyrites displaying $\Delta^{36}S$ enrichment, $\Delta^{36}S/\Delta^{33}S \approx -0.6$ have been reported in Neoarchean (Izon et al., 2015). They pose that slopes shallower than the ARA may represent an unknown state of atmospheric chemistry. The large amount of uncertainty regarding the variability of the $\Delta^{36}S/\Delta^{33}S$ cannot be explained currently, because the effects of thermal- and photo-chemical effects on the MIF signals in the Archean atmosphere are not fully understood (Oduro et al., 2014). Even though we do not currently comprehend how atmospheric variability affects the MIF signal, the observed slope of $\Delta^{36}S/\Delta^{33}S \approx -3.3$ is highly anomalous for the Neoarchean and does not compare well with other data from Neoarchean rocks which generally plot on the ARA (Kaufmann et al., 2007).

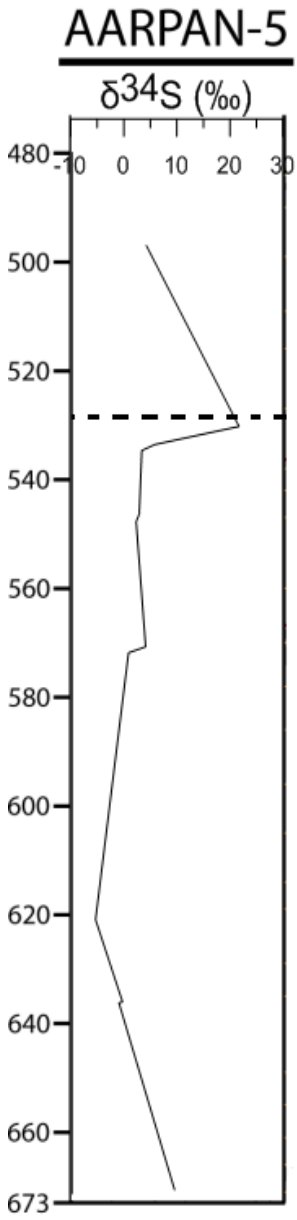

Figure 23: Depth dependent variability of sulphur MDF. Samples depths were extrapolated to core AARPAN-5. The dashed black line indicates the top of the upper thick shale band.

Sulphur MDF: Microbial Sulphate Reducers

The $\Delta^{33}S$-$\delta^{34}S$ and $\Delta^{36}S$-$\delta^{34}S$ plots show that most samples plot around the ARA, an indicator for atmospheric MIF generation, implying that deposition of the Griquatown and Kuruman IFs occurred during the onset of the GOE, prior to the disappearance of the sulphur MIF signal (Fig. 15a and c). Most Neoarchean samples display positive $\Delta^{33}S$ and negative $\Delta^{36}S$ values, implying that the sulphur was originally sourced from the reduced sulphur (S^0) pool (Izon et al., 2015). However, half of my samples show slightly negative $\Delta^{33}S$ as well as positive $\Delta^{36}S$ values, indicating that the sulphide in the pyrite was introduced to the seawater via the sulphate (SO_4^{2-}) pool (Farquhar et al., 2001; Johnston et al., 2006). The presence of a sulphate signature in some of the samples implies that sulphur was sourced from both pools. Izon et al. (2015) reported similar variability in sulphate source pools, but since their dataset is significantly larger they were able to constrain that only a minor fraction of the samples had sulphur sourced from the sulphate pool. In my samples there is an equal division between the sulphur pools, but this may arise as a result of a limited dataset. In order to generate the magnitude of sulphur MDF that is observed via microbial sulphate reduction (MSR) the Archean oceans must have had SO_4^{2-} concentrations of at least 200 µM (Habicht et al., 2002). This value lies at the uppermost boundary inferred for Archean ocean sulphate levels which are estimated between 1 and 200 µM (e.g. Jamieson et al., 2013; Crowe et al., 2014; Zhelezinskaia et al., 2014). Since the required SO_4^{2-} concentrations are inferred to be at the upper limit, other explanation may be required to explain the high magnitude of sulphur MDF. The first possibility is that the fractionation did not occur through biotic processes at all, instead it occurred through thermochemical reduction of sulphate (Ohmoto and Goldhaber, 1997; Canfield, 2001). However, temperatures in the Archean hydrothermal vents and oceans were insufficient to cause sulphate reduction via either magmatic hydrolysis or reduction on Fe-mineral surfaces (Bekker et al., 2014). Moreover, the TOC of the samples indicates the presence of microbes. While this does not mean that these are sulphate reducing microbes, there is a positive correlation between TS and TOC which suggests that at least part of the microbial community consisted of sulphate reducers. Secondly, it could be that the high magnitude in sulphur MDF is generated through a Rayleigh fractionation effect where a temporal evolution of the sulphate isotopic composition causes gradual shifts as a result of progressive consumption of isotopically light sulphur by microbes, generating more positive sulphur MDF

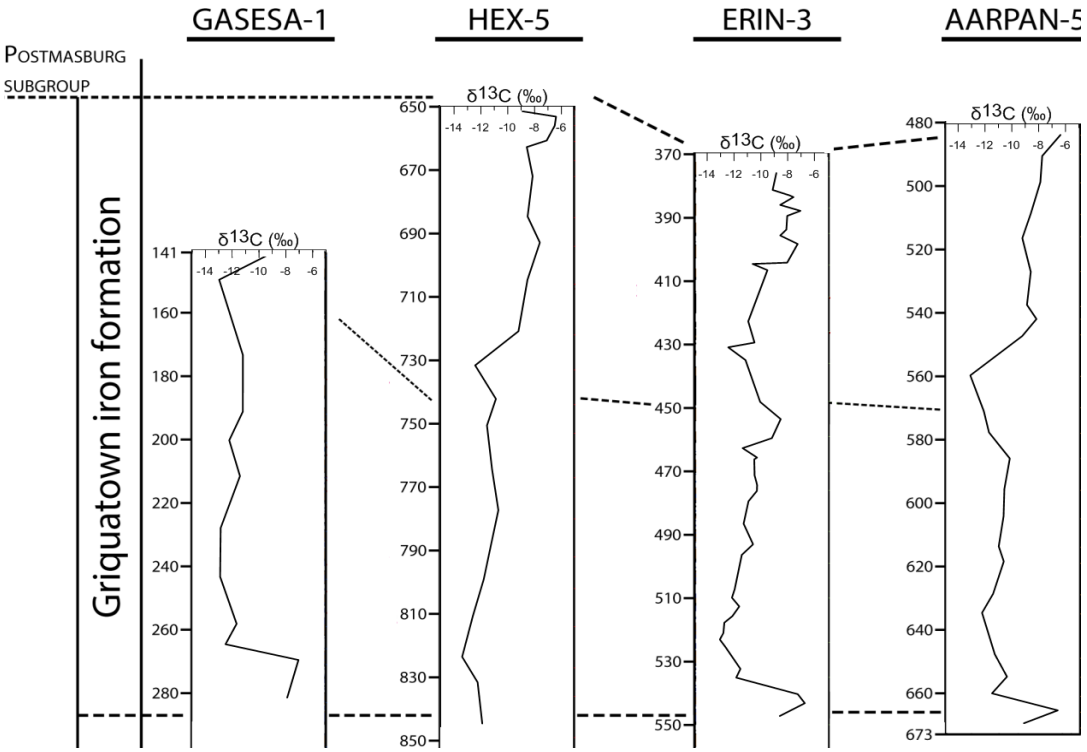

Figure 24: The evolution of carbon isotope fractionation, the $\delta^{13}C$ variability through time shows a gradual increase within the Griquatown formation. Values for $\delta^{13}C$ courtesy of P.B.H. Oonk (personal comm.).

through time. The third, and final, possibility is that it could be related to limited periods of enhanced sulphate concentrations in the basin. Since the deposition of stilpnomelane lutites is directly related to volcanic activity it is also expected that, at the time of deposition, atmospheric SO_2 concentrations are elevated due to the volcanic emissions. This will result in a short-term increase of sulphate in the basin which is sufficient to generate high magnitude sulphur MDF. Moreover, this volcanic activity will introduce more microbial nutrients to the surface layers of the seawater, enhancing microbial primary productivity. This explains the correlation between the TOC and TS as well as the overall increased carbon content compared to the BIFs as this does not require changes in the preservation rate of the organic carbon compounds. A second notable observation is that the $\delta^{34}S$ shows a depth dependence within the cores, the most negative values are found in the lower part of the Griquatown BIF and a steady increase is observed towards the upper shale bands. Similar observations have been made for the near-contemporaneously deposited Mt. McRae shale and Brockman IF in the Hamersley basin, Australia (Ono et al., 2003; Partridge et al., 2008). The gradual increase of $\delta^{34}S$ is thought to be a Rayleigh fractionation effect in a basin with no or limited exchange with the open ocean where SO_4^{2-} was no limiting factor as SO_4^{2-} concentrations are required to be around 200 µM to generate large $\delta^{34}S$ variability (Habicht et al., 2002; Partridge et al., 2008). In this basin MSR was taking place, reducing the SO_4^{2-} with the slightly negative $\Delta^{33}S$ to sulphide which was subsequently incorporated in pyrite. Throughout the sulphate reduction and pyrite formation, the negative $\Delta^{33}S$ is retained as it is unaffected by these processes (Wacey et al., 2015). MSR can also explain the depth-dependent shift in $\delta^{34}S$, because $^{32}SO_4^{2-}$ is preferred over $^{34}SO_4^{2-}$ since it requires less energy to break down the bonds during metabolism. As a result, negative $\delta^{34}S$ values will be generated first and as time progresses, the ^{32}S is consumed and $\delta^{34}S$ increases to more positive values. The highly positive $\delta^{34}S$ samples can be explained as those close to the end of the Rayleigh fractionation cycle. This process has also been observed on a smaller scale by Gregory et al. (2015) observed a gradual increase of $\delta^{34}S$ within a single pyrite nodule measuring from the centre outwards and attributed it to Rayleigh fractionation. In order to support the hypothesis that the gradual increase in $\delta^{34}S$ is related to a Rayleigh fractionation process, sulphur isotope data from drill cores which represent the edge of the basin will have to be integrated with this data set, since we do require isotopically heavy $\delta^{34}S$ to be preserved in the basin as well. One way to do this, is via lateral variability in the isotopic composition of the deposited sulphides. This could be related to the proximity to the edge of the basin and therefore water depth. Strongly negative sulphur isotopic values have been reported in the contemporaneously deposited Boolgeeda BIF, located in the Australian Hamersley Basin, where $\delta^{34}S$ values range between -40 and +10‰ (Swanner et al., 2013). Since these basins were connected at the time of deposition, this could indicate lateral variability in the isotopic composition of the sulphur. Variability in carbon isotopes ($\delta^{13}C$) also shows a gradual increase with decreasing age, supporting the idea of a Rayleigh fractionation process controlling mass dependent isotope fractionation in the Transvaal basin at the time of deposition of the Griquatown iron formation (Fig. 24). While the Rayleigh fractionation effect seems to disappear from the sulphur isotopes after the deposition of the upper of the three thick shale bands, the gradual increase in $\delta^{13}C$ persists until the top of the core. The apparent disappearance of the Rayleigh fractionation trend in $\delta^{34}S$ might be a result of either a lack of data points above the topmost thick shale bed, since there is only one, or due to an anomalously high $\delta^{34}S$ value for sample HEX S1.

Depositional Environment of Stilpnomelane Lutites

By compiling all the different pieces of evidence I am now able to reconstruct a depositional environment for the stilpnomelane lutites in the Griquatown BIF (Fig. 25). The absence of Ce-anomalies implies that deposition occurred in a marine environment which was reducing with respect to Ce. The presence of sulphur MIF shows that the atmospheric oxygen levels were still $<10^{-5}$ PAL (Pavlov and Kasting, 2002). The low oxidation potential of both ocean and atmosphere imply the presence of a ferruginous ocean. Sulphur MDF, in combination with TOC, indicates that there was a microbial presence during the deposition of the lutites. Since slightly negative $\Delta^{33}S$ and positive $\Delta^{36}S$ are commonly observed, the sulphur is sourced from the sulphate pool. Therefore sulphate reducers

are likely among the microbes. These would reduce the S(VI) to S(-II) and explain the variability in $\delta^{34}S$ (Shen and Buick, 2004). The gradual increase of $\delta^{34}S$ values with decreasing age in the upper part of the Griquatown BIF is indicative of a Rayleigh fractionation process, implying deposition occurred in a basin with no or limited exchange with the open ocean. The absence of sedimentary structures implies that the Griquatown BIF was deposited in quiet waters, below the storm wave base, as a result of the oxidation of hydrothermally supplied Fe(II), the source of which is beyond the scope of this study (Simonson, 1985; Pickard, 2003). The stilpnomelane lutites represent episodic events as indicated by their notable cyclicity (Beukes and Gutzmer, 2008). Their deposition is related to periodic introduction of additional component to the system. Based on the trace element behaviour the most likely source of this material is felsic volcanic ash from distal volcanism. There is no evidence for the presence of a large detrital component. Beukes and Klein (1990) interpreted this such that the depositional environment was completely devoid of terrestrial material.

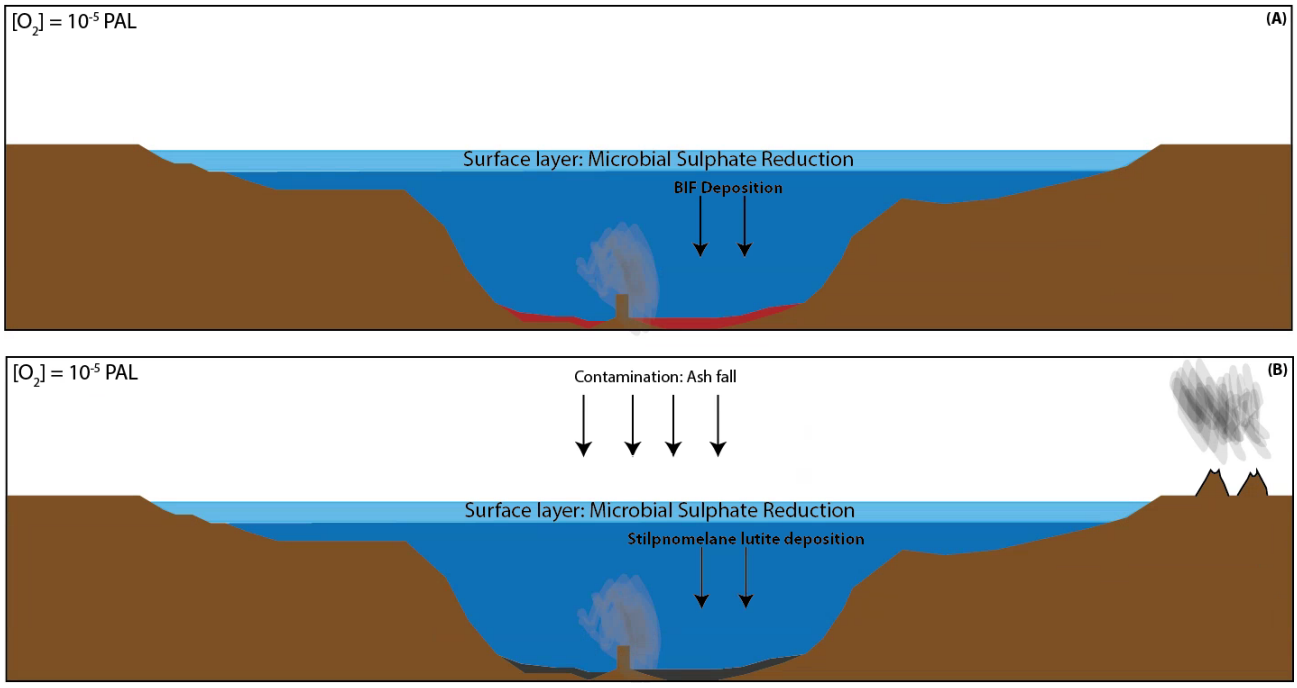

Figure 25: Depositional model for stilpnomelane lutites in a closed basin. **(25a):** Deposition of the Griquatown BIF resulting from the oxidation of hydrothermally supplied Fe(II). **(25b):** Deposition of the stilpnomelane lutites as a result of felsic ash mixing in with hydrothermally sourced material.

VIII: Conclusions

Major- and trace element XRF and ICP-MS measurements, mineralogical XRD measurements, (in)organic carbon and quadruple sulphur isotope analyses of the 2.43 Ga Griquatown BIF have revealed the depositional mechanisms of the stilpnomelane lutites. They contain three omnipresent minerals, stilpnomelane, magnetite and pyrite. Siderite, ankerite, biotite, quartz and clinochlore are present in some, but not all, samples while K-feldspar, calcite and talc have been identified in one sample each. Based on the mineralogy samples were divided in three groups; an Fe-silicate group, Fe-carbonate group and 'other' group. Samples from the Fe-carbonate and 'other' group generally show lower amounts of felsic input and contain more primary REY signatures (LREE depletion and positive Eu anomalies) than the Fe-silicate group samples which show a large variability. This variability is controlled by variations in LREE additions, which are correlated to the degree of felsic input.

In the environment, sulphur MIF shows that the Griquatown BIF was deposited during the onset of the GOE, prior to the disappearance of the sulphur MIF signal in its entirety, constraining the age of the upper Griquatown IF to be older than 2.32 Ga. Variability in slopes for $\Delta^{33}S$-$\Delta^{36}S$ plots implies short term variability in atmospheric chemistry at the time of deposition. However, the

understanding of Archean atmospheric states is insufficiently advanced to explain this in more detail. The absence of Ce-anomalies shows that the oxidation state of the oceans reducing with respect to Ce and therefore incapable of readily oxidizing Fe and Mn. Post-depositional conditions were late diagenetic to low-grade metamorphic conditions and thus insufficient to alter the primary signatures. Therefore it is safe to assume that there was no post-depositional alteration of the REY signatures. The deposition of stilpnomelane lutites took place in a basin with no or limited exchange with the open ocean during the deposition of the Griquatown BIF, as indicated by the gradual increase of $\delta^{34}S$ and $\delta^{13}C$ with decreasing age. These trends indicate that Rayleigh fractionation governed the isotopic composition of sulphur and carbon. Deposition of the lutites took place below the storm wave base depth, as no sedimentary structures have been observed. During quiet periods, the Griquatown BIF would be deposited, but episodic felsic input to the system would alter the primary hydrothermal signal. Based on the behaviour of various trace elements that constitute weathering resistant heavy minerals I was able to constrain the source as volcanic ash. Distal felsic volcanic activity would produce ash which settled, generating large variability in trace element abundances, LREE variability and Eu-anomalies. Correlations along a single line for the mixing of the marine and felsic component implies the felsic component originates from one source. This implies that the system was devoid of a weathered continental component. Large variations in $\delta^{34}S$ indicate that the presence of microbes also influenced the deposition of the lutites which is further supported by intervals with high TOC. The slightly negative $\Delta^{33}S$ and positive $\Delta^{36}S$ indicate that these microbes were, at least partially, sulphate reducers.

IX: Acknowledgements

The author would like to thank everyone that has been involved in making this thesis into what it has become. Special thanks go out to Paul Mason, Paul Oonk and Harilaos Tsikos for their tireless efforts and help during this study as well as for reviewing the manuscript. Their comments have provided invaluable assistance in finalising this thesis. Furthermore, I would like to thank Helen de Waard for her tireless efforts of helping me with everything in the GML and for performing the total destructions in preparation for ICP-OES and ICP-MS analysis. Rob van Galen and Jan van Tongeren are thanked for their help during all of the sulphur and carbon measurements. I would like to thank Anita van Leeuwen-Tolboom for performing the XRD analysis as well as her help during the interpretation of the data. XRF results could not have been obtained without the help from Bernadette Marchand and Jan van Tongeren, for which they are thanked. Discussions regarding sulphur isotope extractions procedures benefited greatly from the input by Peter Kraal who also helped in the process of trying to get the extraction set-up working in Utrecht, albeit to no avail. All of the people at the Westfalische Wilhelms Universitat Münster, in particular Harald Strauss, Artur Fugmann, Andreas Lutter and Vanessa Fichtner, are thanked for their help and guidance during my stay in Münster for the S-extraction experiments and the subsequent quadruple sulphur isotope analysis.

X: References

Alexander, B.W., Bau, M., Andersson, P., Dulski, P. (2008). Continentally-derived solutes in shallow Archean seawater: Rare earth element and Nd isotope evidence in iron formation from the 2.9 Ga Pongola Supergroup, South Africa. Geochimica et Cosmochimica Acta, vol. 72, p. 378-394

Alibert, C., McCulloch, M.T. (1993). Rare-earth element and neodymium isotopic compositions of the banded iron-formations and associated shales from Hamersley, western Australia. Geochimica et Cosmochimica Acta, vol. 57, p. 187-204

Alibo, D.S., Nozaki, Y. (1999). Rare earth elements in seawater: Particle association, shale-normalization and Ce oxidation. Geochimica et Cosmochimica Acta, vol. 63, p. 363-372

Anbar, A.D., Holland, H.D. (1992). The photochemistry of manganese and the origin of banded iron formations. Geochimica et Cosmochimica Acta, vol. 56, p. 2595-2603

Anbar, A.D., Duan, Y., Lyons, T.W., Arnold, G.L., Kendall, B., Creaser, R.A., Kaufman, A.J., Gordon, G.W., Scott, C., Garvin, J., Buick, R. (2007). A Whiff of oxygen before the great oxidation event? Science, vol. 317, p. 1903-1906

Arnold, T., Zorn, T., Bernhard, G., Nitsche, H. (1998). Sorption of uranium(VI) onto phyllite. Chemical Geology, vol. 151, p. 129-141

Balci, N., Shanks III, W.C., Mayer, B., Mandernack, K.W. (2007). Oxygen and sulfur isotope systematics of sulfate produced by bacterial and abiotic oxidation of pyrite. Geochimica et Cosmochimica Acta, vol. 71, p. 3796-3811.

Baroni, M., Thiemens, M.H., Delmas, R.J., Savarino, J. (2007) Mass-independent Sulfur Isotopic Compositions in Stratospheric Volcanic Eruptions. Science, vol. 315, p. 84-87

Bau, M. (1996). Controls on the fractionation of isovalent trace elements in magmatic and aqueous systems: evidence from Y/Ho, Zr/Hf and lanthanide tetrad effect. Contributions to Mineralogy and Petrology, vol. 123, p. 323-333

Bau, M., Dulski, P. (1996). Distribution of yttrium and rare-earth elements in the Penge and Kuruman iron-formations, Transvaal Supergroup, South Africa. Precambrian Research, vol. 79, p. 37-55

Bau, M., Moller, P., Dulski, P. (1997). Yttrium and lanthanides in eastern Mediterranean seawater and their fractionation during redox cycling. Marine Chemistry, vol. 56, p. 123-131

Bau, M., Dulski, P. (1999). Comparing yttrium and rare earths in hydrothermal fluids from the Mid-Atlantic Ridge: Implications for Y and REE behaviour during near-vent mixing and for the Y/Ho of Proterozoic seawater. Chemical Geology, vol. 155, p. 77-90

Bau, M., Romer, R.L., Luders, V., Beukes, N.J. (1999). Pb, O and C isotopes in silicified Mooidraai dolomite (Transvaal Supergroup, South Africa): Implications for the composition of Paleotproterozoic seawater and 'dating' the increase of oxygen in the Precambrian atmosphere. Earth and Planetary Science Letters, vol. 174, p. 43-57

Bekker, A., Holland, H.D., Wang, P.-L., Rumble III, D., Stein, H.J., Hannah, J.L., Coetzee, L.L., Beukes, N.J. (2004). Dating the rise of atmospheric oxygen. Nature, vol. 427, p. 117-120

Bekker, A., Slack, J.F., Planavsky, N., Krapez, B., Hofmann, A., Konhauser, K.O., Rouxel, O.J. (2010). Iron formation: the sedimentary product of a complex interplay among mantle, tectonic, oceanic and biospheric processes. Economic Geology, vol. 105, p. 467-508

Bekker, A., Planavsky, N.J., Krapez, B., Rasmussen, B., Hofmann, A., Slack, J.F., Rouxel, O.J., Konhauser, K.O. Iron Formations: Their origins and implications for ancient seawater chemistry, in: Treatise on Geochemistry vol. 9, Amsterdam, Elsevier, 2014

Beukes, N.J. (1984). Sedimentology of the Kuruman and Griquatown iron-formations, Transvaal Supergroup, Griqualand west, South Africa. Precambrian Research, vol. 24, p. 47-84

Beukes, N.J., Klein, C. (1990). Geochemistry and sedimentology of a facies transition - from microbanded to granular iron formation - in the early Proterozoic Transvaal Supergroup, South Africa. Precambrian Research, vol. 47, p. 99-139

Beukes, N.J., Gutzmer, J. (2008). Origin and Paleoenvironmental significance of major iron formations at the Archean-Paleoproterozoic boundary. Society of Economic Geologists Reviews, vol. 15, p. 5-47

Birdwell, J.E. (2012). Review of rare earth element concentrations in oil shales of the Eocene Green River Formation: U.S. Geological Survey Open-File Report 2012-1016, 20 p.

Bolhar, R., Kamber, B.S., Moorbath, S., Fedo, C.M., Whitehouse, M.J. (2004). Characterisation of early Archaean chemical sediments by trace element signatures. Earth and Planetary Science Letters, vol. 222, p. 43-60

Bolhar, R., Van Kranendonk, M.J., Kamber, B.S. (2005). A trace element study of siderite-jasper banded iron formation in the 3.45 Ga Warrawoona Group, Pilbara Craton - Formation from hydrothermal fluids and shallow seawater. Precambrian Research, vol. 137, p. 93-114

Brocks, J.J. (2011). Millimeter-scale concentration gradients of hydrocarbons in Archean shales: Live-oil escape or fingerprint of contamination? Geochimica et Cosmochimica Acta, vol. 75, p. 3196-3213

Cabral, A.R., Creaser, R.A., Nagler, T., Lehmann, B., Voegelin, A.R., Belyatsky, B., Pasava, J., Seabra Gomes Jr, A.A., Galbiatti, H., Bottcher, M.E., Escher, P. (2013). Trace-element and multi-isotope geochemistry of Late-Archean black shales in the Carajas iron-ore district, Brazil. Chemical Geology, vol. 362, p. 91-104

Canfield, D.E., Raiswell, R., Westrich, J.T., Reaves, C.M., Berner, R.A. (1986). The use of chromium reduction in the analysis of reduced inorganic sulfur in sediments and shales. Chemical Geology, vol. 54, p. 149-155

Canfield, D.E., Thamdrup, B. (1994). The production of 34S-depleted sulfide during bacterial disproportionation of elemental sulfur. Science, vol. 266, p. 1973-1975

Canfield., D.E. (1998). A New model for Proterozoic ocean chemistry. Nature, vol. 396, p. 450-453

Canfield, D.E. (2001). Biogeochemistry of Sulfur Isotopes. Reviews in Mineralogy and Geochemistry, vol. 43, p. 607-636

Claire, M.W., Kasting, J.F., Domagal-Goldman, S.D., Stueken, E.E., Buick, R., Meadows, V.S. (2014). Modeling the signature of sulfur mass-independent fractionation produced in the Archean atmosphere. Geochimica et Cosmochimica Acta, vol. 141, p. 365-380

Condie, K.C., Wronkiewicz, D.J. (1990). The Cr/Th ratio in Precambrian pelites from the Kaapvaal Craton as an index of craton evolution. Earth and Planetary Science Letters, vol. 97, p. 256-267

Crowe, S.A., Dossing, L.N., Beukes, N.J., Bau, M.J., Kruger, S.J., Frei, R., Canfield, D.E. (2013). Atmospheric oxygenation three billion years ago. Nature, vol. 501, p. 536-538

Crowe, S.A., Paris, G., Katsev, S., Jones, C.A., Kim, S.T., Zerkle, A.L., Nomosatryo, S., Fowle, D.A., Adkins, J.F., Sessions, A.L., Farquhar, J., Canfield, D.E. (2014). Sulfate was a trace constituent of Archean seawater. Science, vol. 346, p. 735-739

Daou, T.J., Begin-Colin, S., Greneche, J.M., Thomas, F., Derory, A., Bernhardt, P., Legare, P., Pourroy, G. (2007). Phosphate Adsorption Properties of Magnetite-Based Nanoparticles. Chemistry of Materials, vol. 19, p. 4494-4505

Date, A.R., Cheung, Y.Y., Stuart, M.E. (1987). The influence of polyatomic ion interferences in analysis by inductively coupled plasma source mass spectrometry (ICP-MS). Spectrochimica Acta Part B: Atomic Spectroscopy, vol. 42, p. 3-20

De Baar, H.J.W., Bacon, M.P., Brewer, P.G., Bruland, K.W. (1985). Rare earth elements in the Pacific and Atlantic Oceans. Geochimica et Cosmochimica Acta, vol. 49, p. 1943– 1959.

De Baar, H.J.W., Schijf, J., Byrne, R.H. (1991). Solution chemistry of the rare earth elements in seawater. European Journal of Solid State Inorganic Chemistry, vol. 28, p. 357-373

De Kock, M.O., Evands, D.A.D., Beukes, N.J. (2009). Validating the existence of Vaalbara in the Neoarchean. Precambrian Research, vol. 174, o. 145-154

Ding, T., Valkiers, S., Kipphardt, H., De Bievre, P., Taylor, P.D.P., Gonfiantini, R., Krouse, R. (2001). Calibrated sulfur isotope abundance ratios of the three IAEA sulfur isotope reference materials and V-CDT with a reassessment of the atomic weight of sulfur. Geochimica et Cosmochimica Acta, vol. 65, p. 2433-2437

Domagal-Goldman, S.D., Kasting, J.F., Johnston, D.T., Farquhar, J. (2008). Organic haze, glaciations and multiple sulfur isotopes in the Mid-Archean Era. Earth and Planetary Science Letters, vol. 269, p. 29-40

Farquhar, J., Bao, H., Thiemens, M. (2000). Atmospheric influence of Earth's earliest Sulfur cycle. Science, vol. 289, p. 756-758

Farquhar, J., Savarino, J., Airieau, S., Thiemens, M.H. (2001). Observation of wavelength-sensitive mass-independent sulphur isotope effects during SO_2 photolysis: Implications for the early atmosphere. Journal of Geophysical Research, vol. 106, p. 32829-32839

Farquhar, J., Wing, B.A. (2003). Multiple sulfur isotopes and the evolution of the atmosphere. Earth and Planetary Science Letters, vol. 213, p. 1-13

Farquhar, J., Peters, M., Johnston, D.T., Strauss, H., Masterson, A., Wiechert, U., Kaufmann, A.J. (2007). Isotopic evidence for Mesoarchean anoxia and changing atmospheric sulphur chemistry. Nature, vol. 449, p. 706-709

Farquhar, J., Zerkle, A.L., Bekker, A. (2011). Geological constraints on the origin of oxygenic photosynthesis. Photosynthetic Research, vol. 107, p. 11-36

Feret, F.R., Hamouche, H., Boissonneault, Y. (2003). Spectral Interference in X-ray Fluorescence Analysis of Common Materials. International Centre for Diffraction Data 2003, Advances in X-ray Analysis, vol. 46, p. 381-387

Fischer, W.W., Knoll, A.H. (2009). An iron shuttle for deepwater silica in Late Archean and early Paleoproterozoic iron formation. Geological Society of America Bulletin, vol. 121, p. 222-235

Francois, L.M. (1986). Extensive deposition of banded iron formations was possible without photosynthesis. Nature, vol. 320, p. 352-354

Gregory, D.D., Large, R.R., Halpin, J.A., Steadman, J.A., Hickman, A.H., Ireland, T.R., Holden, P. (2013). The chemical conditions of the late Archean Hamersley basin inferred from whole rock and pyrite geochemistry with $\Delta^{33}S$ and $\delta^{34}S$ isotope analyses. Geochimica et Cosmochimica Acta, vol. 149, p. 223-250.

Groger, J., Franke, J., Hamer, K., Schulz, H.D. (2009). Quantitative Recovery of Elemental Sulfur and Improved Selectivity in a Chromium-Reducible Sulfur Distillation. Geostandards and Geoanalytical Research, vol. 33, p. 17-27

Gromet, L.P., Dymek, R.F., Haskin, L.A., Korotev, R.L. (1984). The "North American shale composite": Its compilation, major and trace element characteristics. Geochimica et Cosmochimica Acta, vol 48, p. 2469-2482

Gross, C.T., McIntyre, S.M., Houk, R.S. (2009). Reduction of Matrix Effects in Inductively Coupled Plasma Mass Spectrometry by Flow Injection with an Unshielded Torch. Analytical Chemistry, vol. 81, p. 4898-4905

Gumsley, A.P., Chamberlain, K., Bleeker, W., Soderlund, U., de Kock, M.O., Kampmann, T.C., Larsson, E. (2015). U-Pb TIMS and in-situ SIMS dating of baddleyite and zircon from sub-volcanic sills of the Ongeluk Formation (Transvaal Supergroup) in the Griqualand West sub-basin, Kaapvaal Craton, with implications for Snowball Earth and the Great Oxygenation Event. Paper presented at AGU-GAC-MAC-CGU Joint Assembly 2015, Montréal, Canada.

Habicht, K.S., Gade, M., Thamdrup, B., Berg, P., Canfield, D.E. (2002). Calibration of sulfate levels in the Archean Ocean. Science, vol. 298, p. 2372-2374

Hamade, T., Konhauser, K.O., Raiswell, R., Goldsmith, S., Morris, R.C. (2003). Using Ge/Si ratios to decouple iron and silica fluxes in Precambrian banded iron formations. Geology, vol. 31, p. 35-38

Hassler, S.W., Simonson, B.M., Summer, D.Y., Bodin, L. (2011). Paraburdoo spherule layer (Hamersley Basin, Western Australia): Distal ejecta from a fourth large impact near the Archean-Proterozoic boundary. Geology, vol. 39, p. 307-310

Hickson, C.J., Juras, S.J. (1986). Sample contamination by grinding. Canadian Mineralogist, vol. 24, p. 585-589

Holland, H.D. The Chemical Evolution of the Atmosphere and Oceans. Princeton, New Jersey: Princeton University Press, 1984

Horstmann, U.E., Halbich, I.W. (1995). Chemical composition of banded iron-formations of the Griqualand West Sequence, Northern Cape Province, South Africa, in comparison with other Precambrian iron formations. Precambrian Research, vol. 72, p. 109-145

Huston, D.L., Logan, G.A. (2004). Barite, BIFs and bugs: evidence for evolution of the Earth's early hydrosphere. Earth and Planetary Science Letters, vol. 220, p. 41-55

Isley, A.E., Abbott, D.H. (1999). Plume-related mafic volcanism and the deposition of banded iron formation. Journal of Geophysical Research, vol. 104, p. 15461-15477

Izon, G., Zerkle, A.L., Zhelezinskaia, I., Farquhar, J., Newton, R.J., Poulton, S.W., Eigenbrode, J.L., Claire, M.W. (2015). Multiple oscillations in Neoarchean atmospheric chemistry. Earth and Planetary Science Letters, vol. 431, p. 264-273

Jamieson, J.W., Wing, B.A., Farquhar, J., Hannington, M.D. (2013). Neoarchaean seawater sulphate concentrations from sulphur isotopes in massive sulphide ore. Nature Geoscience, vol. 6, p. 61-64

Johnston, D.T., Poulton, S.W., Fralick, P.W., Wing, B.A., Canfield, D.E., Farquhar, J. (2006). Evolution of the oceanic sulfur cycle at the end of the paleoproterozoic. Geochimica et Cosmochimica Acta, vol. 70, p. 5723-5739

Johnston, D.T., Farquhar, J., Canfield, D.E. (2007). Sulfur isotope insights into microbial sulphate reduction: When microbes meet models. Geochimica et Cosmochimica Acta, vol. 71, p. 3929-3947

Kamber, B.S., Whitehouse, M.J. (2007). Micro-scale sulphur isotope evidence for sulphur cycling in the late Archean shallow ocean. Geobiology, vol. 5, p. 5-17

Kampmann, T.C., Gumsley, A.P., de Kock, M.O., Soderlund, U. (2015). U-Pb geochronology and paleomagnetism of the Westerberg Sill Suite, Kaapvaal Craton - Support for a coherent Kaapvaal-Pilbara Block (Vaalbara) into the Paleoproterozoic? Precambrian Research, vol. 269, p. 58-72

Kato, Y., Kimura, S.-I. (1999). Bulk-rock chemical compositions of the Boolgeeda Iron Formation of the Hamersley Group, Western Australia: Its origin and implication from a very low concentration of minor elements. Shigen-Chishitsu, vol. 49, p. 175-189

Kato, Y., Yamaguchi, K.E., Ohmoto, H. (2006). Rare earth elements in Precambrian banded iron formations: Secular changes of Ce and Eu anomalies and evolution of atmospheric oxygen. Geological Society of America Memoirs, vol. 198, p. 269-289

Kaufman, A.J., Johnston, D.T., Farquhar, J., Masterson, A.L., Lyons, T.W., Bates, S., Anbar, A.D., Arnold, G.L., Garvin, J., Buick, R. (2007). Late Archean biospheric oxygenation and atmospheric evolution. Science, vol. 317, p. 1900-1903

Klein, C. (2005). Precambrian banded iron-formations (BIFs) from around the world: Their age, geologic setting, mineralogy, metamorphism, geochemistry and origin. American Mineralogist, vol. 90, p. 1473-1499

Konhauser, K.O., Hamade, T., Raiswell, R., Morris, R.C., Ferris, F.G., Southam, G., Canfield, D.E. (2002). Could bacteria have formed the Precambrian banded iron formations? Geology, vol. 30, p. 1079-1082

Konhauser, K.O., Amskold, L., Lalonde, S.V., Posth, N.R., Kappler, A., Anbar, A.D. (2007). Decoupling photochemical Fe(II) oxidation from shallow-water BIF deposition. Earth and Planetary Science Letters, vol. 258, p. 87-100

Kopp, R.E., Kirschvink, J.L., Hilburn, I.A., Nash, C.Z. (2005). The Paleoproterozoic snowball Earth: A climate disaster triggered by the evolution of oxygenic photosynthesis. Proceedings of the National Academy of Science, vol. 102, p. 11131-11136

Krapez, B., Barley, M.E., Pickard, A.L. (2003). Hydrothermal and resedimented origins of the precursor sediments to banded iron formations: sedimentological evidence from the Early Palaeoproterozoic Brockman Supersequence of Western Australia. Sedimentology, vol. 50, p. 979-1011

Lyons, J.R. (2009). Atmospherically-derived mass-independent sulfur isotope signatures, and incorporation into sediments. Chemical Geology, vol. 267, p. 164-174

MacRae, N.D., Nesbitt, H.W., Kronberg, B.I. (1992). Development of a positive Eu anomaly during diagenesis. Earth and Planetary Science Letters, vol. 109, p. 585-591

Maliva, R.G., Knoll, A.H., Simonson, B.M. (2005). Secular change in the Precambrian silica cycle: Insights from chert petrology. Geological Society of America Bulletin, vol. 117, p. 835-845

Mapeo, R.B.M., Armstrong, R.A., Kampunzu, A.B., Modisi, M.P., Ramokate, L.V., Modie, B.N.J. (2006). A ca. 200Ma hiatus between the Lower and Upper Transvaal Groups of southern Africa: SHRIMP U-Pb detrital zircon evidence from the Segwagwa Group, Botswana: Implications for Palaeoproterozoic glaciations. Earth and Planetary Science Letters, vol. 244, p. 113-132

Martin, D.McB., Powell, C.McA., George, A.D. (2000). Stratigraphic architecture and evolution of the early Paleoproterozoic McGrath Trough, Western Australia. Precambrian Research, vol. 99, p. 33-64

Martin, H., Smithies, R.H., Rapp, R., Moyen, J.-F., Champion, D. (2005). An overview of adakite, tonalite-trondhjemite-granodiorite (TTG), and sanukitoid: relationships and some implications for crustal evolution. Lithos, vol. 79, p. 1-24

May, T.W., Wiedmeyer, R.H. (1998). A Table of Polyatomic Interferences in ICP-MS. Atomic Spectroscopy, vol. 19, p. 150-155.

Miyano, T., Beukes, N.J. (1984). Phase relations of stilpnomelane, ferri-annite, and riebeckite in very low-grade metamorphosed iron-formations. South African Journal of Geology, vol. 87, p. 111-124

Mojzsis, S.J., Coath, C.D., Greenwood, J.P., McKeegan, K.D., Harrison, T.M. (2003). Mass-independent isotope effects in the Archean (2.5 to 3.8 Ga) sedimentary sulphides determined by iron microprobe analysis. Geochimica et Cosmochimica Acta, vol. 67, p. 1635-1658

Nance, W.B., Taylor, S.R. (1976) Rare earth element patterns and crustal evolution I. Australian post-Archean sedimentary rocks. Geochimica et Cosmochimica Acta, vol. 40, p. 1539-1551

Neubauer, K. (2010). Reducing the Effects of Interferences in Quadrupole ICP-MS. Spectroscopy

Oduro, H., Izon, G., Ono, S. (2014). Mass-dependent and Mass-independent Sulphur Isotope Fractionation Accompanying Thermal- and Photo-chemical Decomposition of Sulphur Bearing Organic Compounds. Geophysical Research Abstracts, vol. 16, EGU2014-14036-1

Ohmoto, H., Goldhaber, M. B. (1997). Sulfur and carbon isotopes. Geochemistry of Hydrothermal ore deposits, vol. 3, p. 517-611

O'Loughlin, E.J., Kelly, S.D., Cook, R.E., Csecsits, R., Kemner, K.M. (2003). Reduction of Uranium(VI) by Mixed Iron(II)/Iron(III) Hydroxide (Green Rust): Formation of UO_2 Nanoparticles. Environmental Science and Technology, vol. 37, p. 721-727

Ono, S., Eigenbrode, J.L., Pavlov, A.A., Kharecha, P., Rumble III, D., Kasting, J.F., Freeman, K.H. (2003). New insights into Archean sulfur cycle from mass-independent sulfur isotope records from the Hamersley Basin, Australia. Earth and Planetary Science Letters, vol. 213, p. 15-30

Ono, S., Kaufman, A.J., Farquhar, J., Sumner, D.Y., Beukes, N.J. (2009). Lithofacies control on multiple-sulfur isotope records and Neoarchean sulfur cycles. Precambrian Research, vol. 169, p. 58-67

Pankhurst, M.J., Schaefer, B.F., Betts, P.G. (2011). Geodynamics of rapid voluminous felsic magmatism through time. Lithos, vol. 123, p. 92-101

Partridge, M.A., Golding, S.D., Baublys, K.A., Young, E. (2008). Pyrite paragenesis and multiple sulfur isotope distribution in late Archean and early Paleoproterozoic Hamersley Basin sediments. Earth and Planetary Science Letters, vol. 272, p. 41-49

Pavlov, A.A., Kasting, J.F. (2002). Mass-Independent Fractionation of Sulfur Isotopes in Archean Sediments: Strong Evidence for an Anoxic Archean Atmosphere. Astrobiology, vol. 2, p. 27-41

Pecoits, E., Gingras, M.K., Barley, M.E., Kappler, A., Posth, N.R., Konhauser, K.O. (2009). Petrography and geochemistry of the Dales Gorge banded iron formation: Paragenetic sequence, source and implications for palaeo-ocean chemistry. Precambrian Research, vol. 172, p. 163-187

Pickard, A.L. (2003). SHRIMP U-Pb zircon ages for the Palaeoproterozoic Kuruman Iron Formation, Northern Cape Province, South Africa: evidence for simultaneous BIF deposition of Kaapvaal and Pilbara Cratons. Precambrian Research, vol. 125, p. 275-315

Pickard, A.L., Barley. M.E., Krapez, B. (2004). Deep-marine depositional setting of banded iron formation: sedimentological evidence from interbedded clastic sedimentary rocks in the early Palaeoproterozoic Dales Gorge Member of Western Australia. Sedimentary Geology, vol. 170, p. 37-62

Planavsky, N., Rouxel, O., Bekker, A., Shapiro, R., Fralick, P., Knudsen, A. (2009). Iron-oxidizing microbial ecosystems thrived in late Paleoproterozoic redox-stratified oceans. Earth and Planetary Science Letters, vol. 286, p. 230-242

Planavsky, N., Bekker, A., Rouxel, O.J., Kamber, B., Hofmann, a., Knudsen, A., Lyons, T.W. (2010). Rare Earth Element and yttrium compositions of Archean and Paleoproterozoic Fe formations revisited: New perspectives on the significance and mechanisms of deposition. Geochimica et Cosmochimica Acta, vol. 74, p. 6387-6405

Planavsky, N.J., McGoldrick, P., Scott, C.T., Li, C., Reinhard, C.T., Kelly, A.E., Chu, X., Bekker, A., Love, G.D., Lyons, T.W. (2011). Widespread iron-rich conditions in the mid-Proterozoic ocean. Nature, vol. 477, p. 448-451

Posth, N.R., Hegler, F., Konhauser, K.O., Kappler, A. (2008). Alternating Si and Fe deposition caused by temperature fluctuations in Precambrian oceans. Nature Geosciences, vol. 1, p. 703-708

Posth, N.R., Konhauser, K.O., Kappler, A. Banded Iron Formations, in: Encyclopedia of Geobiology, Springer Netherlands, 2011.

Posth, N.R., Canfield, D.E., Kappler, A. (2014). Biogenic Fe(III) minerals: From formation to diagenesis and preservation in the rock record. Earth Science Reviews, vol. 135, p. 103-121

Pourmand, A., Dauphas, N., Ireland, T.J. (2012). A novel extraction chromatography and MC-ICP-MS technique for rapid analysis of REE, Sc and Y: Revising CI-chondrite and Post-Archean Australian Shale (PAAS) abundances. Chemical Geology, vol. 291, p. 38-54

Raiswell, R., Reinhard, C.T., Derkowski, A., Owens, J., Bottrell, S.H., Anbar, A.D., Lyons, T.W. (2011). Formation of syngenetic and early diagenetic iron minerals in the late Archean Mt. McRae Shale, Hamersley Basin, Australia: New insights on the patterns, controls and paleoenvironmental implications of authigenic mineral formation. Geochimica et Cosmochimica Acta, vol. 75, p. 1072-1087

Rasmussen, B., Buick, R. (1999). Redox state of the Archean atmosphere: Evidence from detrital heavy minerals in ca. 3250-2750 Ma sandstones from the Pilbara Craton, Australia. Geology, vol. 27, p. 115-118

Reuschel, M., Strauss, H., Lepland, A. (2013). The End of Mass-Independent Fractionation of Sulphur Isotopes, in: Reading the Archive of Earth's Oxygenation Ch. 7.1, Berlin, Springer Berlin Heidelberg, 2013

Scott, C., Lyons, T.W., Bekker, A., Shen, Y., Poulton, S.W., Chu, X., Anbar, A.D. (2011). Tracing the stepwise oxygenation of the Proterozoic ocean. Nature, vol. 452, p. 456-459

Seal II, R.R. (2006). Sulfur isotope geochemistry of Sulfide minerals. Reviews in Mineralogy & Geochemistry, vol. 61, p. 633-677

Shen, Y., Buick, R. (2004). The antiquity of microbial sulfate reduction. Earth-Science Reviews, vol. 64, p. 243-272

Sherrell, R.M., Field, M.P., and Ravizza, G. (1999). Uptake and fractionation of rare earth elements on hydrothermal plume particles at 9°45'N, East Pacific Rise. Geochimica et Cosmochimica Acta, vol. 63, p. 1709−1722.

Simonson, B.M. (1985) Sedimentological constraints on the origins of Precambrian iron-formations. The Geological Society of America Bulletin, vol. 96, p. 244-252

Slack, J.F., Cannon, W.F. (2009). Extraterrestrial demise of banded iron formations 1.85 billion years ago. Geology, vol. 37, p. 1011-1014

Stern, R.J., Avigad, D., Miller, N.R., Beyth, M. (2006). Evidence for the Snowball Earth hypothesis in the Arabian-Nubian Shield and the East African Orogen. Journal of African Earth Sciences, vol. 44, p. 1-20

Swanner, E.D., Bekker, A., Pecoits, E., Konhauser, K.O., Cates, N.L., Mojzsis, S.J. (2013). Geochemistry of pyrite from diamictites of the Boolgeeda Iron Formation, Western Australia with implications for the GOE and Paleoproterozoic ice ages. Chemical Geology, vol. 362, p. 131-142

Tan, S.H., Horlick, G. (1987). Matrix-effect Observations in Inductively Coupled Plasma Mass Spectrometry. Journal of Analytical Atomic Spectrometry, vol. 2, p. 745-763

Teng, H.H., Fenter, P., Cheng, L., Sturchio, N.C. (2001). Resolving orthoclase dissolution processes with atomic force microscopy and X-ray reflectivity. Geochimica et Cosmochimica Acta, vol. 65, p. 3459-3474

Wacey, D., Noffke, N., Cliff, J., Barley, M.E., Farquhar, J. (2015). Micro-scale quadruple sulfur isotope analysis of pyrite from the ~3480 Ma Dresser Formation: New insights into sulfur cycling on the early Earth. Precambrian Research, vol. 258, p. 24-35

Webb, A.D., Dickens, G.R., Oliver, N.H.S. (2003). From banded iron-formation to iron ore: geochemical and mineralogical constraints from across the Hamersley Province, Western Australia. Chemical Geology, vol. 197, p. 215-251

White, A.F., Peterson, M.L. (1996). Reduction of aqueous transition metal species on the surfaces of Fe(II)-containing oxides. Geochimica et Cosmochimica Acta, vol. 60, p. 3799-3814

Wolf, R.E. (2005). What is ICP-MS? ... And more importantly, what can it do? http://crustal.usgs.gov/laboratories/icpms/intro.html

Wronkiewicz, D.J., Condie, K.C. (1987). Geochemistry of Archean shales from the Witwatersrand Supergroup, South Africa: Source-area weathering and provenance. Geochimica et Cosmochimica Acta, vol. 51, p. 2401-2416

Zerkle, A.L., Claire, M.W., Domagal-Goldman, S.D., Farquhar, J., Poulton, S.W. (2012). A bistable organic-rich atmosphere on the Neoarchaean Earth. Nature Geoscience, vol. 5, p. 359-363

Zhelezinskaia, I., Kaufman, A.J., Farquhar, J., Cliff, J. (2014). Large sulfur isotope fractionations associated with Neoarchean microbial sulfate reduction. Science, vol. 346, p. 742-744

XI: Appendix A: Detailed Sample Descriptions

Sample **GAS S1**

This sample is a dark-coloured, fine-grained, mudstone of which the surface has visibly weathered. Ubiquitous white material is present on the surface of the sample, as well as some red patches (Fig. A1a). There are also two visible calcitic veins running through the sample. The white minerals, most likely weathered sulphides, persisted further into the sample as the polishing shows that they remain, but are now a grey colour (Fig. A1b). This is supported by the presence of pyrite found in the XRD results.

Figure A1: Pictures of sample GAS S1
A1a. Top left. View from the inside of the sample before polishing.
A1b. Top right. View from the inside of the sample after polishing.
A1c. Bottom left. View from the outside of the sample after polishing.
A1d. Bottom right. Sample powder after grinding

Sample **GAS S2**

This sample is a dark-coloured, fine-grained, mudstone. The sample contains visible reflective mineral grains on the flat surfaces. The sample has a homogeneously dark, unweathered, appearance with no indications of veining (Fig. A2a and A2b).

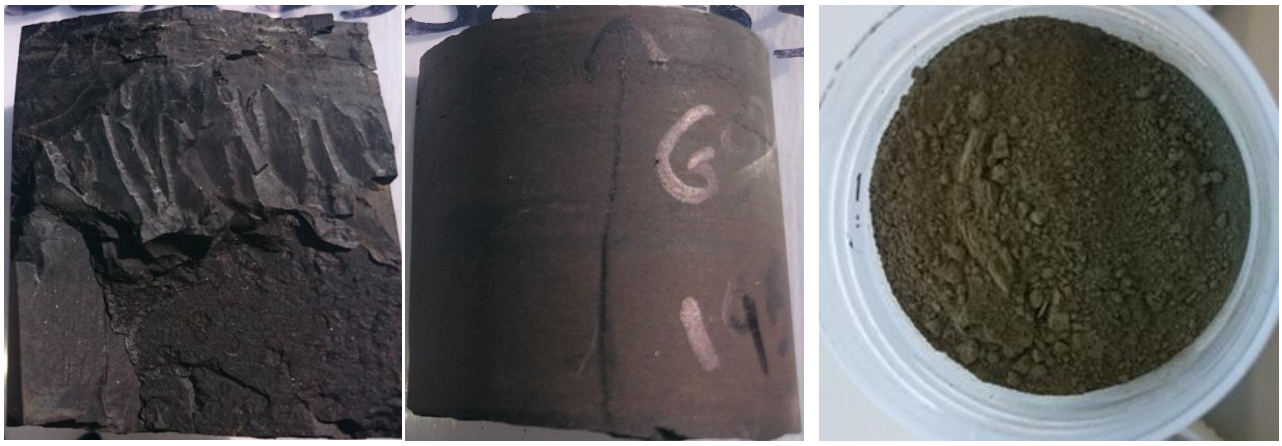

Figure A2: Pictures of sample GAS S2
A2a. Inside view of the sample before polishing.
A2b. View of the sample from the outside before polishing.
A2c. Sample powder after grinding

Sample **GAS S3**

The sample is a dark-coloured, fine-grained, thinly-bedded mudstone. The top of the sample shows some dark-red/brown spots which represent weathering of Fe-rich minerals such as magnetite and/or biotite (Fig. A3a). There are no veins present in the sample. The thin bedding that is observed can be partially attributed to the presence of biotite as inferred by XRD.

Figure A3: Pictures of sample GAS S3
A3a. Top view of sample before polishing.
A3b. Sample powder after grinding.

Sample **GAS S4**

The sample is a dark-coloured, fine-grained, mudstone. When looking at the sample, the first things that stand out are large beige and orange spots (Fig. A4a). The mineral that is responsible for these spots is unknown. After polishing these spots become white, indicative of carbonate minerals (Fig. A4c). On the inside of the sample similar white specks can be seen (Fig. A4b). The orange colour is a remnant of the iron in the minerals weathering and altering the colour as a result. Based on XRD the white minerals are most likely ankerite.

Figure A4: Pictures of sample GAS S4
A4a. Top left. View on the outside of the sample prior to polishing.
A4b. Top right. View on the inside of the sample prior to polishing.
A4c. Bottom left. Same view as Figure 4a,now after polishing.
A4d. Bottom right. Sample powder after grinding.

Sample **GAS S5**

The sample is a dark-coloured, thinly-bedded, fine-grained, mudstone that has been moderately weathered (Fig. A5a). On one of the surfaces we can see individual crystals that are confined to a very thin surface layer. The bottom of the sample does not display weathering to such an extent (Fig. A5b). The brown colour results from iron oxidation. The platy, rusty appearance is a likely result of biotite being the dominant mineral in this sample.

Figure A5: Pictures of sample GAS S5
A5a. Top view of the sample before polishing.
A5b. Bottom view of the sample before polishing.
A5c. Sample powder after grinding

Sample **GAS S6**

The sample is a dark-coloured, fine-grained, thinly-bedded mudstone. There are some white specks visible which are also visible in other samples (Fig. A6a). These are minerals that are present within the black shales which appear to be confined to layers. Based on the XRD the two likely candidates are biotite and pyrite, but due to their microscopic size I was unable to constrain which mineral it was with certainty.

Figure A6: Pictures of sample GAS S6
A6a. Top view of the sample before polishing.
A6b. Bottom view of the sample.
A6c. Sample powder after grinding.

Sample **GAS S7**

This sample is a dark-coloured, fine-grained, thinly-bedded mudstone. The top and bottom surfaces contain lighter coloured layers, which could be indicative of either weathering or mineralogical variations in the sample. Since the inside and outside of the core do not appear to have been weathered significantly it is likely a mineralogical feature (Fig. A7a and A7b).

Figure A7: Pictures of sample GAS S7
A7a. The inside of the sample prior to polishing.
A7b. The outside of the sample prior to polishing.
A7c. Sample powder after grinding.

Sample GAS S8

This sample is a dark-coloured, fine-grained, thinly-bedded mudstone (Fig. A8b). There are some minor signs of weathering. However, the majority of the sample is a homogeneous black colour. The bedding is likely the result of biotite being the most common mineral in the sample.

Figure 8: Pictures of sample GAS S8
A8a. Top view of the sample before polishing.
A8b. Bottom view of the sample before polishing.
A8c. Sample powder after grinding.

Sample **GAS S9**

The sample is a dark-coloured, fine-grained, mudstone with inter-bedded layers of pyrite. In one of the samples the pyrite beds are very nicely horizontally bedded (Fig. A9a, top piece). However, in the lower part of the sample the layers vary laterally in thickness and the pyrite has spread out into the other layers (Fig. A9a, bottom piece). The blue lines can be identified on the outer surface of the sample to correspond with the presence of a vein (Fig. A9b). Based on the mineralogy of the sample, it consists either of siderite or quartz. The green bed thickness variations on the inside can also be seen on the outside of the sample. There are no clear fractures/veins that are cross-cutting the bedding. Upon polishing the thickness variations in the bedding become better visible on the outside as the removal of the surface weathering more clearly exposes the veins and lighter layers (Fig. A9d). Furthermore, upon polishing, the top of both pieces of the sample displays more white specks which can be explained by polishing off a top dark layer and slowly penetrating down into a pyritic one (Fig. A9c).

Figure A9: Pictures of sample GAS S9

A9a. Top left. Inside view of the sample before polishing. We can see clearly that the two samples contain light and dark layers. The top piece has nice thinly-bedded layers while the bottom piece has large layer thickness variations.

A9b. Middle top. Outside view of sample before polishing. Correlation of the layer thicknesses observed on the outside can be done with regards to the presence of veins or more light coloured material.

A9c.Bottom left. Top view of the samples after polishing.

A9d. Middle bottom. Two pictures, outside view from different angles after polishing. We can see that the white vein related to the blue lines in 9a and 9b has become more apparent.

A9e. Central right. Sample powder after grinding.

Sample **GAS S10**

The sample is a dark-coloured, fine-grained, thinly-bedded mudstone. Signs of weathering are especially visible on the top of the sample where a greyish-green layer containing pink specks has formed (Fig. A10a). The inside of the sample is fresh and shows no clear signs of weathering (Fig. A10c). Fig A10b shows some orange coloured specks which are remnants of weathering.

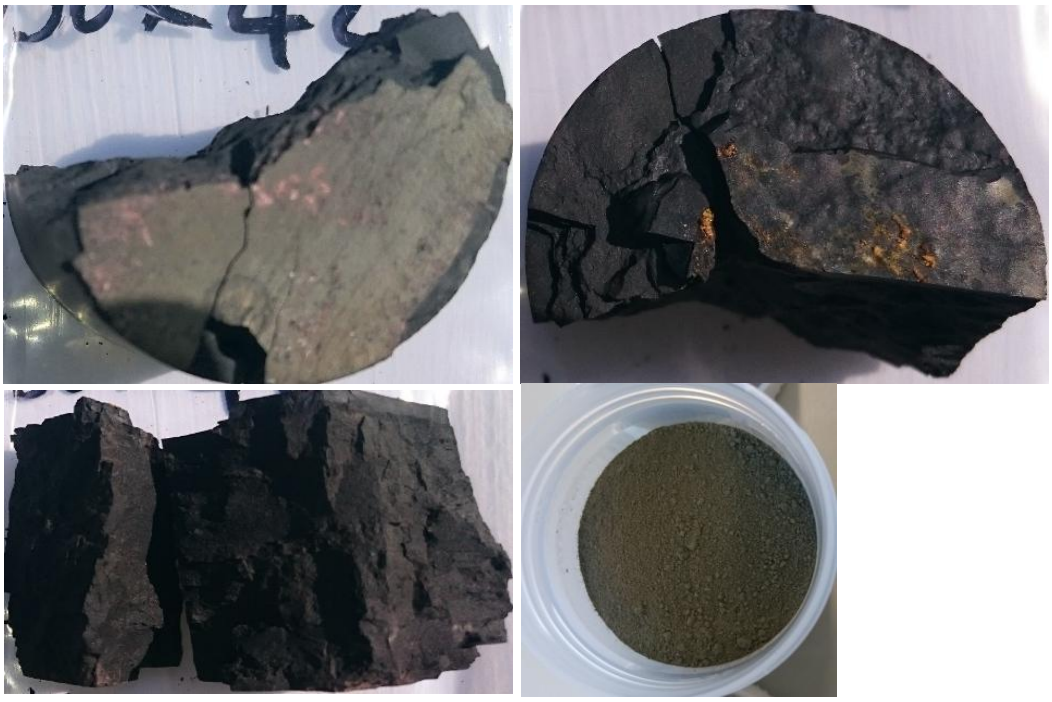

Figure A10: Pictures of sample GAS S10
A10a. Top left. Top view of the sample before polishing.
A10b.Top right. Bottom view of the sample before polishing.
A10c. Bottom left. Inside view of the sample before polishing.
A10d. Bottom right. Sample powder after grinding.

Sample **GAS S11**

This sample consists of three different pieces. Two of those fit together, while the other doesn't. All of the samples are dark-coloured, fine-grained, thinly-bedded mudstones. The pieces that fit together (fig A11a, bottom pieces) contain a vein that is almost the same colour as the surrounding material. In the upper piece the bedding is not horizontal. We can clearly see that the bedding is disturbed and has a kink in it which, based on the layer orientation, could represent a micro-scale fault (Fig. A11c). The dominant presence of biotite in this sample correlates well with the thinly-bedded structure that is observed.

Figure A11: Pictures of sample GAS S11
A11a. Top left. Inside view of the sample pieces before polishing.
A11b. Top middle. Top/Bottom view of the samples before polishing.
A11c. Top right. Sample powder after grinding.
A11d. Bottom. This piece, top piece on A11a, contains a clear bedding. However, upon closer examination the bedding is clearly distorted. The red lines indicate the orientation of the bedding in the sample. This is not observed in the other pieces.

Sample **GAS S12**

This sample is a dark-coloured, fine-grained, mudstone with variable bedding. The bottom of the sample contains a calcitic vein that was removed during sample preparation. The inner surface of the sample displays pinkish coloured mineral which are pyrites in various stages of weathering with colours from gold to the more pinkish depending on the degree of weathering (Fig. A12b). Prior to polishing the sample displays orange spots (Fig. A12a). After polishing these orange spots have become white (Fig. A12c). Furthermore, there is a large amount of heterogeneity observed on the outside where many different minerals are visible which are not horizontally bedded (Fig. A12c). The minerals that have been identified for this part are ankerite, siderite, quartz, magnetite, stilpnomelane and pyrite. The ankerite corresponds with the minerals that were visible as orange minerals before polishing, similar to sample GAS S4. Since no microscopic study was conducted, the other minerals could not be linked to specific grains.

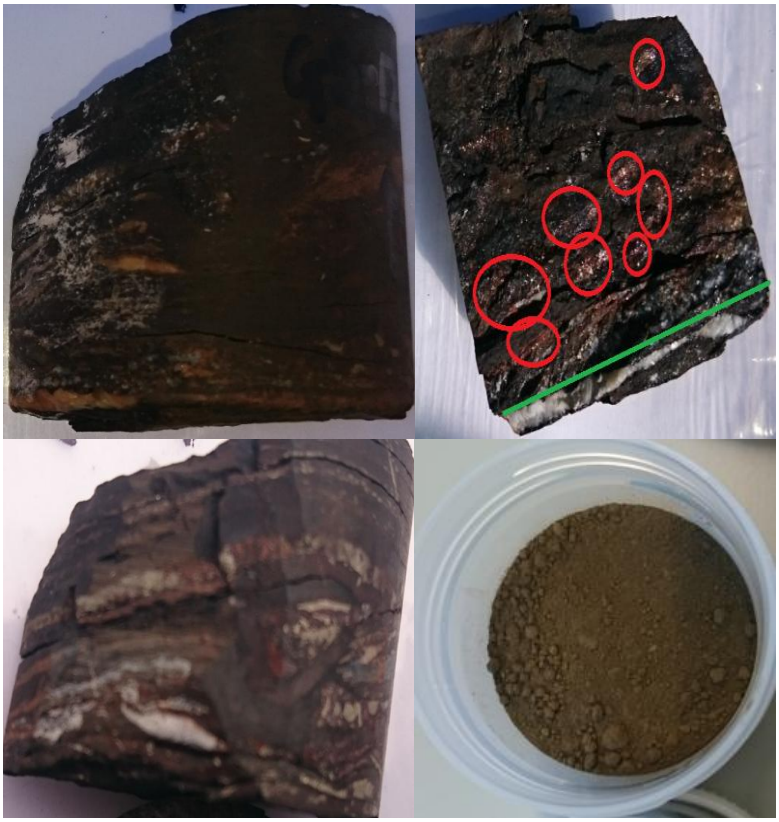

Figure A12: Pictures of GAS S12
A12a. Top left. Outside view of the sample prior to polishing.
A12b. Top right. Inside view of the sample prior to polishing. We can see a lot of orange-to-purple coloured minerals in the red circles. Below the green line is a secondary calcite vein that has been sawn off.
A12c. Bottom left. Outside view of the sample after polishing.
A12d. Bottom right. Sample powder after grinding.

Sample **HEX S1**

This is a sample that consists of three fractured pieces. They are a deep black colour with no clear indicators of weathering. There is no bedding, which is also in agreement with the absence of biotite in the sample. Some grey-to-white specks have been identified on the surface of the samples. Based on the mineralogy of the sample these specks most likely correspond with one or both of the two Fe-carbonates that is present in the sample, siderite or ankerite.

Figure A16: Pictures of sample HEX S1
A16a. Side view of the samples prior to polishing.
A16b. Samples prior to polishing.
A16c. Sample powder after grinding.

Sample **HEX S2**

The sample is a dark-coloured, fine-grained, mudstone which shows no clear signs of weathering. Within the sample we can see one clear pyrite vein (Fig. A17a and A17b). This mm-scale vein has a 70 degree angle with the bedding of the sample. The homogeneity of the sample in its appearance is also reflected in its mineralogy which is completely dominated by stilpnomelane with only minor fractions of pyrite, magnetite, biotite and clinochlore are also present.

Figure A17: Pictures of sample HEX S2
A17a. Inside view of the sample prior to polishing. We can see that there are no weathering indicators and we can see the main vein running from top right to bottom left.
A17b. Outside view prior to polishing. There are no clear weathering indicators. We can see the main vein running on the right side.
A17c. Sample powder after grinding.

Sample **HEX S3**

This broken sample is a dark-coloured, fine-grained, mudstone. It is very similar to sample HEX S2 in both appearance and mineralogy. The visual homogeneity of this sample is also reflected in the mineralogy which is dominated by stilpnomelane. Minor fractions of pyrite, magnetite, biotite and clinochlore are also present.

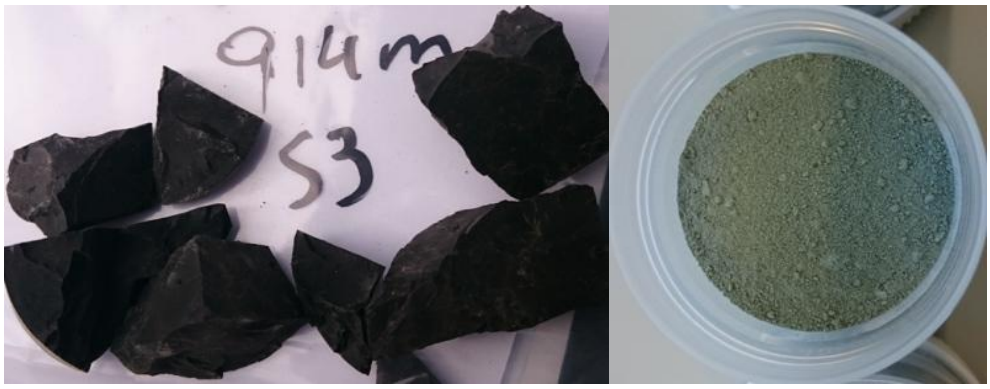

Figure A18: Image of sample HEX S3
A18a.View of the sample prior to polishing.
A18b. Sample powder after grinding.

Sample **ARP S1**

The sample is a dark-coloured, fine-grained, mudstone. The sample appears a homogeneous dark colour with no significant features. The main mineralogy of the sample is composed of quartz and stilpnomelane. The other minerals that are present in the sample are clinochlore, ankerite, magnetite and pyrite.

Figure A15: Pictures of sample ARP S1
A15a. Outside view of the sample prior to polishing.
A15b. Inside of the sample prior to polishing.
A15c. Sample powder after grinding.

Sample **ARP S2**

The sample is a dark-coloured, fine-grained, mudstone. The top and bottom surfaces contained some white-to-grey weathering layers which were only present on the surface. The homogeneous appearance of the sample is also reflected in the mineralogy, which is predominantly stilpnomelane and quartz.

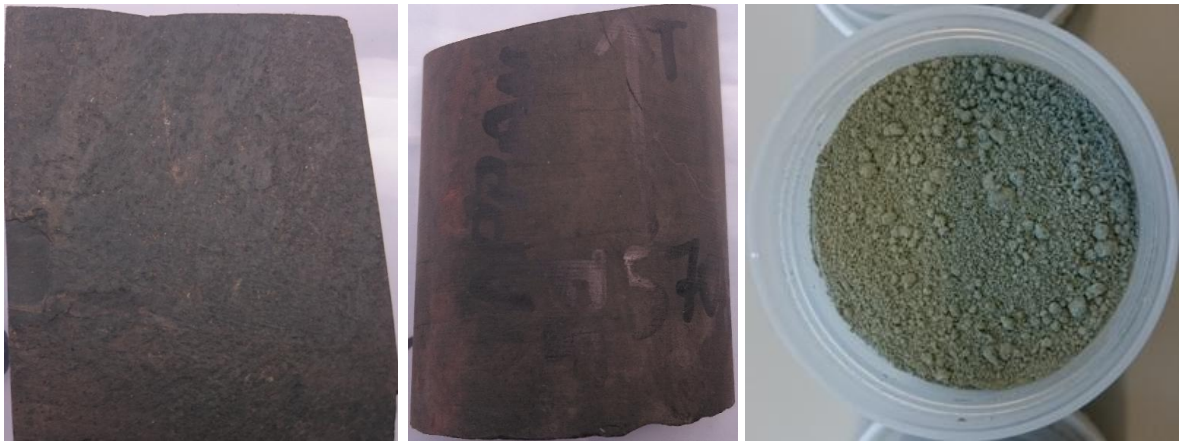

Figure A14: Pictures of sample ARP S2
A14a. Inside view of the sample prior to polishing. Some signs of weathering are visible in discolorations
A14b. Outside view of the sample prior to polishing. The discolorations are heavier than on the inside of the sample indicating that more weathering has taken place.
A14c. Sample powder after grinding.

Sample **ARP S3**

The sample is a dark-coloured, fine-grained, mudstone. The sample has clearly weathered, because its colour changed dramatically during sample preparation. The sample contains multiple secondary pyrite veins of various thicknesses, with the thickest of them around 2 mm thick, cutting through the sample (Fig. A13b, red line). Two other veins are of a smaller <1mm scale and do not reach through the entire sample (Fig. A13b, green line). Finally, pyrite is observed on one of the surfaces where it is a possible remnant of a pyrite vein since it has the same orientation as the other veins of about 70 degrees with the bedding (Fig. A13a). Even though the sample appears similar to the other samples only containing a few secondary pyrite veins, the mineralogy is distinctly different. Stilpnomelane is almost completely absent and the main mineral in this sample are magnetite and quartz.

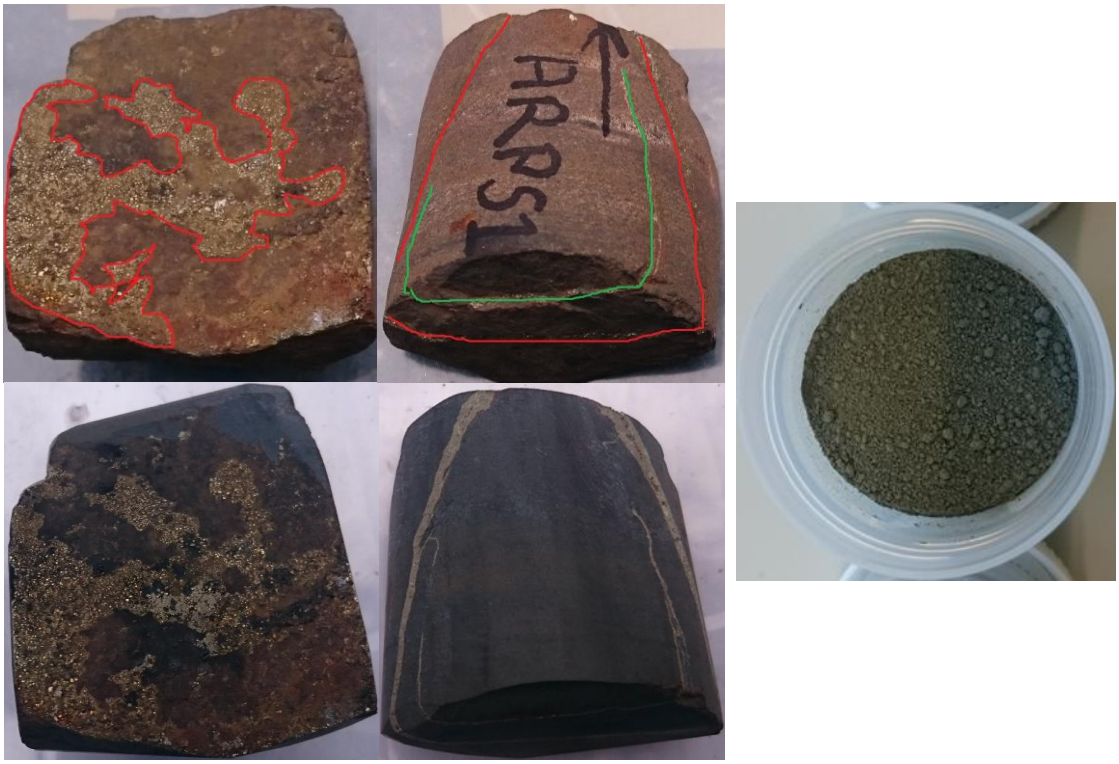

Figure A13: Pictures of ARP S3

A13a.Top left. Inside view of the sample prior to polishing. We can see the brown weathering colour on the surface as well as a large concentration of pyrite. The largest cluster of pyrite has been indicated with the red outline, but smaller specks are also present.

A13b.Top right. Outside view of the sample before polishing. This clearly shows the presence of the veins. The two biggest are indicated where the red one is significantly bigger than the green one.

A13c. Bottom left. Inside view of the sample after polishing.

A13d.Bottom right. Outside view of the sample after polishing.

A13e. Central right. Sample powder after grinding.

Sample **ERI S1**

The sample is a dark-coloured, fine-grained, mudstone which contains zones of dark coloured material. The brownish colours are regions where ankerite and pyrite have weathered. We can also see ankerite and pyrite being present on the inside of the sample before the polishing (Fig. A19a). After polishing we can see that these groups are actually parts of layers that are pyrite enriched layers (Fig. A19c). Two main lines can be identified; in the middle and near the bottom of the sample. When looking at the outside of the sample (Fig. A19d) we can also that see the central band is enriched in pyrite. On the other hand, the lower band is not visible throughout the entire sample, but only on the bottom left. Near the top the veins have become white, indicating that the orange colour resulted from weathering of the Fe in Fe-carbonates which, based on the mineralogy, is ankerite. While there is a lot of apparent heterogeneity, the vast majority of the sample is composed of stilpnomelane.

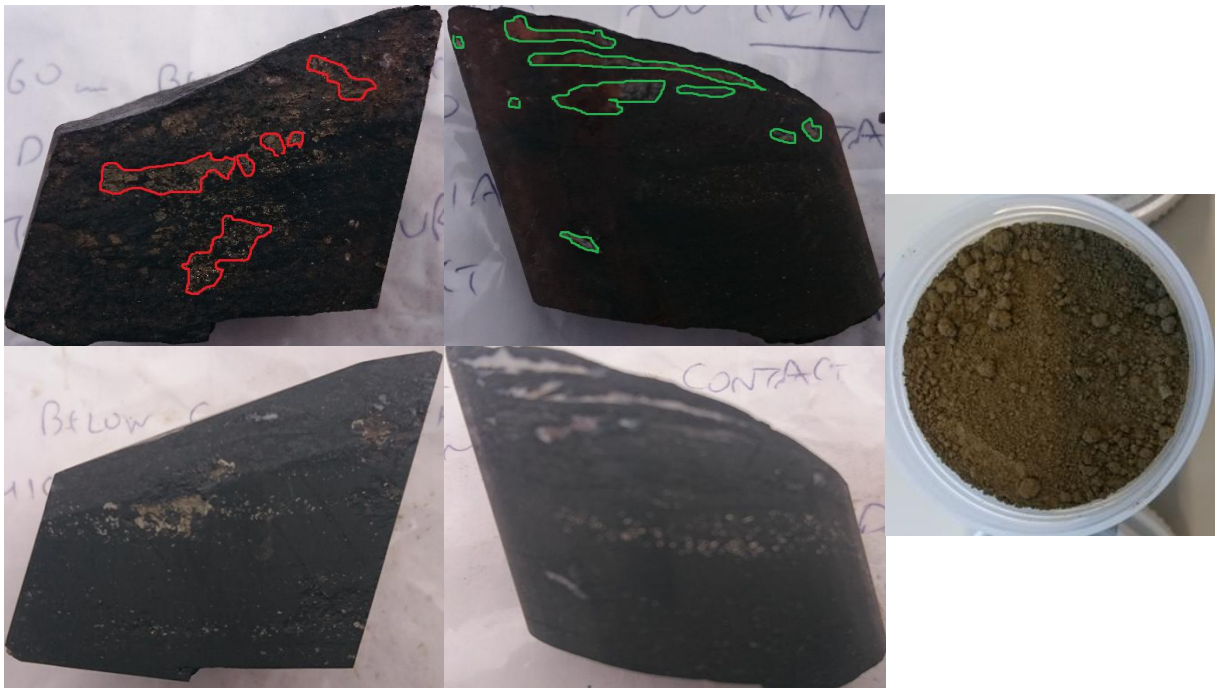

Figure A19: Pictures from ERI S1
A19a. Top left. Inside view of the sample prior to polishing. We can see some concentrations of pyrite, indicated in red.
A19b. Top right. Outside view of the sample prior to polishing. We can see veins and/or specks of an orange coloured material that is mainly concentrated in the upper part of the sample.
A19c. Bottom left. Inside view of the sample after polishing.
A19d. Bottom right. Outside view of the sample after polishing.
A19e. Central right. Sample powder after grinding.

Sample **ERI S2**

This sample is a dark-coloured, fine-grained, mudstone. It is homogeneous dark in appearance. Similar to the other homogeneously dark-coloured samples, the most common mineral is stilpnomelane, followed by quartz.

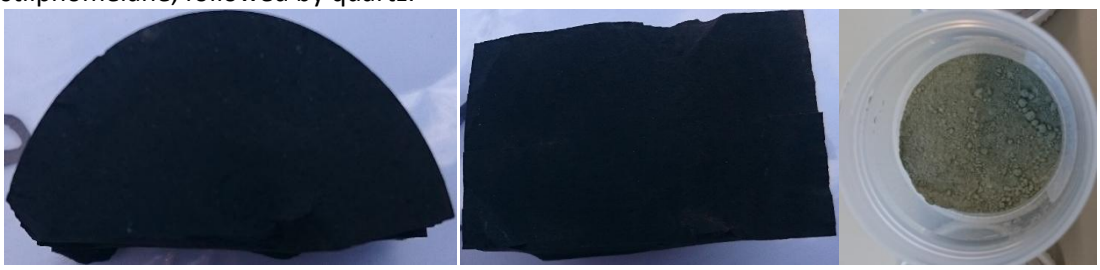

Figure A20: Pictures of sample ERI S2
A20a. Top view of the sample prior to polishing.
A20b. Inside view of the sample prior to polishing.
A20c. Sample powder after grinding.

Sample **MP53**

This sample is different from the other samples. Its colour varies from the usual black colours shown by the other samples. It is mostly of a dark-red or purple colour, indicating an increase in oxidised iron. The mineralogy is dominated by hematite. During polishing there was another indicator of the composition being different from the other samples in that its streak provided was purple-to-red rather than the grey or black streaks shown by other samples. Furthermore the sample proved very brittle as it broke in half during polishing indicating that it was layered. However, based on the mineralogy this layering is not caused by biotite, but instead by clinochlore. Furthermore, it is essentially the only shale ever to be found within the Hotazel BIF Formation. The shale is about 40cm-thick and occurs immediately below the topmost of the Hotazels three manganese layers (H. Tsikos, personal comm.).

Figure A21: Pictures of sample MP53: Black shale in BIF.
A21a. Bottom view of the sample prior to polishing.
A21b. Top view of the sample prior to polishing.
A21c. Sample powder after grinding.

XII: Appendix B: Description of Analytical Uncertainties

XRD:

The XRD is a qualitative method to infer the major mineralogy of the samples. The XRD has problems identifying minerals that form less than 5 wt% of the sample. The minerals present in small amounts will show low magnitude peaks, often indistinguishable from the background noise. For BIF samples this holds for e.g. minnesotaite/talc, greenalite, riebeckite and calcite. Another issue that arises is the inaccuracy of the XRD in multi-component systems. Generally three or four minerals can be identified from a single XRD plot with sufficient certainty, but for systems that contain more than four major minerals, like the stilpnomelane lutites, it becomes increasingly difficult to identify minerals. In the samples it was always possible to identify stilpnomelane, magnetite and pyrite. Identification of siderite, ankerite, quartz and biotite was also relatively easy if they were present in high enough quantities since they have very distinct peaks. However, the silicate minerals form a cluster of peaks in the 2Θ range of 20°-35°, making it difficult to identify the ones present.
For XRD it is assumed that, during analysis, the crystals in the powder all have a random orientation. Therefore difficulties may arise during the interpretation of the XRD pattern when there is a preferential orientation of the crystals. This can have profound effects on the magnitude of the peaks for different minerals. If there are minerals which have a preferred orientation, the ratio between different peak magnitudes for a single mineral can vary from the expected pattern. Sometimes they may even disappear. Since my samples were measured as powder instead of whole-rock this effect should be minimal. Peaks can also shift slightly as a result of the sample preparation. During the loading of the sample in the XRD sample-holder, if the powder contains a coarse grain, the surface of the powder may not be completely homogeneous, resulting in a peak shift. This can be prevented by compressing the sample, which itself may result in the crystals having a preferred orientation which will also affect the results. Therefore it is important to make sure your powder is finely grained and that sample compression is minimised during XRD analysis in order to minimise the effects this has on peak magnitude and position.

There is a peak at 2Θ = 44.5° which is present in nearly all of the measured samples. In certain samples, such as GS-9 and GS-12, it corresponds very well with a siderite peak. However, in the other samples it does not. Webb et al. (2003) attribute peaks close to this wavelength to quartz and to siderite, but it is unlikely that this peak is related to siderite since the major peak for siderite, related to its carbonate bond, at 2Θ = 37.5°, is absent. It cannot be explained by a preferred crystallographic orientation either, because the peak at 2Θ = 44.5° is present in fourteen samples that do not contain the other major peaks of siderite. It is very unlikely that there would be a similar preferential orientation of crystals in all of the samples that suppresses the same major peak every time. Therefore it is unlikely that this is a peak related to siderite. It is not likely that the peak corresponds to quartz either. A similar reasoning can be applied to quartz, the major peaks for quartz at 2Θ = 31° are missing from the patterns that show the unknown peak. Since no mineral could be found that fits the unknown peak as well as the low-grade metamorphic conditions experienced by the rocks in the Griquatown and Kuruman BIFs it was not possible to identify a mineral for this peak.

ICP-OES and ICP-MS:

For both ICP-OES and ICP-MS techniques, the sample preparation procedure is crucial. Incomplete digestion of the samples will yield inaccurate results. Complete digestion was attained by the HF-$HClO_4$-HNO_3 procedure for most samples. H_2O_2 and HCl were added to samples that were not fully digested following the HF-$HClO_4$-HNO_3 procedure. Recoveries for ICP-OES and ICP-MS were computed by comparing the processed and measured ISE-921 values to their reference values. Values between 85% and 115% were considered to be reliable results. Not all of

Element	ICP-OES(%)	ICP-MS (%)
Be	82.1-83.4	106.4
Co	86.9-96.5	123.1
Cu	93.8-103.8	120.6
Tl	N/A	128.7
V	99.0-100.0	124.2
Y	82.3-83.0	74.7
Zr	41.2-43.0	46.4

Table B1: Anomalous recoveries that were obtained for the ICP-OES and ICP-MS measurements. Values indicated in red show anomalously high or low recoveries.

the analysed elements had recoveries that were within this range. The ICP-OES recoveries yielded low values for Be, Y and Zr, no high recoveries were recorded (Table B1). ICP-MS recoveries yielded low values for Y and Zr. High recoveries were found for V, Co, Cu and Tl (Table B1). Moreover, due to an incomplete reference dataset recoveries could not be computed for Cs, Pr, Sm, Eu, Gd, Tb, Dy, Ho, Er, Tm, Yb, Lu, Hf, Ta and Re. The low recovery of Zr is possible if zircons, for example, were not digested. Another explanation might be that during the preparation it is possible that Zr-Y complexes form which are very hard to digest, resulting in low recoveries for both. The low recovery of Be in ICP-OES can be explained by the fact that the concentrations of Be are very low and close to its practical detection limit. So, small variations in the measured counts concentration can have a large effect on the recovery. The low or high recoveries associated with these elements means that is a possible uncertainty associated with their concentrations.

Further uncertainties are present for values that are above the line range or below the practical detection limit. These values will have to be used with caution as there can be >10% uncertainties involved with these values. The detection limit and line range were determined individually for each element in each sample by multiplying the practical detection limit or line range of an element by the dilution factor of the sample. Values that are below the Background Equivalent Concentration (BEC) value also contain relatively large uncertainties. The BEC value is the concentration of an element which would produce the same emission intensity as the background plasma for a certain wavelength. It is dependent on the alignment of the plasma torch, the viewing height of the plasma, the gas flow rate through the nebuliser and the power of the incident radio-frequency. Values that are below the BEC should generally be treated as indicative values only.

Different types of interferences may affect the measurements of ICP-OES and ICP-MS instruments. For ICP-OES spectral interference may affect the resulting dataset. Every element has a set of different specific wavelengths based on the energy released during excitation-relaxation cycles between different electron orbits. In some cases the specific wavelength of different elements can be close together, which means that they could affect each other's pattern, resulting in errors. This effect is minimized by looking at various known specific wavelength of elements. These different wavelengths are subsequently compared to test the reliability of the results.

There are two types of interferences that are present for ICP-MS analysis; isobaric and polyatomic interferences (Date et al., 1987). Isobaric interferences are those which arise due to two different atoms having isotopes of the same mass. This implies that one intensity peak may contain counts from different elements. Polyatomic interferences are interferences that are related to the formation of atomic complexes where atoms from the sample matrix bond with atoms from the diluent or the argon plasma (May and Wiedmeyer, 1998). Since these polyatomic complexes will have a different mass, they are able to interfere in the signals of heavier elements. These interferences are mitigated by measuring another isotope of these elements. Subsequently, corrections can be made using the known natural ratios between the different isotopes to determine the total amount of the element that is present (Neubauer, 2010). These corrections can be performed for all elements, except In since this is used as internal standard, as a result these interferences are implicitly corrected for in the instrument (Date et al., 1987). The quality control of the results was determined using external reference material, ISE-921. These values showed recoveries between 85 and 115%. The obtained values were within the range of the standard deviations, implying that there were no polyatomic interferences.

The matrix elements are the elements that are present in the diluents and the plasma torch. Drift can be caused by material collecting on the analytical components of the instrument. These elements may form solids that can coat the sampler or clog the skimmer cone, the part through which the ions are introduced to the mass spectrometer which will result in a drift of the signal (Gross et al., 2009). The drifting of the signal may result in spectral overlap. Drifts were measured for the ICP-MS results,

these indicated that variations in the drift during the runtime of the instrument were within the bounds of the standard deviation, implying that there are no substantial instrumental errors.

Uncertainties may also arise from matrix effects in the instrument. The matrix effects are dependent on the concentration and can therefore be minimised by diluting the sample (Tan and Horlick, 1987). Sample dilution is done to free the elements in the sample for analysis. To prevent clogging the instrument, which affects results, less than 0.2 wt% of the sample should remain as dissolved solid (Wolf, 2005). Dilution factors of the samples all exceed 200 times dilution, indicating that the samples were sufficiently diluted to exclude matrix effects.

XRF:

Recoveries for XRF were computed by comparing the measured standard materials to the reference values. Different standards were used for the different techniques. For the fusion beads ISE-921 was used as standard while AGV-1 was used for the pressed powder pellets. For the recoveries, values between 90 and 110% compared to their reference values were considered to be reliable. Not all of the analysed elements had recoveries that were within this range. Low recoveries were found for Ba, while high recoveries were found for As, Ni and P_2O_5 (Table B2). X-ray fluorescence studies rely on the absorption of emitted photons with characteristic wavelengths for each element. A complicating factor arises for the elements with multiple electron shells. In an ideal situation, only the electrons from the inner orbitals would be affected by the incident X-rays. However, in reality electrons from higher orbits are also affected by these X-rays, albeit on a smaller scale. The wavelength of the photons emitted by electrons that fall into higher electron orbitals is different from those that fall to the inner orbital, because the energy difference between orbitals is not constant for an element. This implies that the amount of possible spectral lines that can be produced increases with atomic numbers as elements with a higher atomic number will contain more electron orbitals than those with low atomic numbers (Feret et al., 2003).

Compound	Recovery (%)
As	171.1-185.9
Ba	84.5-85.2
Ni	128.4-128.7
P_2O_5	116.9-117.1

Table B2: Anomalous recoveries that were obtained for XRF measurements. As, Ba and Ni were determined using the pressed-powder pellet method, P_2O_5 using fusion beads.

The quality of XRF analyses can be checked by looking at the sum of the major element oxides and the LOI, which should add up to 100% (Webb et al., 2003). The average over the sample range is 99.3±1.5 wt%, implying a high-quality XRF analysis. However, these sums were computed using Fe_2O_3 for the Fe-oxide abundance, while the XRD implies that the majority of the Fe is stored as ferrous iron in Fe-carbonates, silicates, pyrite and magnetite. Recalculation of the Fe-abundances using FeO yields an average sum of 95.6±1.8 wt%, which would imply a larger uncertainty on the XRF data. The real value will be somewhere between the two extremes as Fe(III) is incorporated in minerals as well.

CS-Analyser:

For the CS-analyser there is a large uncertainty in high-S values. For the data that was obtained during the first run, this was caused by malfunction in the high sulphur detector. This means that, for high S concentrations, the resulting values should be seen as indicative values rather than accurate and precise results, although the quantitative measurements of one sample containing more sulphur than another still holds. To be more qualitative, a second run was analysed without any problems. When the results of the two runs are compared, we can see that the second run has a

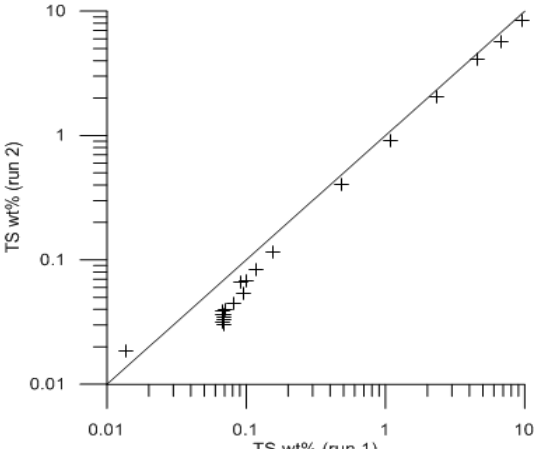

Figure B1: This figure illustrates the correlation between the two separate instances where TS was determined using the CS-analyser.

consistently lower S-content than the first run, with the exception of sample GAS S10 (Fig. B1). There is a very strong correlation between the two results, but it does not plot on a one-to-one line, this is most likely caused by different calibrations for each run. The results of the second run will be used for further work, since I am uncertain about the quality of the first run.

CRS:

The Utrecht Extractions

The distillation based AVS/CRS extraction is an experimental procedure and as such it contains various uncertainties that can yield inaccurate results in the end. First of all the $H_2S(g)$ that forms following the reduction of the pyritic S to S(-II) might escape. $H_2S(g)$ can escape in various means, first of all, if the sulphur content of the sample exceeds that of the silver nitrate trap not all the sulphur is converted to $H_2S(g)$ will be converted to $Ag_2S(s)$ since there is insufficient $AgNO_3$. The chances of this occurring have been mitigated by determining the molar abundances of S in the samples and making sure that there is a clear excess of $AgNO_3$ in the sulphide trap. Secondly, $H_2S(g)$ could escape before reacting with the $AgNO_3$, if the residence time in the trap is too low. The residence time depends on the bubbling rate through the trap solution. By sticking to the prescribed procedure of approximately two bubbles per second this effect has been minimised. Finally, the $H_2S(g)$ can escape from the system if it contains leaks. The presence of leaks has been prevented by greasing all of the contacts and covering them with Parafilm® prior to the experiment.

Another issue which can yield inaccurate results is that not all the sulphur is converted to $H_2S(g)$. This can also be caused by various points. The simplest explanation is that there was not enough time for all of the sulphides to react and form $H_2S(g)$. This is excluded by applying a run-time of the experiment anywhere between two and three hours while the majority of the sulphide will react within the first hour. Another way for incomplete conversion is that not all of the sulphur is liberated because there is an oxidised or organic component to the sulphur that is present in the samples. The AVS/CRS technique only works in liberating reduced sulphur such as that found in elemental sulphur and mono- and di-sulphide minerals like pyrite. However, the technique only works partially on oxidised sulphur (Canfield et al., 1986). Therefore the presence of an oxidised S component would result in an incomplete yield of the sulphur from the sample. Oxidised sulphur compounds will generally form sulphates and subsequently sulphate minerals. While there are reports of sulphate minerals in the Archean, such as barite (Huston and Logan, 2004), their presence is not constant through time and there is no evidence that there was a sulphate concentration capable of forming sulphate minerals during the deposition of the Griquatown BIF approximately 2.4Ga. In fact, there appears to be a large gap in sulphate deposition between 3.2 Ga and 2.2 Ga (Huston and Logan, 2004). This, combined with the low oxygen concentrations in the Archean atmosphere, around 10^{-5} PAL (Pavlov and Kasting, 2002), means that it is unlikely that there was a major oxidised sulphur component. Furthermore, based on XRD no sulphate minerals have been identified while pyrite was ubiquitously present. Therefore it is safe to assume that the sulphur is all stored in sulphide minerals, almost exclusively pyrite, and that the CRS method will extract all of the sulphur from the sample. This indicates that it is not required to perform acid volatile sulphur (AVS) extractions to extract oxidised sulphur compounds.

While I aim for recoveries of 100% I will have to remember that the distillation based CRS methods do not yield an average recovery of 100%. Groger et al. (2009) reported recovery values for pyrite of 98.1±1.44% while Canfield et al. (1986) reported 95.8%. This incomplete recovery may inherently result in fractionation of the sulphur isotopes, because the isotopic composition can vary with location in the pyrite crystal (Gregory et al., 2015). In my experiments in Utrecht I measured a consistently low or even negative recovery for all samples with values between -15.5 and 25.3 %. This implies that material is either lost or not liberated during the experiment. The low recovery may be related to the filtration technique that was applied. Cellulose acetate filters were used and during filtration, the trapped precipitate was rinsed with UHQ water and ammonium hydroxide (NH_4OH). It

is apparent that the cellulose acetate filters and the NH_4OH solution are incompatible. This resulted in the partial breakdown of the filter as it is being rinsed with NH_4OH. The reaction taking place between the filter and the NH_4OH could partially explain the consistent sub-par recoveries. Corrections were made by testing the weight-loss of ten blank filters after rinsing them with NH_4OH. This showed that there was a significant loss of mass using dry filters. Two rinses with NH_4OH resulted in a weight-loss of 2.46 and 1.19 mg of the cellulose acetate filters. Correction of the resulting yields for the mass loss of the filters turned out to be insufficient to explain the low recoveries. This implies that mass is lost elsewhere, an explanation is that the breakdown of filters by the NH_4OH creates gaps in the filter through which material is removed during the filtration process. Another explanation can be found by explaining incomplete sulphide liberation or leaks during the experiment as a cause for the extra loss of mass on top of that which is attributed to the breakdown of the filters. However, it is unlikely that it is the result of leakage because first of all the systems were thoroughly checked and all connections were sealed using Parafilm®. Furthermore, all of the used columns show anomalously low recoveries. This would imply similar leakage in all three columns, which is unlikely. The only way this could be explained is by a flawed set-up.
The set-up can be flawed, because the samples were not heated during the experimental procedure in Utrecht. The results in Münster have shown that heating the samples is a necessity for a good recovery. For sample ARP S1 the obtained recovery, 60.2%, is significantly lower than the recovery of the other samples, implying that heating the sample is an instrumental part of the extraction procedure.

<u>The Münster Extractions</u>
The recoveries in Münster have shown that there were no issues regarding leaks and/or mass loss during the experiment. An air-tight seal between ground glass joints was achieved by wetting the joints before connecting the pieces. Furthermore, there is also no indication that mass was lost during the filtration. This is another indicator that the cellulose acetate filters that were used during the extractions in Utrecht resulted in the partial loss of material as shown before. Only minor amounts of sample may have been lost during the extraction procedure where the $H_2S(g)$ entered the Zn-acetate solution. There was minor precipitation of ZnS on the inside of the tip of the glass tubes. This was partially removed using a piece of wire to scrape it out, however not all of the material could be liberated, but this is only a minor amount compared to the bulk of, on average, 30 mg of Ag_2S. Therefore it is unlikely to have a profound effect on the isotopic composition of the samples.

Factor	Utrecht	Münster
Reagents	30 ml $CrCl_2$ in 6M HCl	20 ml HCl + 30 ml 1M $CrCl_2$
Heating	No heating	Constant heating at 85°C in a heating mantle
Catalyst	No catalyst	10 ml ethanol
Trap solution	1-5 ml $AgNO_3$ with 2 ml 1.5M HNO_3 and 15 ml H_2O	Zn-acetate (4%) in acetic acid. $AgNO_3$ was added after extraction
Acid trap	No acid trap	Distilled H_2O acid trap
Filters	Cellulose acetate	Cellulose nitrate

Table 6: A brief summary of the differences between the sulphur extraction methods that were used in Utrecht and Münster. The most important differences are found in the heating and type of filters.

A comparison of the experimental set-up in Utrecht and in Münster has shown that various improvements can be made with regards to the technique used in Utrecht. First of all, the samples should be heated and stirred and not just stirred during the extraction. The heating allows for faster

and more complete liberation of sulphides. Correcting for the mass loss during filtration proved insufficient to explain the low recoveries. Furthermore, the use of cellulose acetate filters in Utrecht prove detrimental to the yields as both mass and filter were lost during the rinsing with a NH_4OH solution. This can be prevented by switching the type of filter from cellulose acetate to cellulose nitrate, which is stable when rinsed with NH_4OH.

References

Canfield, D.E., Raiswell, R., Westrich, J.T., Reaves, C.M., Berner, R.A. (1986). The use of chromium reduction in the analysis of reduced inorganic sulfur in sediments and shales. Chemical Geology, vol. 54, p. 149-155

Date, A.R., Cheung, Y.Y., Stuart, M.E. (1987). The influence of polyatomic ion interferences in analysis by inductively coupled plasma source mass spectrometry (ICP-MS). Spectrochimica Acta Part B: Atomic Spectroscopy, vol. 42, p. 3-20

Feret, F.R., Hamouche, H., Boissonneault, Y. (2003). Spectral Interference in X-ray Fluorescence Analysis of Common Materials. International Centre for Diffraction Data 2003, Advances in X-ray Analysis, vol. 46, p. 381-387

Gregory, D.D., Large, R.R., Halpin, J.A., Steadman, J.A., Hickman, A.H., Ireland, T.R., Holden, P. (2013). The chemical conditions of the late Archean Hamersley basin inferred from whole rock and pyrite geochemistry with $\Delta^{33}S$ and $\delta^{34}S$ isotope analyses. Geochimica et Cosmochimica Acta, vol. 149, p. 223-250.

Groger, J., Franke, J., Hamer, K., Schulz, H.D. (2009). Quantitative Recovery of Elemental Sulfur and Improved Selectivity in a Chromium-Reducible Sulfur Distillation. Geostandards and Geoanalytical Research, vol. 33, p. 17-27

Gross, C.T., McIntyre, S.M., Houk, R.S. (2009). Reduction of Matrix Effects in Inductively Coupled Plasma Mass Spectrometry by Flow Injection with an Unshielded Torch. Analytical Chemistry, vol. 81, p. 4898-4905

Huston, D.L., Logan, G.A. (2004). Barite, BIFs and bugs: evidence for evolution of the Earth's early hydrosphere. Earth and Planetary Science Letters, vol. 220, p. 41-55

May, T.W., Wiedmeyer, R.H. (1998). A Table of Polyatomic Interferences in ICP-MS. Atomic Spectroscopy, vol. 19, p. 150-155.

Neubauer, K. (2010). Reducing the Effects of Interferences in Quadrupole ICP-MS. Spectroscopy

Pavlov, A.A., Kasting, J.F. (2002). Mass-Independent Fractionation of Sulfur Isotopes in Archean Sediments: Strong Evidence for an Anoxic Archean Atmosphere. Astrobiology, vol. 2, p. 27-41

Tan, S.H., Horlick, G. (1987). Matrix-effect Observations in Inductively Coupled Plasma Mass Spectrometry. Journal of Analytical Atomic Spectrometry, vol. 2, p. 745-763

Wolf, R.E. (2005). What is ICP-MS? ... And more importantly, what can it do? http://crustal.usgs.gov/laboratories/icpms/intro.html

XIII: Appendix C: Complete XRF Dataset

Fusion bead analysis - Major element oxides

Sample	SiO_2 (%)	Al_2O_3 (%)	TiO_2 (%)	Fe_2O_3 (%)	MnO (%)	CaO (%)	MgO (%)
GAS S1	47.3	5.43	0.14	30.2	0.33	0.57	8.17
GAS S2	47.3	4.25	0.07	33.7	0.17	0.16	7.23
GAS S3	47.0	4.90	0.07	33.2	0.05	0.14	8.40
GAS S4	46.2	4.02	0.11	32.7	0.11	0.90	7.29
GAS S5	44.9	3.76	0.22	38.2	0.09	0.23	6.37
GAS S6	45.8	5.03	0.26	34.2	0.04	0.21	7.58
GAS S7	46.5	6.05	0.11	30.1	0.06	0.18	9.57
GAS S8	43.4	6.01	0.22	37.2	0.10	0.14	5.88
GAS S9	27.4	1.92	0.05	47.9	0.67	0.95	3.76
GAS S10	43.8	7.24	0.16	32.9	0.11	0.19	6.51
GAS S11	41.7	5.32	0.31	37.0	0.06	0.14	4.53
GAS S12	26.2	2.13	0.07	46.0	0.41	2.67	3.49
HEX S1	26.8	3.84	0.27	35.1	0.84	8.31	4.37
HEX S2	43.8	6.04	0.81	35.0	0.33	0.66	5.51
HEX S3	43.9	7.00	0.14	31.4	0.09	0.11	8.90
ARP S1	44.1	7.13	0.57	33.3	0.13	0.45	6.56
ARP S2	54.1	8.68	0.47	21.6	0.23	0.26	3.42
ARP S3	38.6	0.26	0.01	50.4	0.17	2.49	1.22
ERI S1	44.1	3.75	0.16	38.8	0.31	0.98	3.62
ERI S2	43.7	5.38	0.33	37.7	0.21	0.22	5.16
MP53	18.7	5.11	0.05	64.7	0.26	1.24	5.15

Sample	Na_2O (%)	K_2O (%)	P_2O_5 (%)	LOI (%)	Sum
GAS S1	0.96	1.94	0.01	5.36	100.4
GAS S2	0.83	1.74	0.05	4.71	100.2
GAS S3	0.53	2.76	0.02	3.66	100.7
GAS S4	0.71	1.72	0.04	6.59	100.4
GAS S5	0.25	2.83	0.03	3.84	100.7
GAS S6	0.46	2.73	0.03	3.64	100.0
GAS S7	0.54	3.28	0.01	4.24	100.6
GAS S8	0.19	3.90	0.01	3.09	100.2
GAS S9	0.17	1.27	0.21	15.4	99.8
GAS S10	0.37	4.49	0.02	3.82	99.6
GAS S11	0.35	3.20	0.03	6.61	99.3
GAS S12	0.18	1.29	0.00	13.8	96.3
HEX S1	0.55	1.09	0.07	14.1	95.4
HEX S2	0.58	1.91	0.11	4.42	99.1
HEX S3	0.64	2.90	0.01	4.68	99.8
ARP S1	0.26	0.87	0.12	5.02	98.5
ARP S2	0.36	6.62	0.07	2.38	98.3
ARP S3	0.04	0.13	0.11	3.76	97.2
ERI S1	0.64	1.60	0.14	4.93	99.0
ERI S2	0.50	1.52	0.07	5.09	99.9
MP53	0.01	0.02	0.81	4.19	100.2

Pressed Powder Pellets - Trace Elements

Sample	As (ppm)	Cu (ppm)	Pb (ppm)	Zn (ppm)	Ni (ppm)	Cr (ppm)	V (ppm)
GAS S1	0.96	10.5	5.73	37.6	7.35	6.85	8.16
GAS S2	3.20	30.1	3.19	31.2	9.31	11.5	12.1
GAS S3	2.43	12.1	3.60	24.8	7.15	8.39	6.50
GAS S4	4.11	21.3	4.10	67.1	16.2	14.7	28.3
GAS S5	5.94	50.9	4.01	52.1	18.9	12.5	16.3
GAS S6	7.22	12.6	2.23	28.1	11.7	4.39	6.10
GAS S7	1.50	28.0	6.92	40.7	10.0	2.34	5.73
GAS S8	6.06	30.1	4.30	126	68.3	10.5	31.0
GAS S9	13.6	64.3	24.6	90.1	20.1	7.89	16.5
GAS S10	4.58	26.8	4.41	56.6	26.6	13.0	28.1
GAS S11	165	23.4	21.0	85.1	175	47.9	49.9
GAS S12	54.2	113	39.8	102	136	11.4	19.5
HEX S1	-	-	-	-	-	-	-
HEX S2	5.14	82.9	9.73	42.0	40.1	40.4	106
HEX S3	1.17	38.9	5.50	27.8	7.51	5.36	7.58
ARP S1	2.77	69.8	7.31	46.0	47.0	46.8	91.2
ARP S2	2.91	36.9	5.76	28.3	43.3	88.2	60.9
ARP S3	37.4	76.7	15.7	36.2	21.6	4.92	3.27
ERI S1	35.5	103	11.6	32.8	30.4	23.2	25.4
ERI S2	-	-	-	-	-	-	-
MP53	9.92	24.4	8.27	48.9	21.3	5.37	9.48

Sample	Sr (ppm)	Ba (ppm)	Rb (ppm)	Ga (ppm)	Zr (ppm)	Nb (ppm)	Y (ppm)
GAS S1	17.0	150	160	6.23	132	6.78	10.4
GAS S2	14.2	81.3	152	4.34	45.7	3.56	6.52
GAS S3	22.9	52.3	331	6.39	83.3	7.68	5.93
GAS S4	21.0	75.8	138	5.71	37.3	4.11	8.50
GAS S5	14.3	34.8	361	4.81	84.9	5.19	10.1
GAS S6	30.0	70.5	333	5.95	228	10.4	11.1
GAS S7	26.6	110	399	7.62	175	16.0	16.0
GAS S8	16.1	87.7	619	6.79	102	11.0	10.7
GAS S9	18.7	26.9	180	4.61	14.0	2.61	18.6
GAS S10	22.3	164	659	11.0	68.1	13.2	17.2
GAS S11	16.6	120	462	8.89	73.8	5.91	22.1
GAS S12	184	41.0	148	5.44	20.0	2.55	9.31
HEX S1	-	-	-	-	-	-	-
HEX S2	17.4	121	112	9.16	85.9	5.59	20.7
HEX S3	10.7	145	285	6.14	156	6.61	7.93
ARP S1	9.15	49.7	52.1	11.9	86.4	5.71	16.5
ARP S2	17.7	279	170	8.68	87.1	5.84	10.9
ARP S3	23.6	28.8	11.3	1.68	10.3	1.68	4.61
ERI S1	6.81	161	115	4.82	41.1	3.51	9.25
ERI S2	-	-	-	-	-	-	-
MP53	16.6	9.80	3.22	4.91	42.5	3.96	24.1

Sample	La (ppm)	Nd (ppm)	Th (ppm)	U (ppm)
GAS S1	-1.35	1.45	8.17	1.97
GAS S2	0.21	3.14	8.09	1.79
GAS S3	-2.03	1.42	9.13	1.57
GAS S4	2.97	5.60	-3.79	3.95
GAS S5	7.63	4.17	9.18	2.51
GAS S6	37.8	34.2	6.17	2.21
GAS S7	32.6	21.3	28.3	5.14
GAS S8	12.2	11.2	17.8	7.09
GAS S9	3.66	6.33	-1.77	0.29
GAS S10	23.8	12.2	20.3	5.68
GAS S11	12.3	10.7	7.81	3.24
GAS S12	3.60	4.00	-0.11	0.49
HEX S1	-	-	-	-
HEX S2	9.18	6.28	3.17	1.34
HEX S3	42.3	26.0	6.07	2.80
ARP S1	13.9	10.2	-0.41	-0.81
ARP S2	21.1	6.63	9.89	2.25
ARP S3	2.36	5.20	-0.65	0.14
ERI S1	8.59	1.49	0.67	0.18
ERI S2	-	-	-	-
MP53	5.56	8.36	17.6	6.29

Values indicated in red are values that are below the detection limit for the specific element.
Elements shown in orange only give indicative values.
Samples ERI S5 and HEX S1 had insufficient sample to make a pressed-powder pellet.

XIV: Appendix D: Complete ICP-OES Dataset

Sample	Dilution	Al (ppm)	Ba (ppm)	Be (ppm)	Ca (ppm)	Ce (ppm)	Co (ppm)	Cr (ppm)
GAS S1	191	27832	161	< -0.26	8137	24.1	26.0	< 3.58
GAS S2	205	20955	85.8	1.88	756	18.9	28.5	< 7.61
GAS S3	172	24185	59.4	1.10	848	15.4	13.9	< -1.99
GAS S4	516	20137	84.3	1.11	7141	26.6	< 15.3	< 14.6
GAS S5	221	18700	35.6	1.27	1523	35.4	19.5	10.4
GAS S6	211	24573	79.6	1.59	1166	118	10.6	< -0.58
GAS S7	238	29635	114	1.30	919	80.1	< 6.77	< -2.20
GAS S8	245	29946	99.2	1.90	533	51.8	< 9.77	13.2
GAS S9	216	9760	29.5	1.77	8111	21.8	15.6	10.2
GAS S10	442	35728	19	2.35	818	61.1	< 9.79	< 13.3
GAS S11	505	26840	147	1.26	326	49.8	32.5	70.5
GAS S12	471	6546	29.3	0.20	13220	< 10.8	< 16.8	< 1.16
HEX S1	503	18963	61.1	< -0.23	64485	14.4	74.2	69.2
HEX S2	203	30454	143	0.49	4538	31.2	24.5	60.7
HEX S3	190	35044	164	< -0.23	262	125	< 5.51	< 0.29
ARP S1	204	36703	54.3	0.46	3024	37.2	31.6	70.9
ARP S2	219	44660	348	0.47	1666	47.5	26.6	111
ARP S3	202	1330	27.4	< -0.12	20486	14.0	21.7	< -0.80
ERI S1	207	18443	196	0.74	7817	34.2	21.6	32.0
ERI S2	215	27069	100	0.49	1235	22.5	49.9	66.2
MP53	354	24822	9.67	0.57	10469	72.5	32.3	< 5.74

Sample	Cu (ppm)	Fe (ppm)	K (ppm)	Li (ppm)	Mg (ppm)	Mn (ppm)	Na (ppm)
GAS S1	< -0.24	> 208589	15394	< 0.35	50079	2328	6772
GAS S2	< -0.12	> 248091	14255	1.92	45965	1284	6014
GAS S3	< -1.68	> 238543	22323	16.1	53441	316	3710
GAS S4	< -3.90	227042	13215	2.00	46901	814	5081
GAS S5	< -2.22	> 288939	23469	7.93	40703	594	1871
GAS S6	< -2.48	> 255313	22419	14.8	48316	275	3211
GAS S7	< -2.02	> 215841	26623	52.2	59314	415	4039
GAS S8	< -4.24	> 286073	31994	4.77	36631	682	1466
GAS S9	22.7	> 364083	10376	< 0.36	24279	5313	1360
GAS S10	< -4.22	236412	35980	3.36	41537	815	2398
GAS S11	< -3.48	268398	25910	4.08	30140	427	2264
GAS S12	26.5	206273	6075	< -1.28	14165	1907	607
HEX S1	27.1	245244	8160	< 1.36	26472	6192	3673
HEX S2	72.9	> 267959	15587	11.1	35394	2391	3996
HEX S3	< -4.27	> 230658	23480	19.5	57081	654	4435
ARP S1	48.7	> 259796	7080	17.3	43735	998	1999
ARP S2	18.6	166353	> 54205	8.15	20228	1597	2792
ARP S3	4.52	> 387665	1040	7.03	7901	1328	271
ERI S1	78.0	> 296803	12891	1.19	22851	2394	4483
ERI S2	20.0	> 288616	12397	6.09	32807	1530	3539
MP53	< -9.32	467425	< 136	16.9	35516	2083	< 145

Sample	Ni (ppm)	P (ppm)	Pb (ppm)	S (ppm)	Sc (ppm)	Sr (ppm)	Ti (ppm)
GAS S1	< 1.53	55.1	< 6.58	< 2.65	1.85	21.8	719
GAS S2	< 3.70	195	< 3.10	< 1.31	1.02	12.8	364
GAS S3	< 1.38	100	< 7.32	< 0.59	1.18	23.1	397
GAS S4	11.7	161	< 12.4	< 260	6.21	26.8	615
GAS S5	11.0	161	< 5.99	< 3.63	2.38	11.7	1211
GAS S6	3.78	150	< 5.43	< 2.09	4.03	29.5	1432
GAS S7	< 2.91	66.9	< 3.67	< 0.90	1.12	26.3	587
GAS S8	58.2	74.6	< 5.94	< 25.1	4.78	15.1	1150
GAS S9	11.1	854	< 6.96	48077	1.64	16.5	281
GAS S10	16.2	101	< 12.6	< 114	4.84	23.6	837
GAS S11	189	123	< 25.4	4273	14.9	17.4	1765
GAS S12	105	< 19.1	< 29.9	53248	2.98	120	219
HEX S1	99.8	304	< 35.4	22137	10.8	22.3	1476
HEX S2	30.9	460	< 10.5	1136	13.2	15.6	4495
HEX S3	< 1.11	67.4	< 6.95	< 4.79	2.59	9.03	756
ARP S1	38.4	485	< 7.60	642	11.8	7.25	3350
ARP S2	39.0	302	< 9.53	622	9.77	18.5	2716
ARP S3	7.99	441	< -12.8	> 58061	< 0.06	20.2	21.4
ERI S1	27.4	585	< 12.7	9828	4.57	5.18	924
ERI S2	30.5	273	< 6.26	451	5.63	4.36	1841
MP53	7.90	3419	< 33.7	351	2.56	13.5	289

Sample	V (ppm)	Y (ppm)	Zn (ppm)	Zr (ppm)
GAS S1	8.29	9.32	35.0	140
GAS S2	17.7	5.02	15.2	53.3
GAS S3	8.44	3.83	17.4	87.2
GAS S4	35.5	7.82	67.5	47.9
GAS S5	22.2	6.28	23.3	97.6
GAS S6	9.53	11.3	21.0	251
GAS S7	< 6.91	14.2	21.7	189
GAS S8	46.5	5.50	109	112
GAS S9	27.5	15.5	66.5	20.1
GAS S10	33.7	10.7	53.1	74.0
GAS S11	68.7	9.24	91.6	83.9
GAS S12	< 13.2	4.64	45.2	15.0
HEX S1	106	15.9	20.9	69.3
HEX S2	147	19.8	32.4	99.8
HEX S3	8.09	6.25	3.92	173
ARP S1	122	19.2	30.5	90.5
ARP S2	77.5	10.7	12.6	93.4
ARP S3	11.1	4.50	< 1.60	13.8
ERI S1	37.1	8.33	16.0	49.7
ERI S2	54.1	10.3	26.4	67.1
MP53	18.4	24.4	43.9	54.3

Values lower than the detection limit are given with a "<" symbol in front. Values more than two times the line range are given with a ">" symbol in front. Values below the Background Equivalent Concentration (BEC) are given in blue. All of these values can have an error of analysis larger than 10% and as such should be seen as an approximate value.

XV: Appendix E: Complete ICP-MS Dataset

Rare Earth Elements

Sample	La (ppb)	Ce (ppb)	Pr (ppb)	Nd (ppb)	Sm (ppb)	Eu (ppb)	Gd (ppb)	Tb (ppb)
GAS S1	6623	15331	1894	7190	1413	232	1412	225
GAS S2	6035	12595	1383	4702	771	168	756	104
GAS S3	2873	6571	844	3472	787	106	788	114
GAS S4	10991	22696	2796	10257	1725	289	1514	199
GAS S5	12638	26654	3029	10346	1557	247	1223	144
GAS S6	49478	118476	14239	50248	8008	1125	4869	452
GAS S7	37519	78786	8637	27705	4962	278	3901	498
GAS S8	21985	44395	4970	16900	2866	379	2149	228
GAS S9	5663	12078	1717	7755	2165	741	2738	395
GAS S10	30458	58971	6194	20021	3330	488	2663	320
GAS S11	21873	44034	5194	18963	3168	469	2418	263
GAS S12	5149	9986	1256	5106	1095	252	1175	172
HEX S1	2289	5780	1005	4925	1102	261	1357	228
HEX S2	11117	24051	3139	12706	2984	674	3023	429
HEX S3	58157	128530	15136	48171	5823	563	3196	286
ARP S1	15284	31389	3825	14568	3033	604	3051	434
ARP S2	21992	45782	5326	18673	3312	616	2580	305
ARP S3	1447	2577	392	1990	386	137	525	70.2
ERI S1	16315	27512	2924	9756	1341	215	1246	148
ERI S2	6790	14682	1827	7072	1452	300	1440	208
MP53	31014	66484	8075	29229	4581	736	4057	440

Sample	Dy (ppb)	Y (ppb)	Ho (ppb)	Er (ppb)	Tm (ppb)	Yb (ppb)	Lu (ppb)
GAS S1	1664	9239	330	1004	166	1123	176
GAS S2	772	5085	156	494	88.7	638	107
GAS S3	760	3737	132	352	58.0	360	55.7
GAS S4	1425	8464	267	782	132	878	154
GAS S5	947	5947	186	561	96.9	645	109
GAS S6	2436	11206	423	1250	203	1380	212
GAS S7	3244	14329	589	1665	267	1778	261
GAS S8	1319	5301	220	639	123	927	167
GAS S9	2711	15544	496	1332	201	1327	208
GAS S10	2089	10486	385	1209	229	1724	288
GAS S11	1585	8172	270	803	149	1135	227
GAS S12	1227	8233	245	760	138	1067	198
HEX S1	1955	15200	455	1531	274	1958	355
HEX S2	2940	15299	574	1688	267	1802	277
HEX S3	1468	5768	242	660	94.9	616	90.8
ARP S1	3122	16405	620	1796	272	1754	265
ARP S2	1903	8574	343	970	154	1035	164
ARP S3	550	4761	113	311	47.1	318	45.6
ERI S1	1064	8265	220	658	103	666	111
ERI S2	1506	9258	305	918	149	1002	164
MP53	2768	24808	540	1449	197	1199	204

Trace Elements

Sample	Li (ppb)	Be (ppb)	Ti (ppb)	V (ppb)	Cr (ppb)	Mn (ppb)	Co (ppb)	Ni (ppb)
GAS S1	2254	76.3	934357	6559	6616	2959345	32046	3003
GAS S2	2710	2743	477609	17011	12022	1624224	33584	5057
GAS S3	18471	1751	53298	3858	3098	402767	17090	2261
GAS S4	2960	1966	775415	38465	23286	906520	19090	12381
GAS S5	8865	1934	1536717	20522	14978	733664	22355	13737
GAS S6	15928	2288	1805577	6129	2451	335858	15259	6085
GAS S7	59264	2034	768621	5620	1261	503565	9629	4349
GAS S8	5872	2664	1430829	50853	16698	829548	13256	66853
GAS S9	953	2432	353660	24978	13892	6066735	17171	14079
GAS S10	3877	3132	996889	32746	16369	827397	11201	17546
GAS S11	5145	1922	2039276	68820	72385	447947	31694	169585
GAS S12	444	1530	423117	29497	13115	3690289	35657	174810
HEX S1	2346	418	1750065	115081	76536	6580130	77430	101032
HEX S2	18126	861	5369497	168163	69159	2693329	27314	36706
HEX S3	20572	110	897645	4843	3765	759534	7307	2432
ARP S1	16894	840	3691017	129598	75228	1113422	32415	40856
ARP S2	8782	819	3007894	83373	114590	1746831	27554	40492
ARP S3	9318	298	39796	3988	2270	1560242	23169	9657
ERI S1	1611	1137	1045783	33948	33944	2436743	21914	28404
ERI S2	6076	859	2030586	53189	68584	1633597	48099	32937
MP53	15628	1313	358247	12137	11579	2406245	34188	10047

Sample	Cu (ppb)	Zn (ppb)	Rb (ppb)	Sr (ppb)	Zr (ppb)	Nb (ppb)	Mo (ppb)	Cs (ppb)
GAS S1	2270	48046	190311	27602	157665	7116	14.7	48480
GAS S2	3805	23768	186666	17037	53784	2356	41.3	51200
GAS S3	2073	23269	403800	27226	93605	8284	116	52924
GAS S4	3464	70849	167013	30965	44916	3266	266	31649
GAS S5	2928	33132	433457	13630	102205	4582	213	46935
GAS S6	2309	31099	400976	34673	282094	11746	675	51878
GAS S7	1636	34249	480793	30825	211188	18251	215	52452
GAS S8	1512	132552	742087	17003	117766	12810	404	50308
GAS S9	32759	79384	212162	21089	11339	1144	3812	23013
GAS S10	2796	53007	760047	24357	75582	14298	156	51350
GAS S11	4746	84649	536508	18092	85233	5800	2834	53803
GAS S12	55513	73555	167124	221142	16064	1685	1030	20183
HEX S1	34620	21657	82987	25819	65761	3400	3278	14842
HEX S2	86072	43666	127517	19419	101094	5156	809	30084
HEX S3	1193	11209	330654	11541	184684	6744	74.2	42354
ARP S1	54362	39098	57707	10532	90850	4833	576	14824
ARP S2	23432	26222	201535	21041	95859	5575	899	21968
ARP S3	14431	7938	9215	25641	3079	97.1	344	1527
ERI S1	81977	24008	132609	8456	45516	2702	400	27723
ERI S2	26126	35519	88673	7448	64374	4032	624	24359
MP53	2829	43230	2571	18366	44681	3164	381	2153

Sample	Ba (ppb)	Hf (ppb)	Ta (ppb)	Re (ppb)	Tl (ppb)	Pb (ppb)	Th (ppb)	U (ppb)
GAS S1	190968	4177	472	10.85	416	5090	8132	2336
GAS S2	96804	1673	524	9.82	403	4003	12642	1200
GAS S3	67293	2802	774	8.41	796	4079	15881	1407
GAS S4	89148	1328	233	12.5	728	5621	3246	941
GAS S5	39144	2055	277	8.70	716	3765	8843	1636
GAS S6	89277	6556	838	7.13	904	3573	9573	1075
GAS S7	132284	6554	2053	7.46	838	4550	32501	4597
GAS S8	111091	3435	1302	9.62	974	3879	21242	4684
GAS S9	32367	304	63.3	6.88	977	22238	944	337
GAS S10	218920	2668	1306	11.5	1627	6126	24601	6002
GAS S11	155171	2259	700	23.69	1419	21995	7911	2507
GAS S12	50291	350	83.3	6.88	3157	41653	1156	330
HEX S1	65112	1702	407	28.6	1636	30830	5994	1336
HEX S2	162232	2699	476	9.60	318	7859	3690	956
HEX S3	183304	5053	518	4.34	470	2601	9301	1634
ARP S1	60646	2549	504	8.45	199	5126	6311	1509
ARP S2	380168	2803	607	6.04	322	5444	10218	2827
ARP S3	30508	105	30.1	4.92	185	9044	177	62.7
ERI S1	214911	1287	256	6.89	461	10897	4535	1408
ERI S2	113909	1895	449	6.47	248	3821	6451	1734
MP53	12464	1400	581	9.54	425	6391	11384	5165

All values are indicated in parts per billion (ppb) abundance. Values below the detection limits are indicated in red. These can have an error of analysis larger than 10% and should be seen as an indicative value. Values above twice the highest calibration are indicated in blue. These can have an error of analysis larger than 10% and should be seen as an indicative value.

XVI: Appendix F: Interpreted XRD Patterns

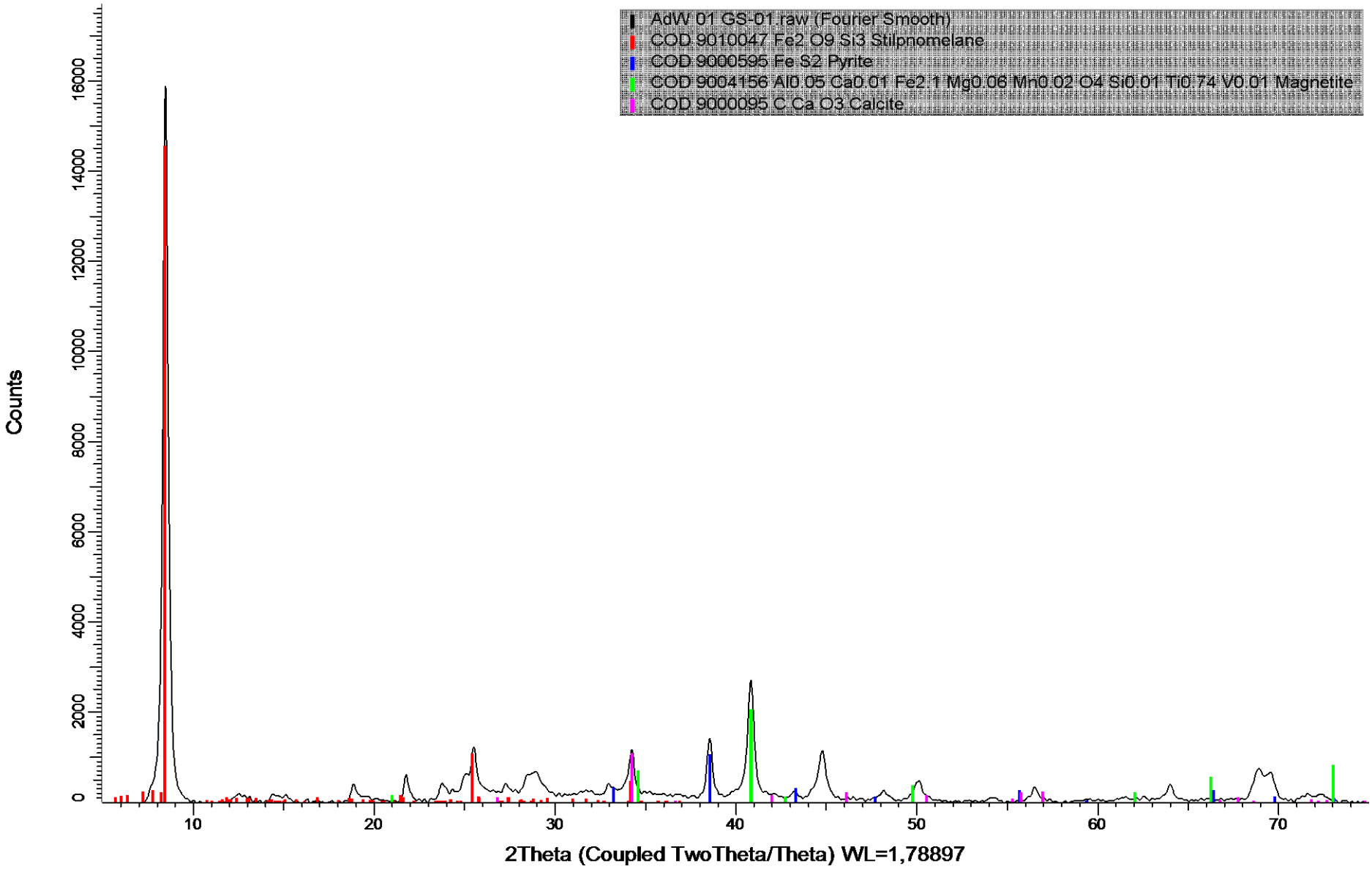

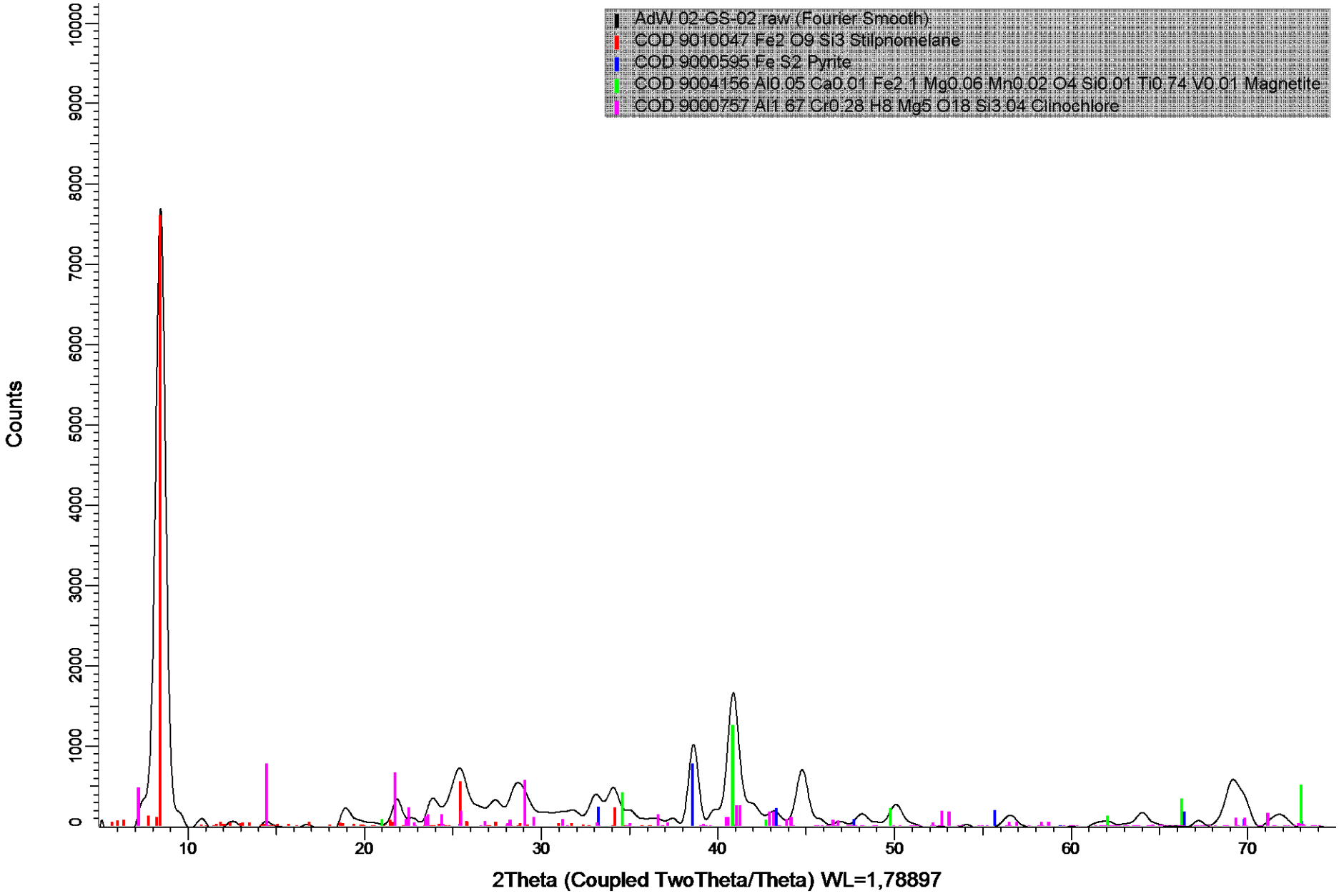
AdW 02-GS-02 raw (Fourier Smooth)
COD 9010047 Fe2 O9 Si3 Stilpnomelane
COD 9000595 Fe S2 Pyrite
COD 9004156 Al0.05 Ca0.01 Fe2.1 Mg0.06 Mn0.02 O4 Si0.01 Ti0.74 V0.01 Magnetite
COD 9000757 Al1.67 Cr0.28 H8 Mg5 O18 Si3.04 Clinochlore
Counts
0
1000
2000
3000
4000
5000
6000
7000
8000
9000
10000
10
20
30
40
50
60
70
2Theta (Coupled TwoTheta/Theta) WL=1,78897

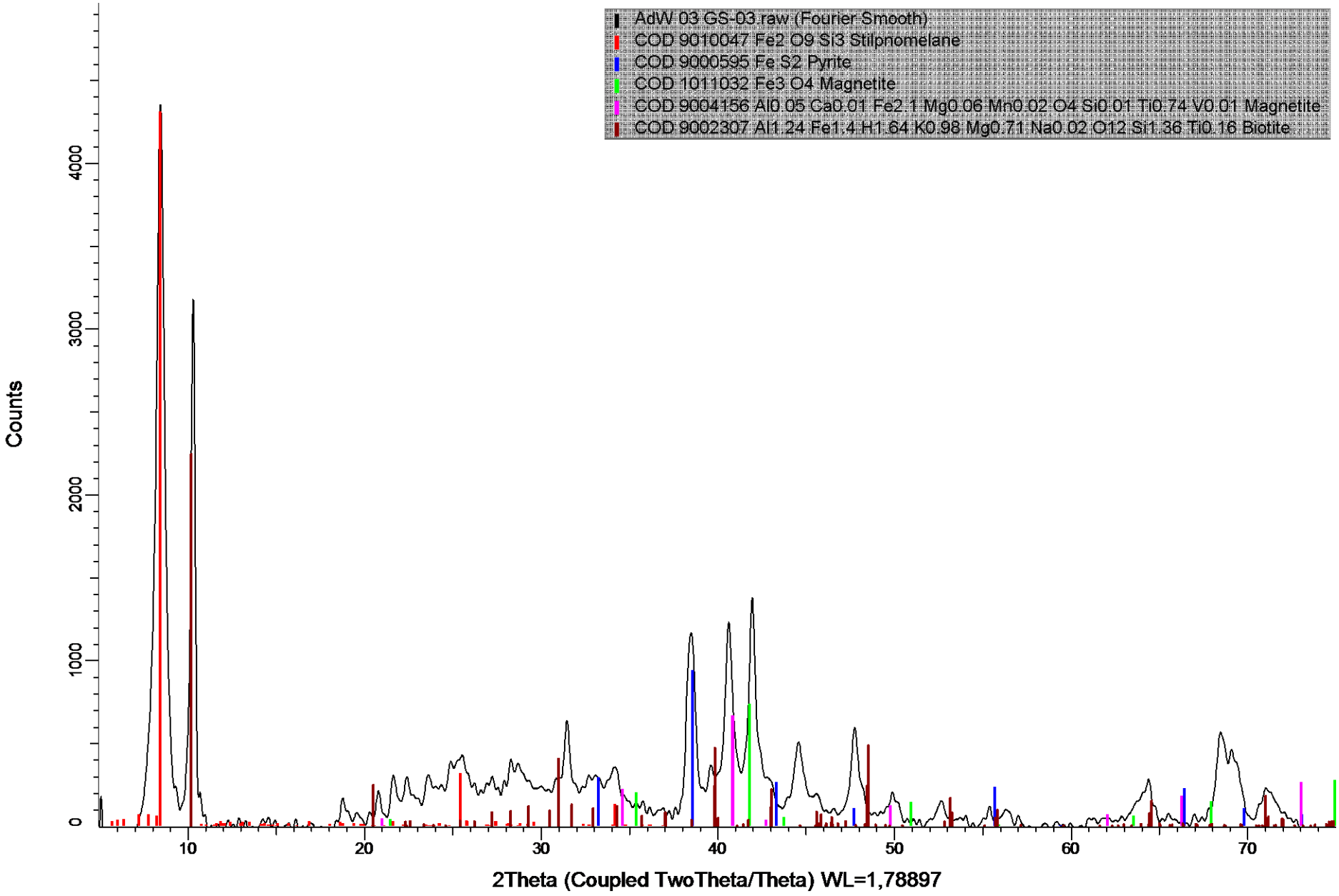
AdW 03 GS-03.raw (Fourier Smooth)
COD 9010047 Fe2 O9 Si3 Stilpnomelane
COD 9000595 Fe S2 Pyrite
COD 1011032 Fe3 O4 Magnetite
COD 9004156 Al0.05 Ca0.01 Fe2.1 Mg0.06 Mn0.02 O4 Si0.01 Ti0.74 V0.01 Magnetite
COD 9002307 Al1.24 Fe1.4 H1.64 K0.98 Mg0.71 Na0.02 O12 Si1.36 Ti0.16 Biotite
Counts
0
1000
2000
3000
4000
10
20
30
40
50
60
70
2Theta (Coupled TwoTheta/Theta) WL=1,78897

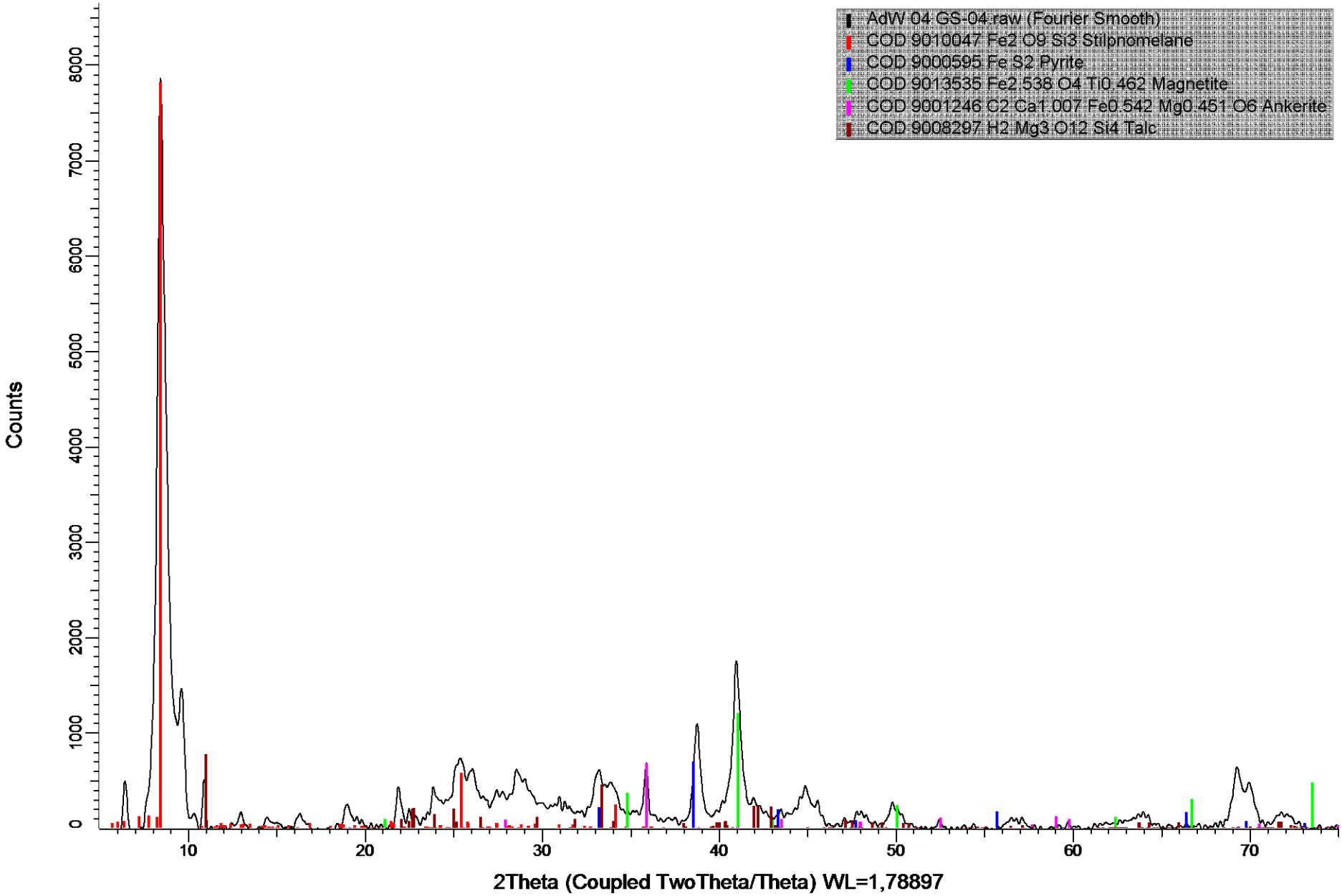
AdW 04 GS-04 raw (Fourier Smooth)
COD 9010047 Fe2 O9 Si3 Stilpnomelane
COD 9000595 Fe S2 Pyrite
COD 9013535 Fe2.538 O4 Ti0.462 Magnetite
COD 9001246 C2 Ca1.007 Fe0.542 Mg0.451 O6 Ankerite
COD 9008297 H2 Mg3 O12 Si4 Talc
Counts
0
1000
2000
3000
4000
5000
6000
7000
8000
10
20
30
40
50
60
70
2Theta (Coupled TwoTheta/Theta) WL=1,78897

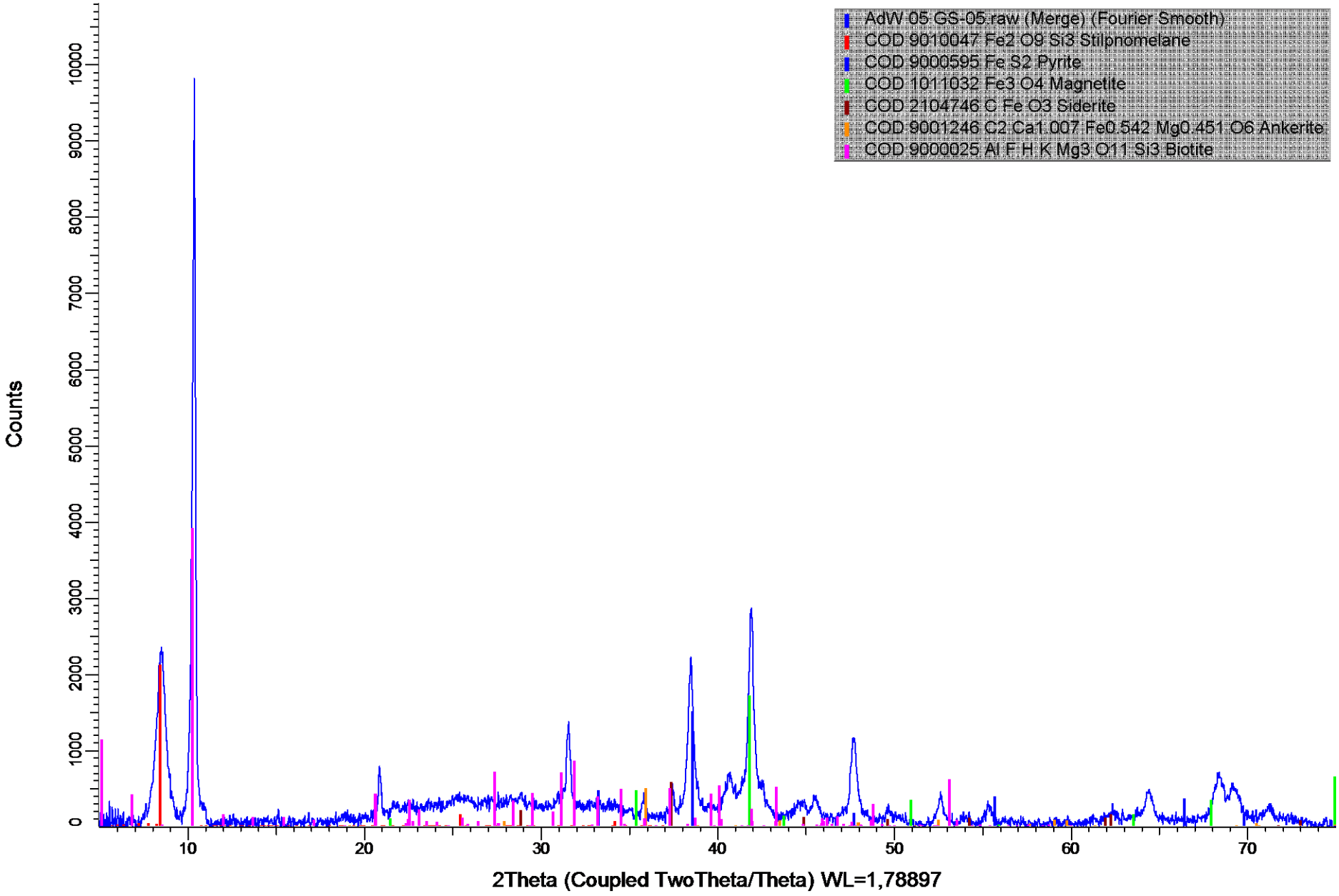
AdW 05 GS-05 raw (Merge) (Fourier Smooth)
COD 9010047 Fe2 O9 Si3 Stilpnomelane
COD 9000595 Fe S2 Pyrite
COD 1011032 Fe3 O4 Magnetite
COD 2104746 C Fe O3 Siderite
COD 9001246 C2 Ca1.007 Fe0.542 Mg0.451 O6 Ankerite
COD 9000025 Al F H K Mg3 O11 Si3 Biotite
Counts
0
1000
2000
3000
4000
5000
6000
7000
8000
9000
10000
10
20
30
40
50
60
70
2Theta (Coupled TwoTheta/Theta) WL=1,78897

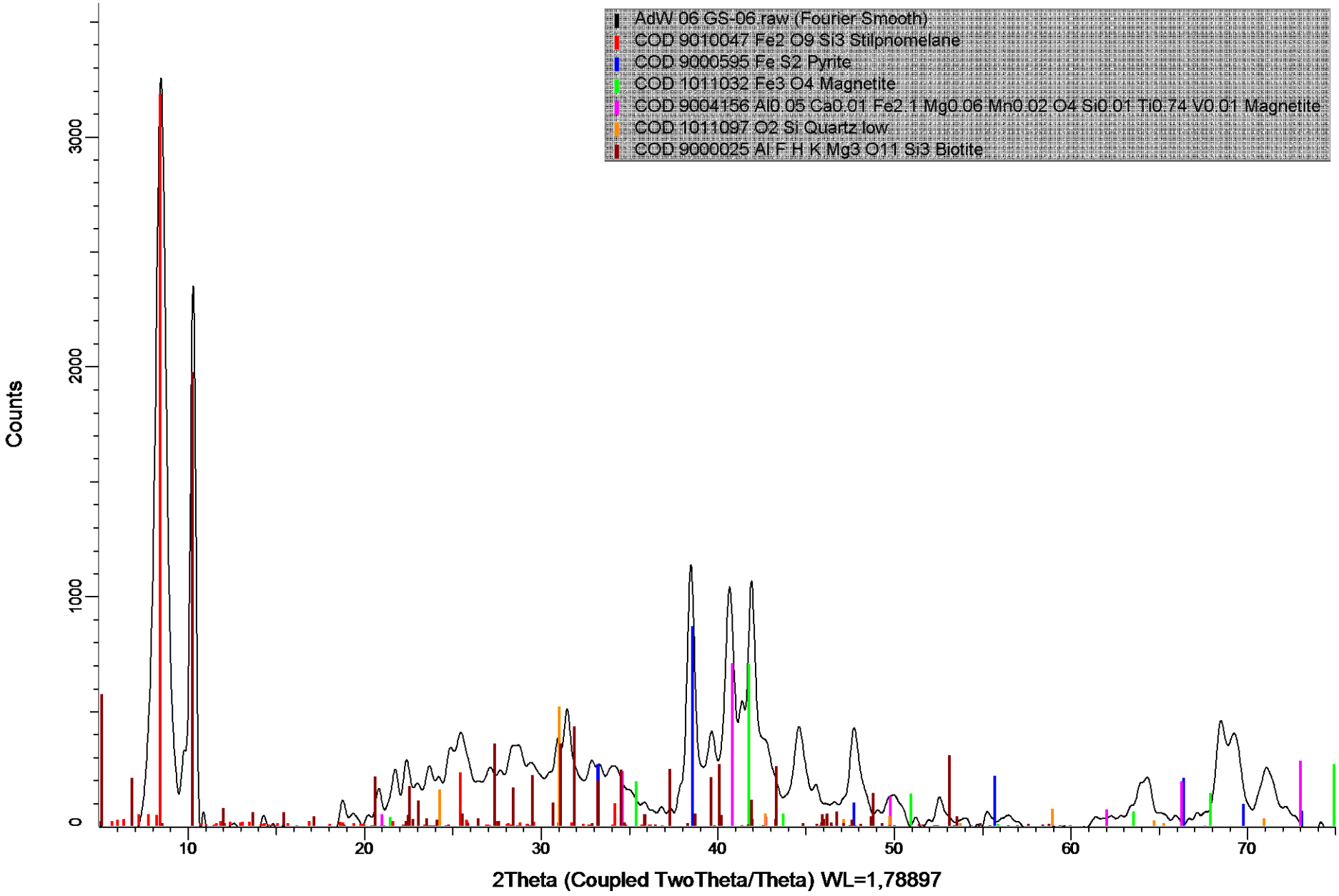
AdW 06 GS-06.raw (Fourier Smooth)
COD 9010047 Fe2 O9 Si3 Stilpnomelane
COD 9000595 Fe S2 Pyrite
COD 1011032 Fe3 O4 Magnetite
COD 9004156 Al0.05 Ca0.01 Fe2.1 Mg0.06 Mn0.02 O4 Si0.01 Ti0.74 V0.01 Magnetite
COD 1011097 O2 Si Quartz low
COD 9000025 Al F H K Mg3 O11 Si3 Biotite
Counts
0
1000
2000
3000
10
20
30
40
50
60
70
2Theta (Coupled TwoTheta/Theta) WL=1,78897

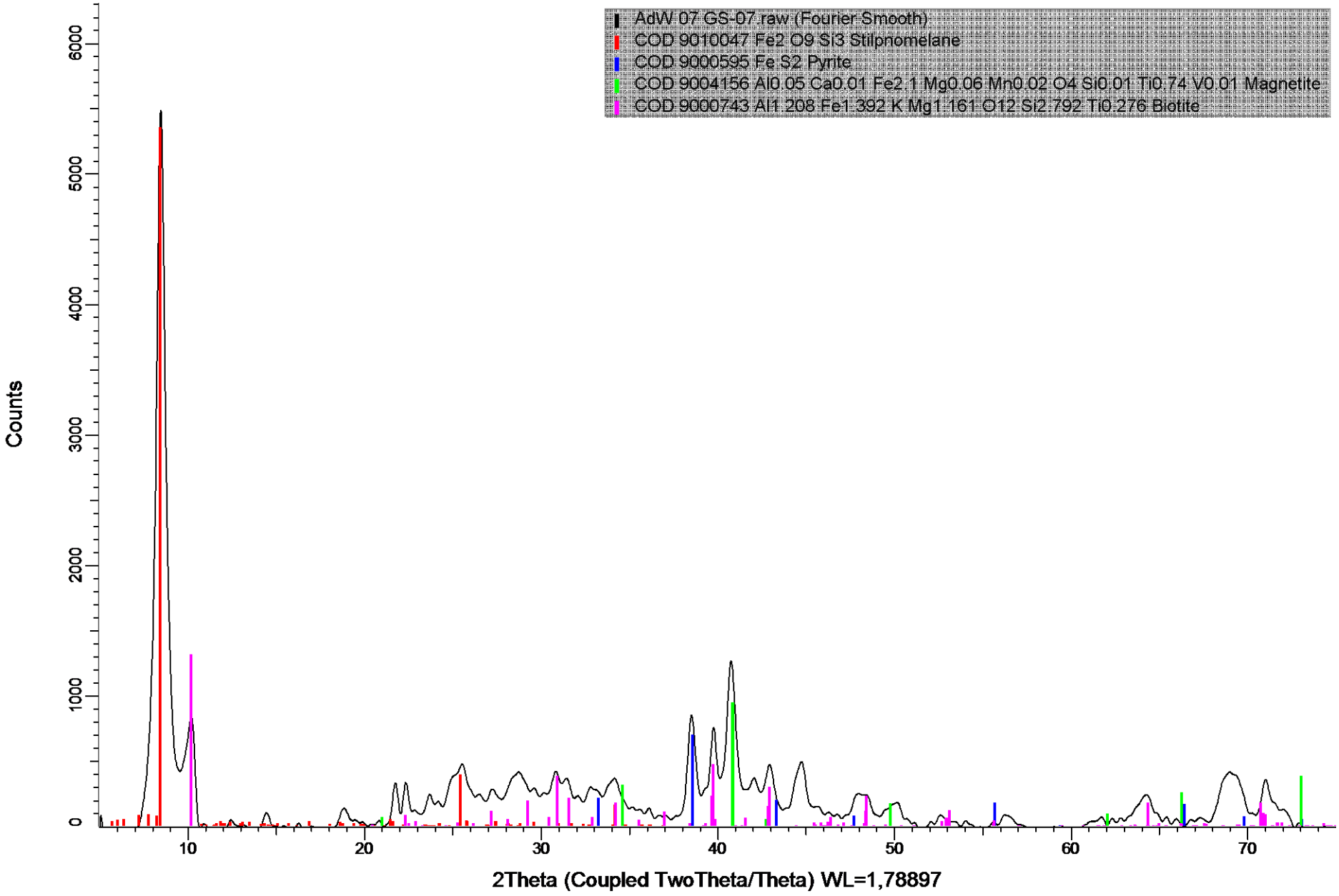
AdW 07 GS-07.raw (Fourier Smooth)
COD 9010047 Fe2 O9 Si3 Stilpnomelane
COD 9000595 Fe S2 Pyrite
COD 9004156 Al0.05 Ca0.01 Fe2.1 Mg0.06 Mn0.02 O4 Si0.01 Ti0.74 V0.01 Magnetite
COD 9000743 Al1.208 Fe1.392 K Mg1.161 O12 Si2.792 Ti0.276 Biotite
Counts
0
1000
2000
3000
4000
5000
6000
10
20
30
40
50
60
70
2Theta (Coupled TwoTheta/Theta) WL=1,78897

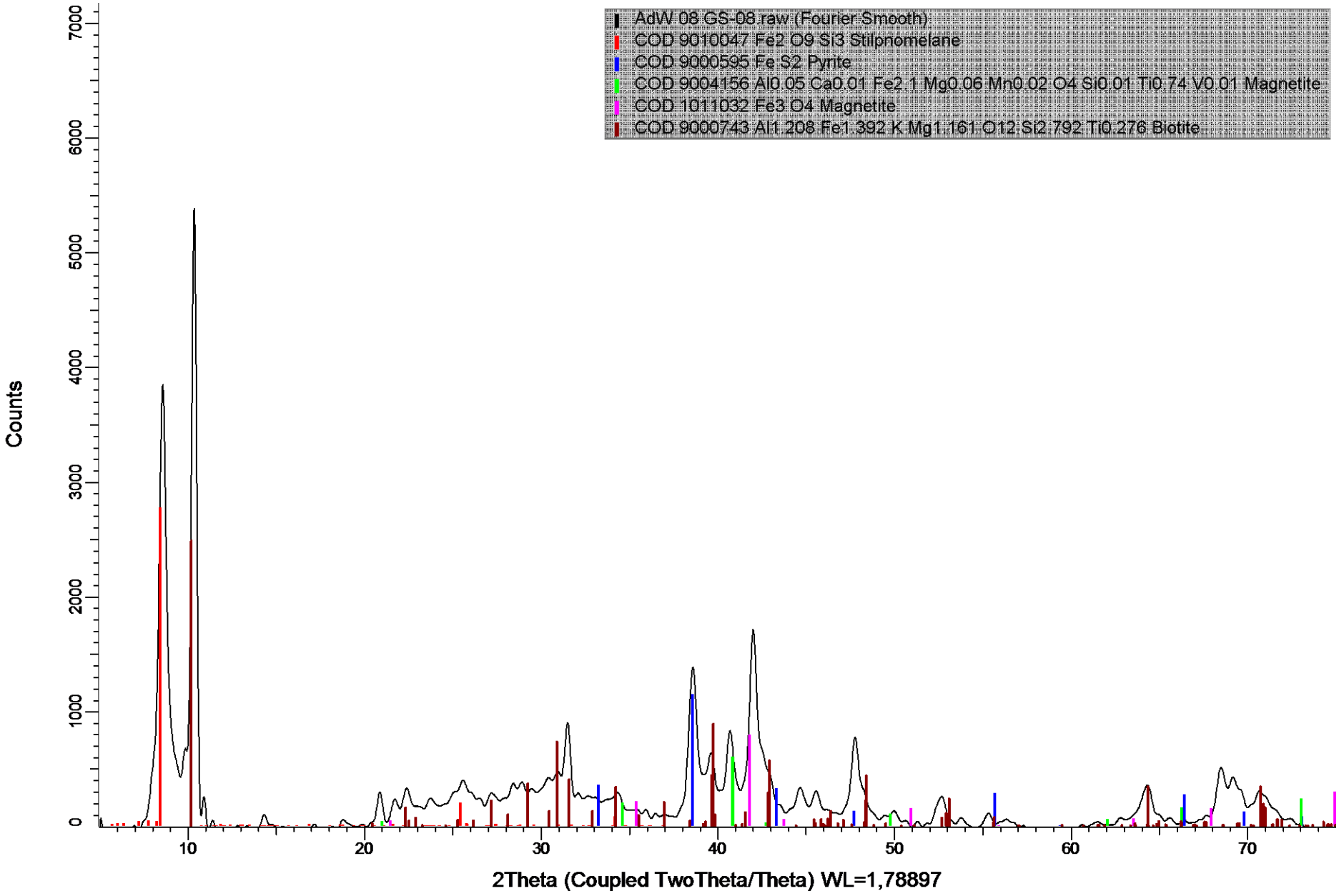
AdW 08 GS-08.raw (Fourier Smooth)
COD 9010047 Fe2 O9 Si3 Stilpnomelane
COD 9000595 Fe S2 Pyrite
COD 9004156 Al0.05 Ca0.01 Fe2.1 Mg0.06 Mn0.02 O4 Si0.01 Ti0.74 V0.01 Magnetite
COD 1011032 Fe3 O4 Magnetite
COD 9000743 Al1.208 Fe1.392 K Mg1.161 O12 Si2.792 Ti0.276 Biotite
Counts
0
1000
2000
3000
4000
5000
6000
7000
10
20
30
40
50
60
70
2Theta (Coupled TwoTheta/Theta) WL=1,78897

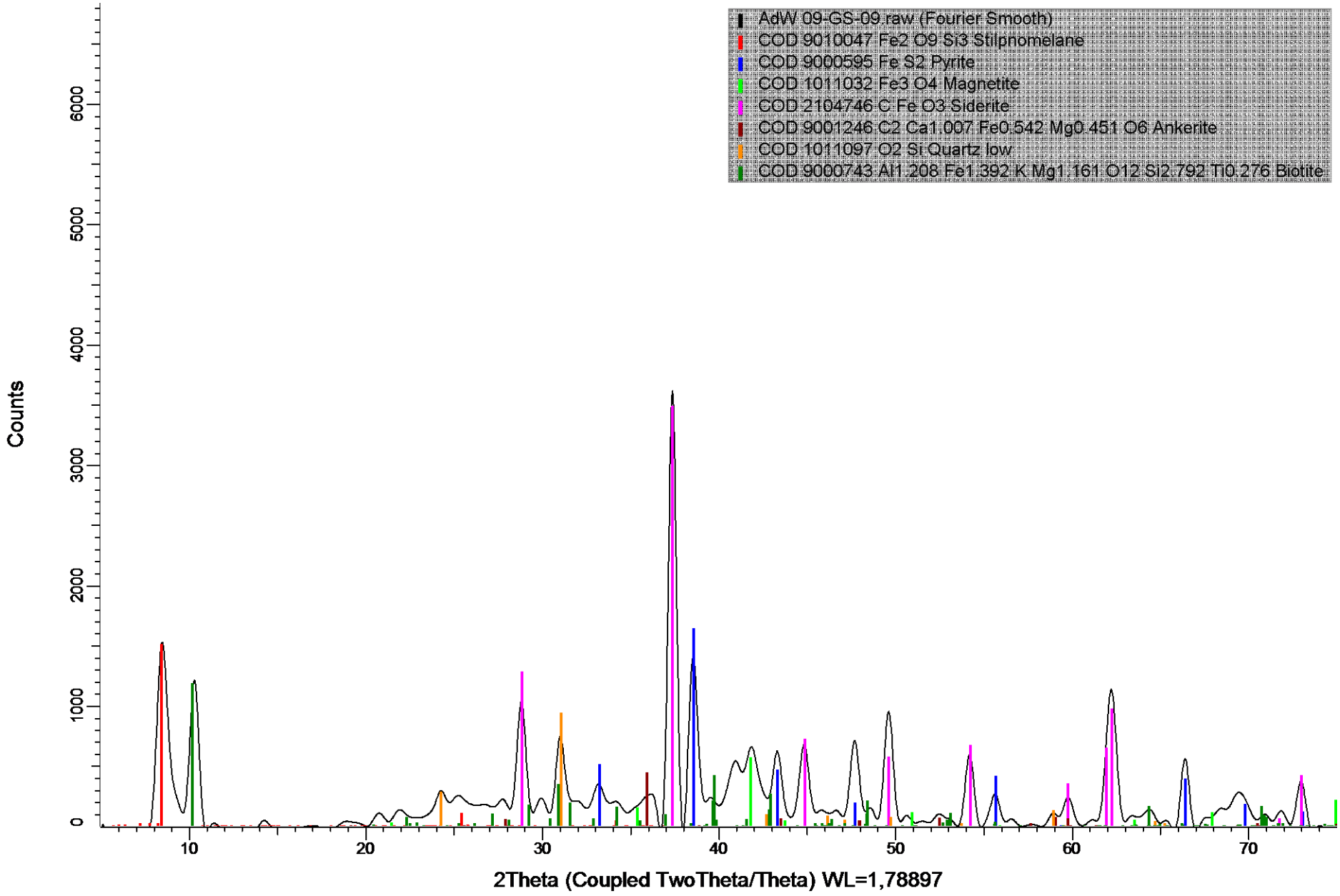
AdW 09-GS-09 raw (Fourier Smooth)
COD 9010047 Fe2 O9 Si3 Stilpnomelane
COD 9000595 Fe S2 Pyrite
COD 1011032 Fe3 O4 Magnetite
COD 2104746 C Fe O3 Siderite
COD 9001246 C2 Ca1.007 Fe0.542 Mg0.451 O6 Ankerite
COD 1011097 O2 Si Quartz low
COD 9000743 Al1.208 Fe1.392 K Mg1.161 O12 Si2.792 Ti0.276 Biotite
Counts
0
1000
2000
3000
4000
5000
6000
10
20
30
40
50
60
70
2Theta (Coupled TwoTheta/Theta) WL=1,78897

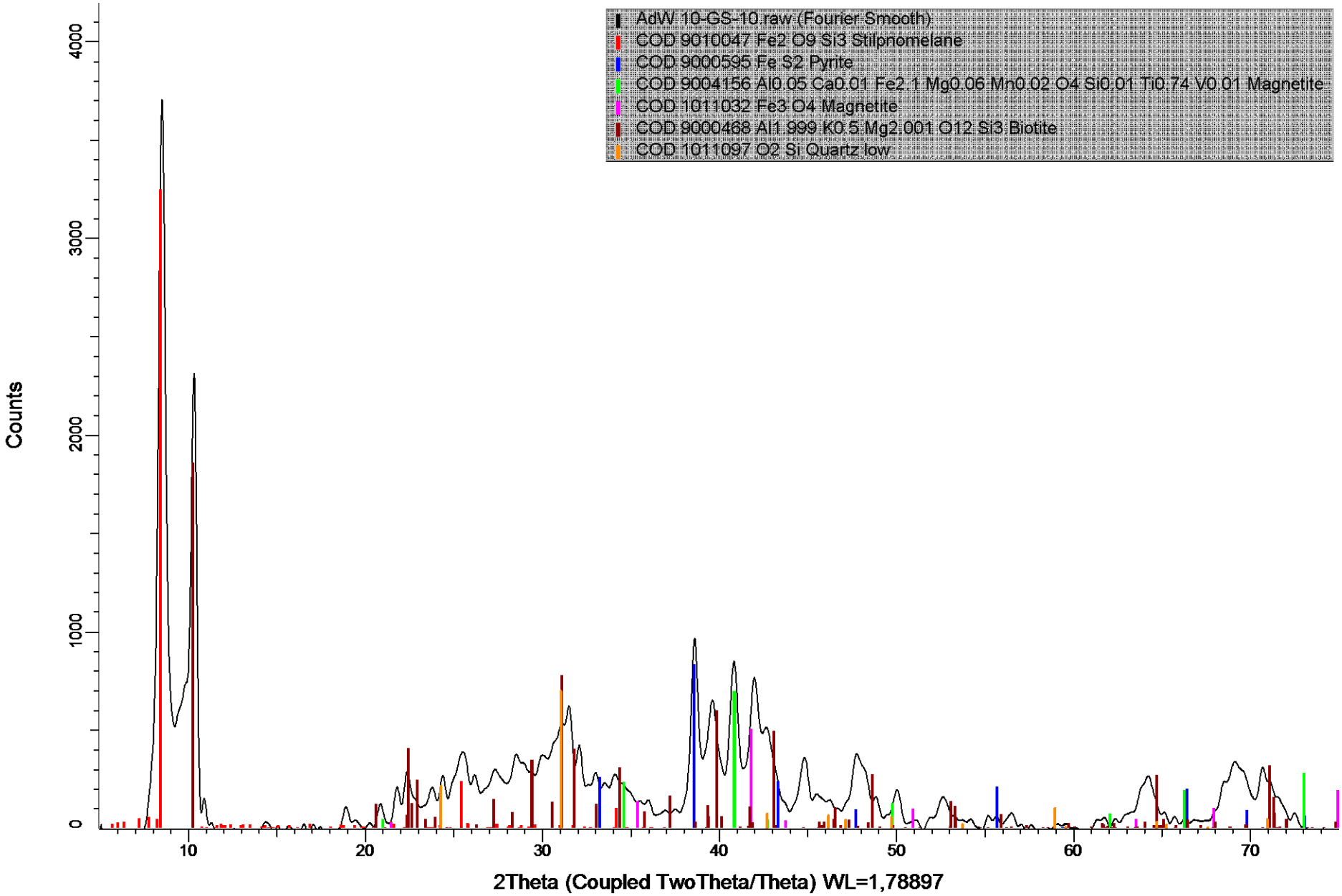
AdW 10-GS-10.raw (Fourier Smooth)
COD 9010047 Fe2 O9 Si3 Stilpnomelane
COD 9000595 Fe S2 Pyrite
COD 9004156 Al0.05 Ca0.01 Fe2.1 Mg0.06 Mn0.02 O4 Si0.01 Ti0.74 V0.01 Magnetite
COD 1011032 Fe3 O4 Magnetite
COD 9000468 Al1.999 K0.5 Mg2.001 O12 Si3 Biotite
COD 1011097 O2 Si Quartz low
Counts
0
1000
2000
3000
4000
10
20
30
40
50
60
70
2Theta (Coupled TwoTheta/Theta) WL=1,78897

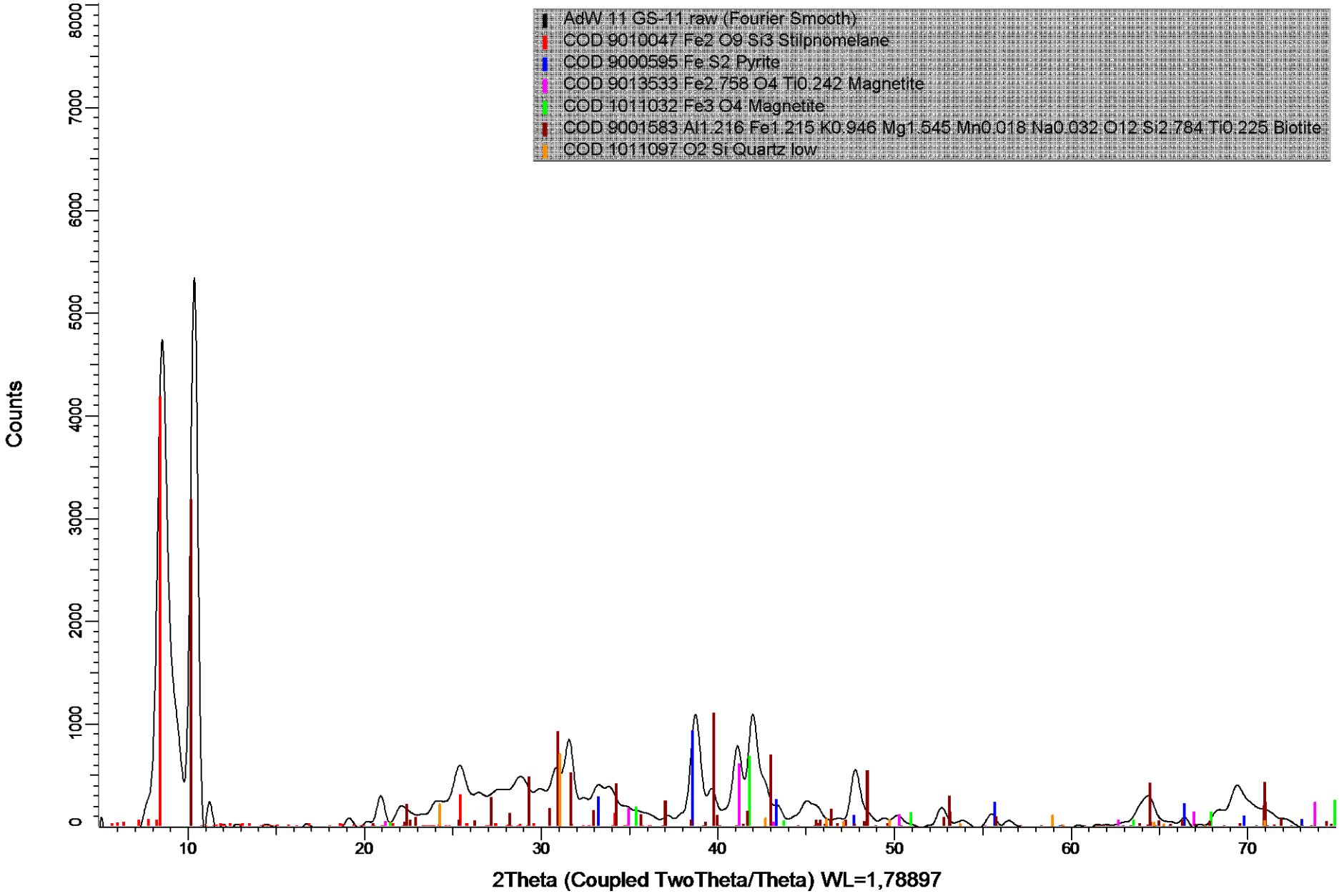
AdW 11 GS-11 raw (Fourier Smooth)
COD 9010047 Fe2 O9 Si3 Stilpnomelane
COD 9000595 Fe S2 Pyrite
COD 9013533 Fe2.758 O4 Ti0.242 Magnetite
COD 1011032 Fe3 O4 Magnetite
COD 9001583 Al1.216 Fe1.215 K0.946 Mg1.545 Mn0.018 Na0.032 O12 Si2.784 Ti0.225 Biotite
COD 1011097 O2 Si Quartz low
Counts
0
1000
2000
3000
4000
5000
6000
7000
8000
10
20
30
40
50
60
70
2Theta (Coupled TwoTheta/Theta) WL=1,78897

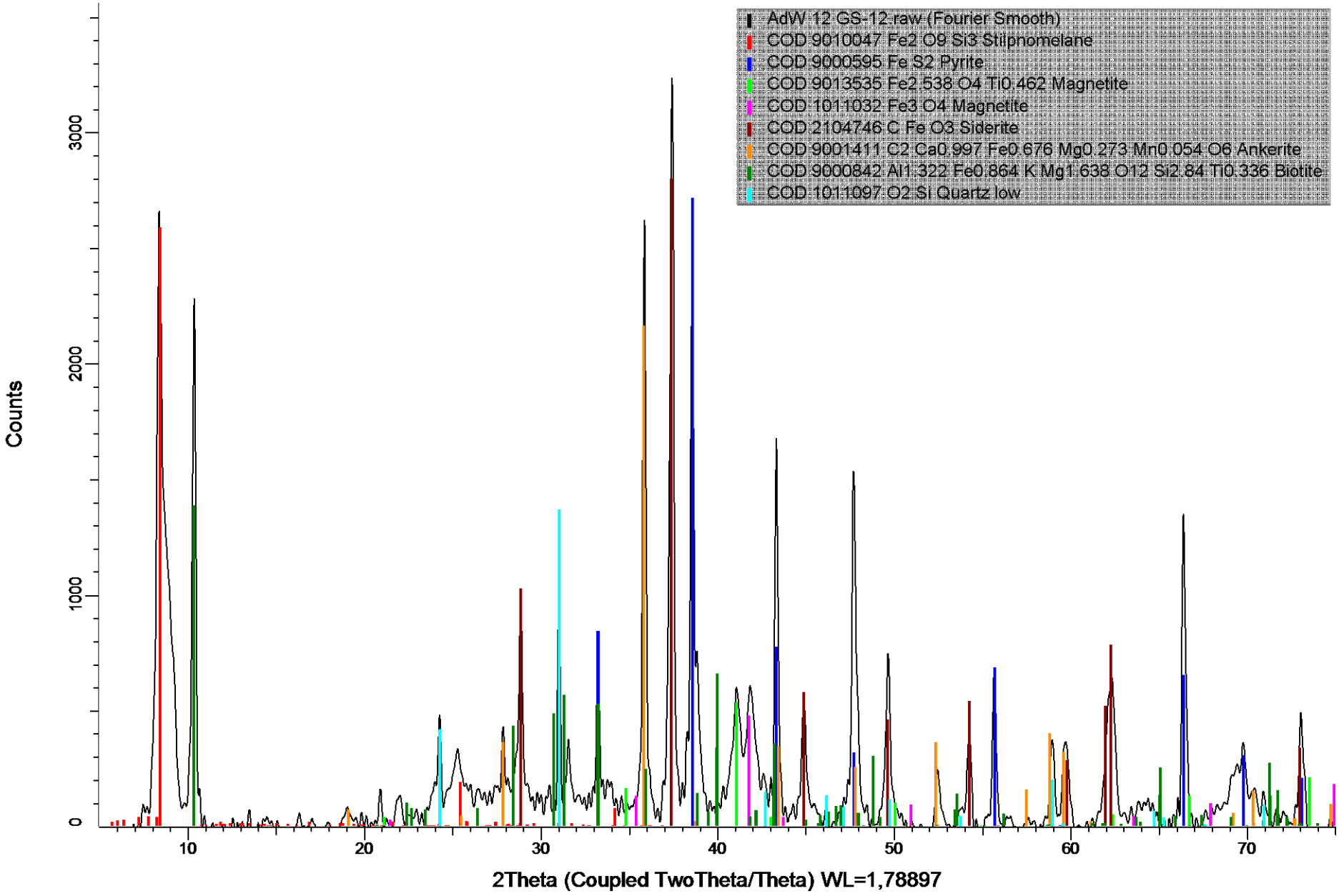
AdW 12 GS-12 raw (Fourier Smooth)
COD 9010047 Fe2 O9 Si3 Stilpnomelane
COD 9000595 Fe S2 Pyrite
COD 9013535 Fe2.538 O4 Ti0.462 Magnetite
COD 1011032 Fe3 O4 Magnetite
COD 2104746 C Fe O3 Siderite
COD 9001411 C2 Ca0.997 Fe0.676 Mg0.273 Mn0.054 O6 Ankerite
COD 9000842 Al1.322 Fe0.864 K Mg1.638 O12 Si2.84 Ti0.336 Biotite
COD 1011097 O2 Si Quartz low
Counts
0
1000
2000
3000
10
20
30
40
50
60
70
2Theta (Coupled TwoTheta/Theta) WL=1,78897

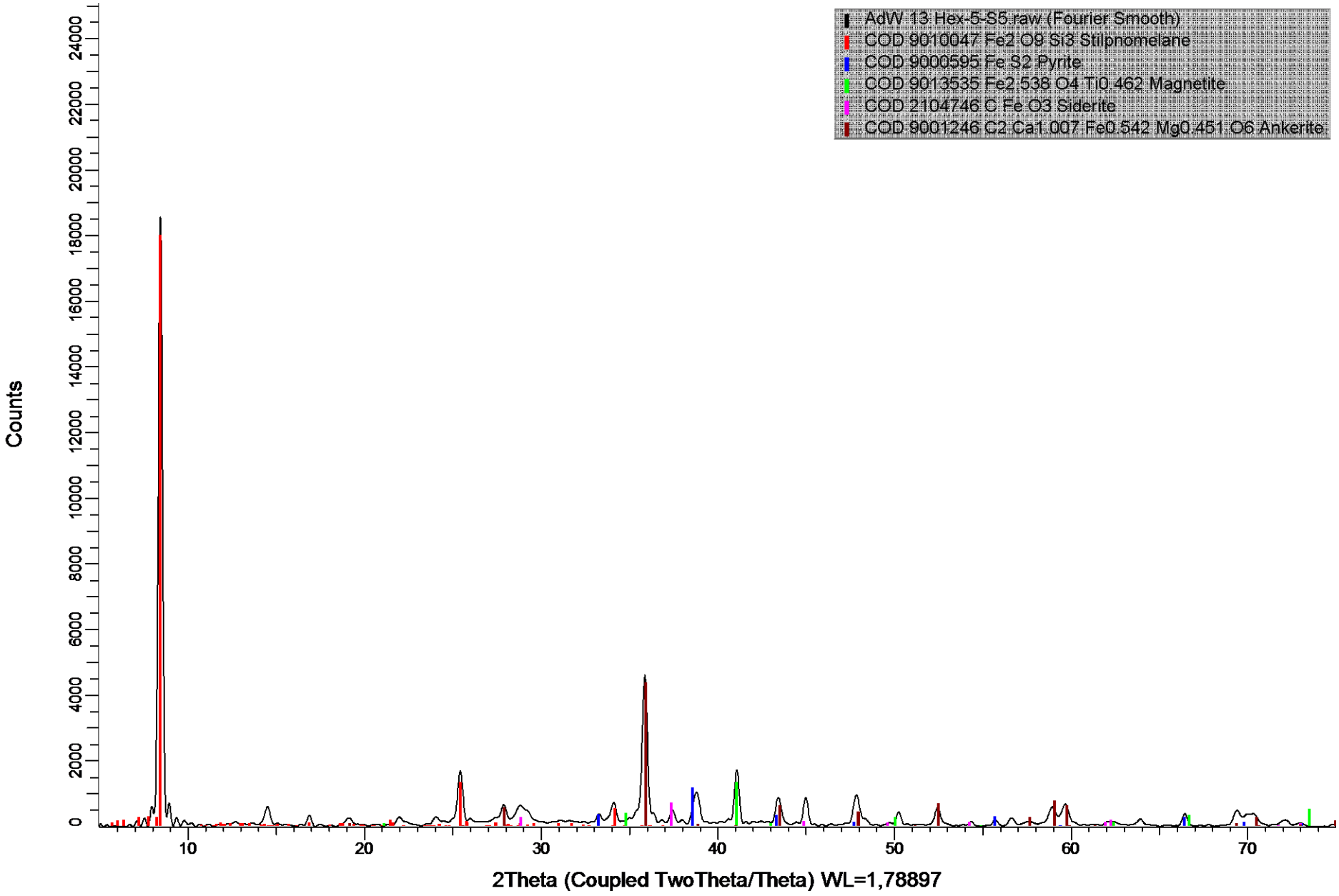
AdW-13-Hex-5-S5.raw (Fourier Smooth)
COD 9010047 Fe2 O9 Si3 Stilpnomelane
COD 9000595 Fe S2 Pyrite
COD 9013535 Fe2.538 O4 Ti0.462 Magnetite
COD 2104746 C Fe O3 Siderite
COD 9001246 C2 Ca1.007 Fe0.542 Mg0.451 O6 Ankerite
Counts
0
2000
4000
6000
8000
10000
12000
14000
16000
18000
20000
22000
24000
10
20
30
40
50
60
70
2Theta (Coupled TwoTheta/Theta) WL=1,78897

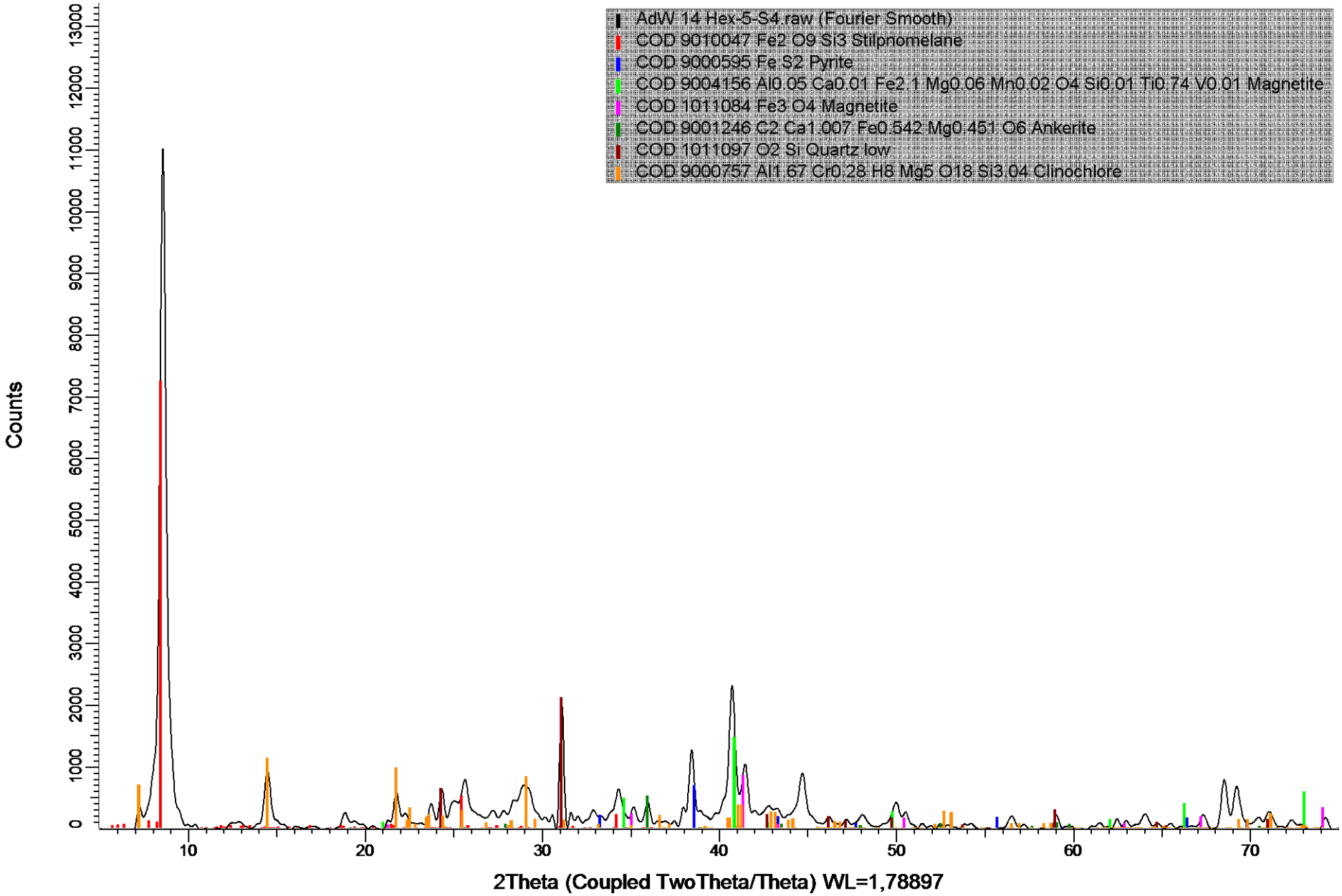
AdW 14 Hex-5-S4.raw (Fourier Smooth)
COD 9010047 Fe2 O9 Si3 Stilpnomelane
COD 9000595 Fe S2 Pyrite
COD 9004156 Al0.05 Ca0.01 Fe2.1 Mg0.06 Mn0.02 O4 Si0.01 Ti0.74 V0.01 Magnetite
COD 1011084 Fe3 O4 Magnetite
COD 9001246 C2 Ca1.007 Fe0.542 Mg0.451 O6 Ankerite
COD 1011097 O2 Si Quartz low
COD 9000757 Al1.67 Cr0.28 H8 Mg5 O18 Si3.04 Clinochlore
Counts
0
1000
2000
3000
4000
5000
6000
7000
8000
9000
10000
11000
12000
13000
10
20
30
40
50
60
70
2Theta (Coupled TwoTheta/Theta) WL=1,78897

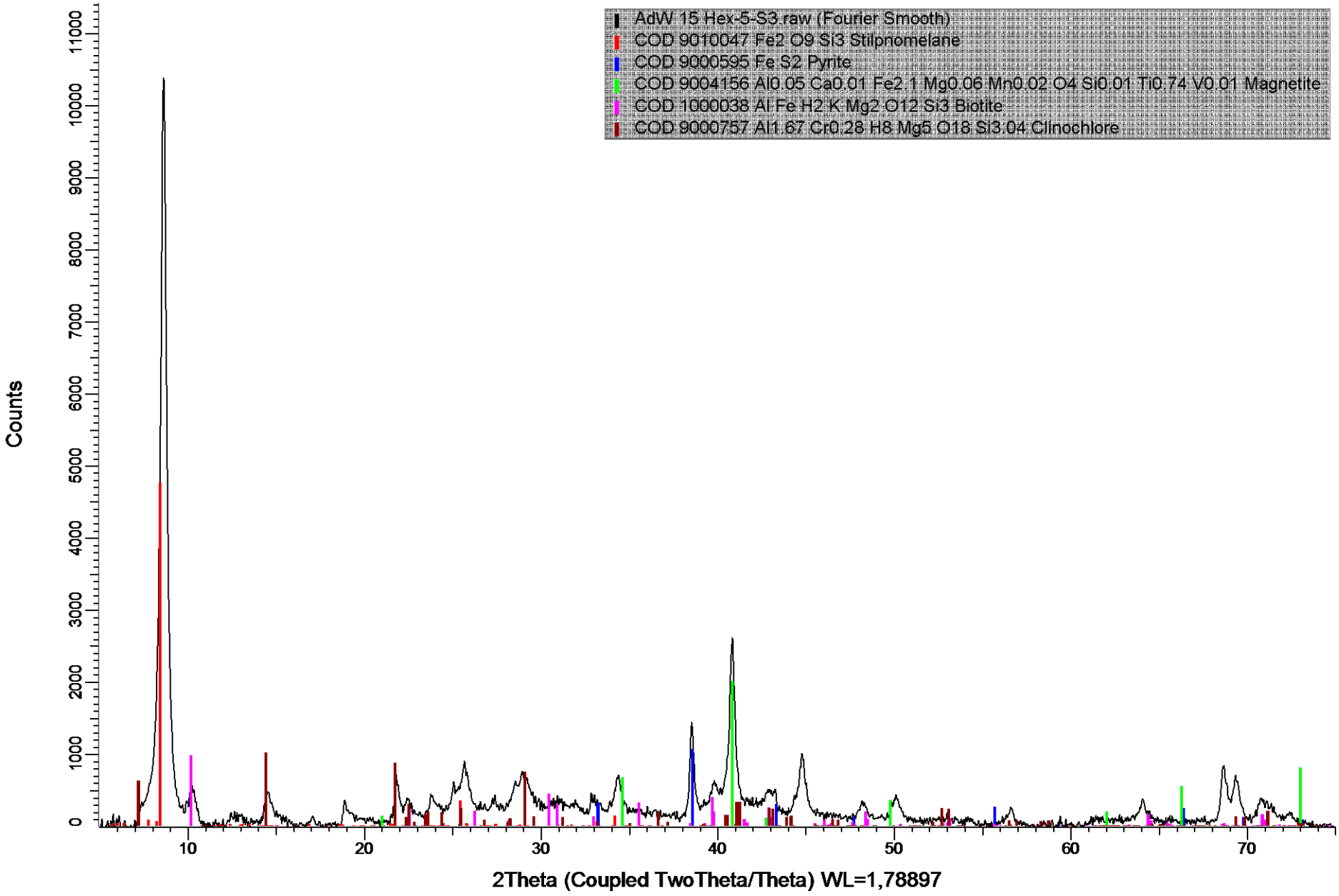
AdW 15 Hex-5-S3 raw (Fourier Smooth)
COD 9010047 Fe2 O9 Si3 Stilpnomelane
COD 9000595 Fe S2 Pyrite
COD 9004156 Al0.05 Ca0.01 Fe2.1 Mg0.06 Mn0.02 O4 Si0.01 Ti0.74 V0.01 Magnetite
COD 1000038 Al Fe H2 K Mg2 O12 Si3 Biotite
COD 9000757 Al1.67 Cr0.28 H8 Mg5 O18 Si3.04 Clinochlore
Counts
0
1000
2000
3000
4000
5000
6000
7000
8000
9000
10000
11000
10
20
30
40
50
60
70
2Theta (Coupled TwoTheta/Theta) WL=1,78897

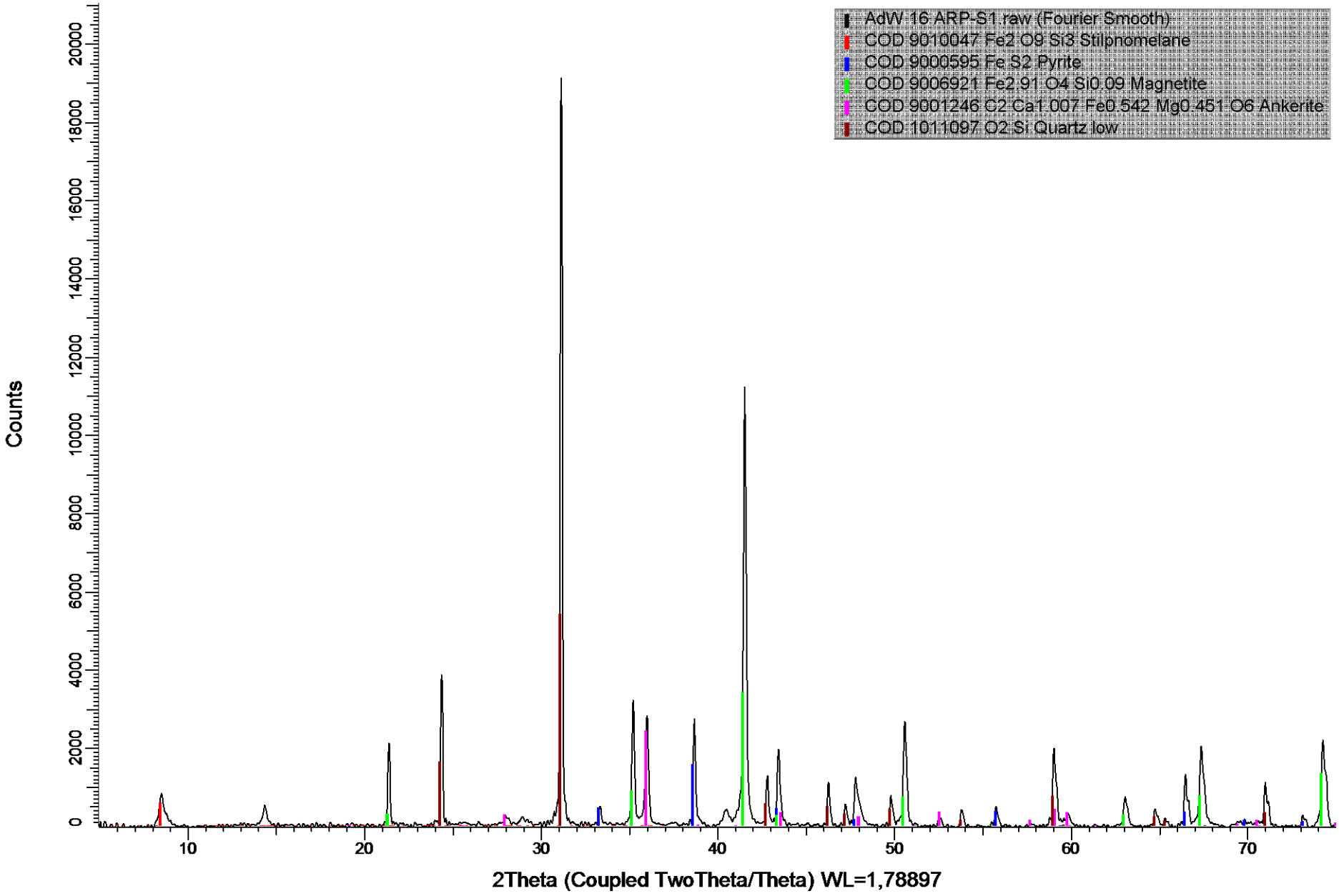
AdW 16 ARP-S1 raw (Fourier Smooth)
COD 9010047 Fe2 O9 Si3 Stilpnomelane
COD 9000595 Fe S2 Pyrite
COD 9006921 Fe2.91 O4 Si0.09 Magnetite
COD 9001246 C2 Ca1.007 Fe0.542 Mg0.451 O6 Ankerite
COD 1011097 O2 Si Quartz low
Counts
0
2000
4000
6000
8000
10000
12000
14000
16000
18000
20000
10
20
30
40
50
60
70
2Theta (Coupled TwoTheta/Theta) WL=1,78897

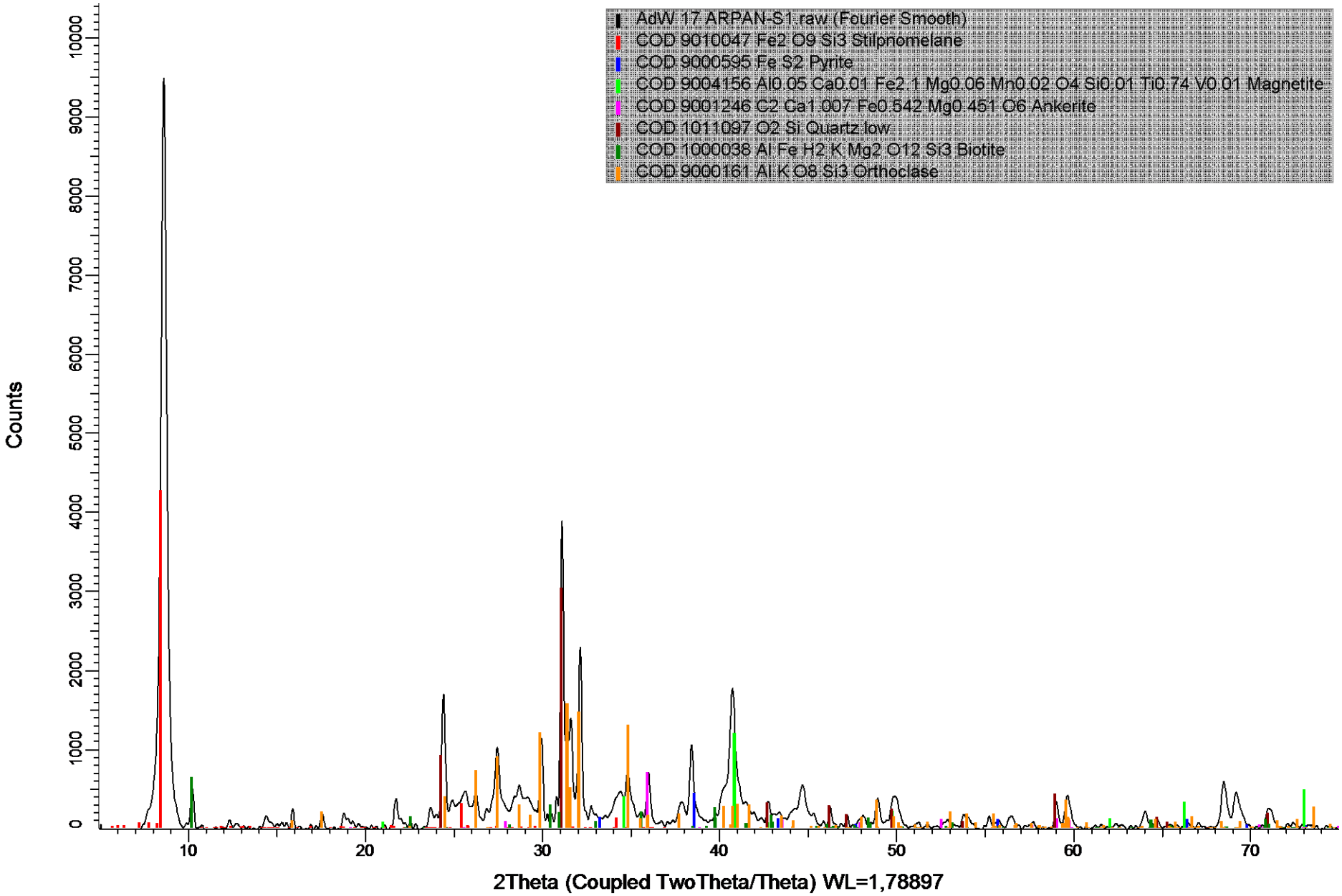
AdW 17 ARPAN-S1 raw (Fourier Smooth)
COD 9010047 Fe2 O9 Si3 Stilpnomelane
COD 9000595 Fe S2 Pyrite
COD 9004156 Al0.05 Ca0.01 Fe2.1 Mg0.06 Mn0.02 O4 Si0.01 Ti0.74 V0.01 Magnetite
COD 9001246 C2 Ca1.007 Fe0.542 Mg0.451 O6 Ankerite
COD 1011097 O2 Si Quartz low
COD 1000038 Al Fe H2 K Mg2 O12 Si3 Biotite
COD 9000161 Al K O8 Si3 Orthoclase
Counts
0
1000
2000
3000
4000
5000
6000
7000
8000
9000
10000
10
20
30
40
50
60
70
2Theta (Coupled TwoTheta/Theta) WL=1,78897

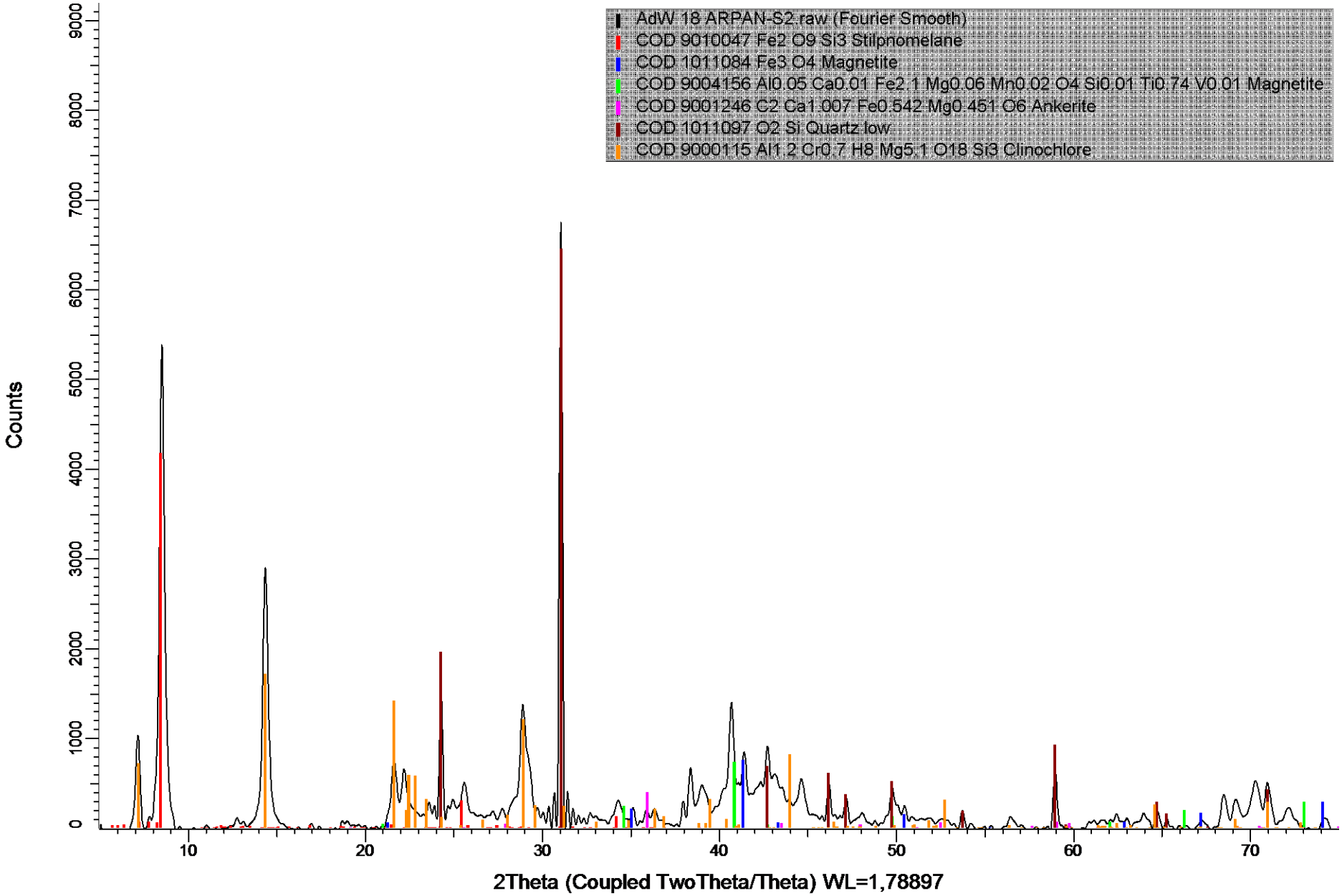
AdW 18 ARPAN-S2.raw (Fourier Smooth)
COD 9010047 Fe2 O9 Si3 Stilpnomelane
COD 1011084 Fe3 O4 Magnetite
COD 9004156 Al0.05 Ca0.01 Fe2.1 Mg0.06 Mn0.02 O4 Si0.01 Ti0.74 V0.01 Magnetite
COD 9001246 C2 Ca1.007 Fe0.542 Mg0.451 O6 Ankerite
COD 1011097 O2 Si Quartz low
COD 9000115 Al1.2 Cr0.7 H8 Mg5.1 O18 Si3 Clinochlore
Counts
0
1000
2000
3000
4000
5000
6000
7000
8000
9000
10
20
30
40
50
60
70
2Theta (Coupled TwoTheta/Theta) WL=1,78897

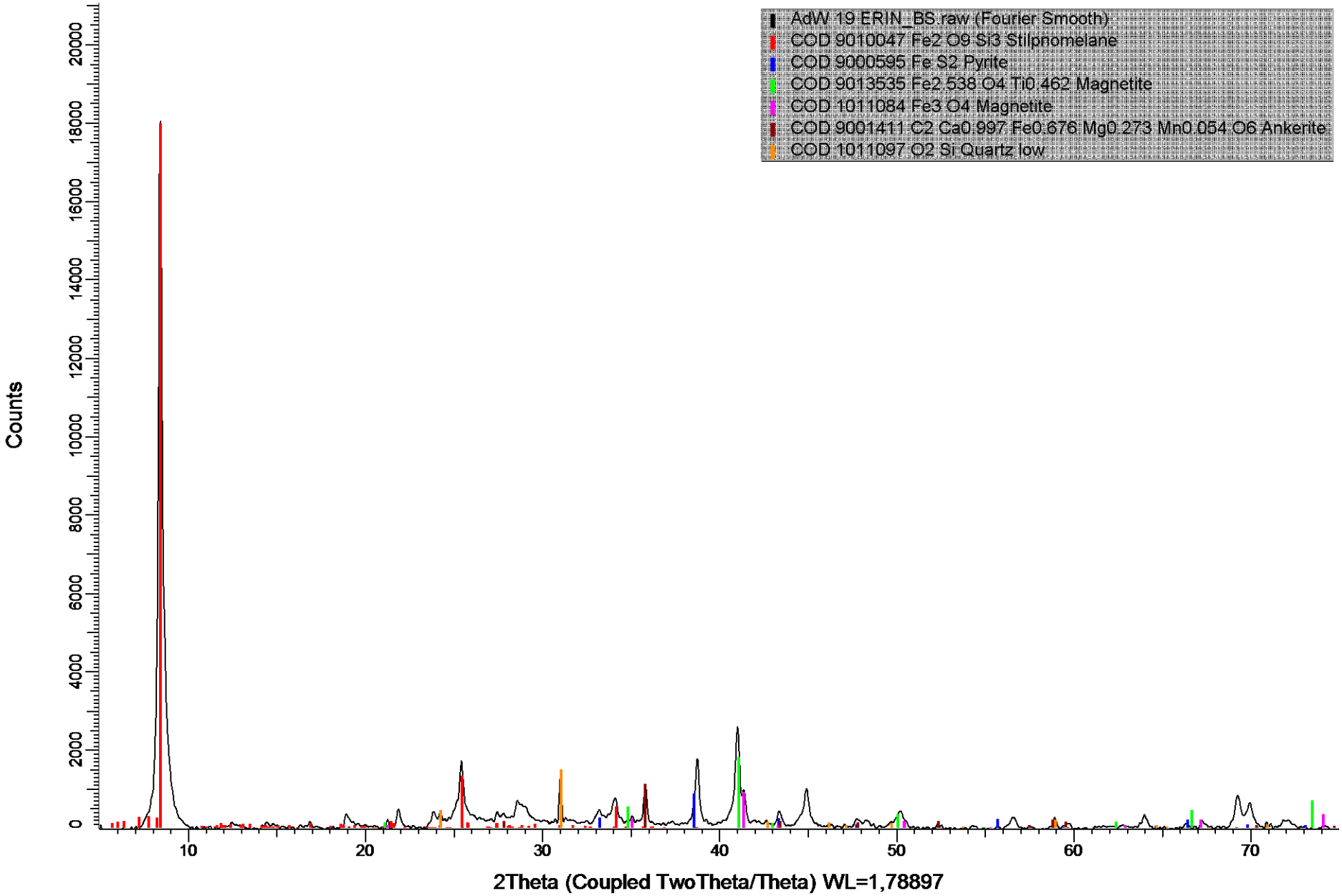
AdW 19 ERIN_BS raw (Fourier Smooth)
COD 9010047 Fe2 O9 Si3 Stilpnomelane
COD 9000595 Fe S2 Pyrite
COD 9013535 Fe2.538 O4 Ti0.462 Magnetite
COD 1011084 Fe3 O4 Magnetite
COD 9001411 C2 Ca0.997 Fe0.676 Mg0.273 Mn0.054 O6 Ankerite
COD 1011097 O2 Si Quartz low
Counts
0
2000
4000
6000
8000
10000
12000
14000
16000
18000
20000
10
20
30
40
50
60
70
2Theta (Coupled TwoTheta/Theta) WL=1,78897

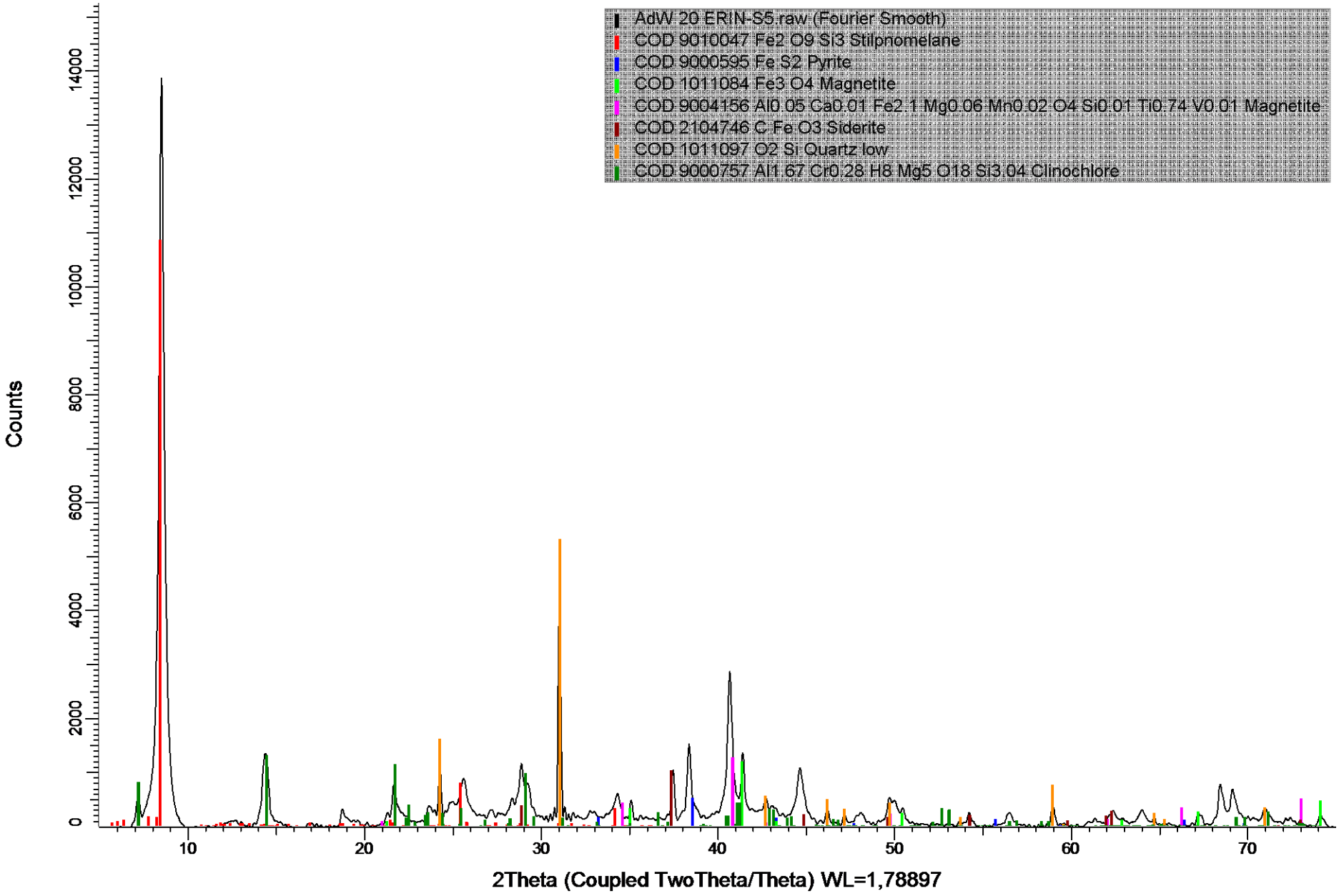
AdW 20 ERIN-S5 raw (Fourier Smooth)
COD 9010047 Fe2 O9 Si3 Stilpnomelane
COD 9000595 Fe S2 Pyrite
COD 1011084 Fe3 O4 Magnetite
COD 9004156 Al0.05 Ca0.01 Fe2.1 Mg0.06 Mn0.02 O4 Si0.01 Ti0.74 V0.01 Magnetite
COD 2104746 C Fe O3 Siderite
COD 1011097 O2 Si Quartz low
COD 9000757 Al1.67 Cr0.28 H8 Mg5 O18 Si3.04 Clinochlore
Counts
0
2000
4000
6000
8000
10000
12000
14000
10
20
30
40
50
60
70
2Theta (Coupled TwoTheta/Theta) WL=1,78897

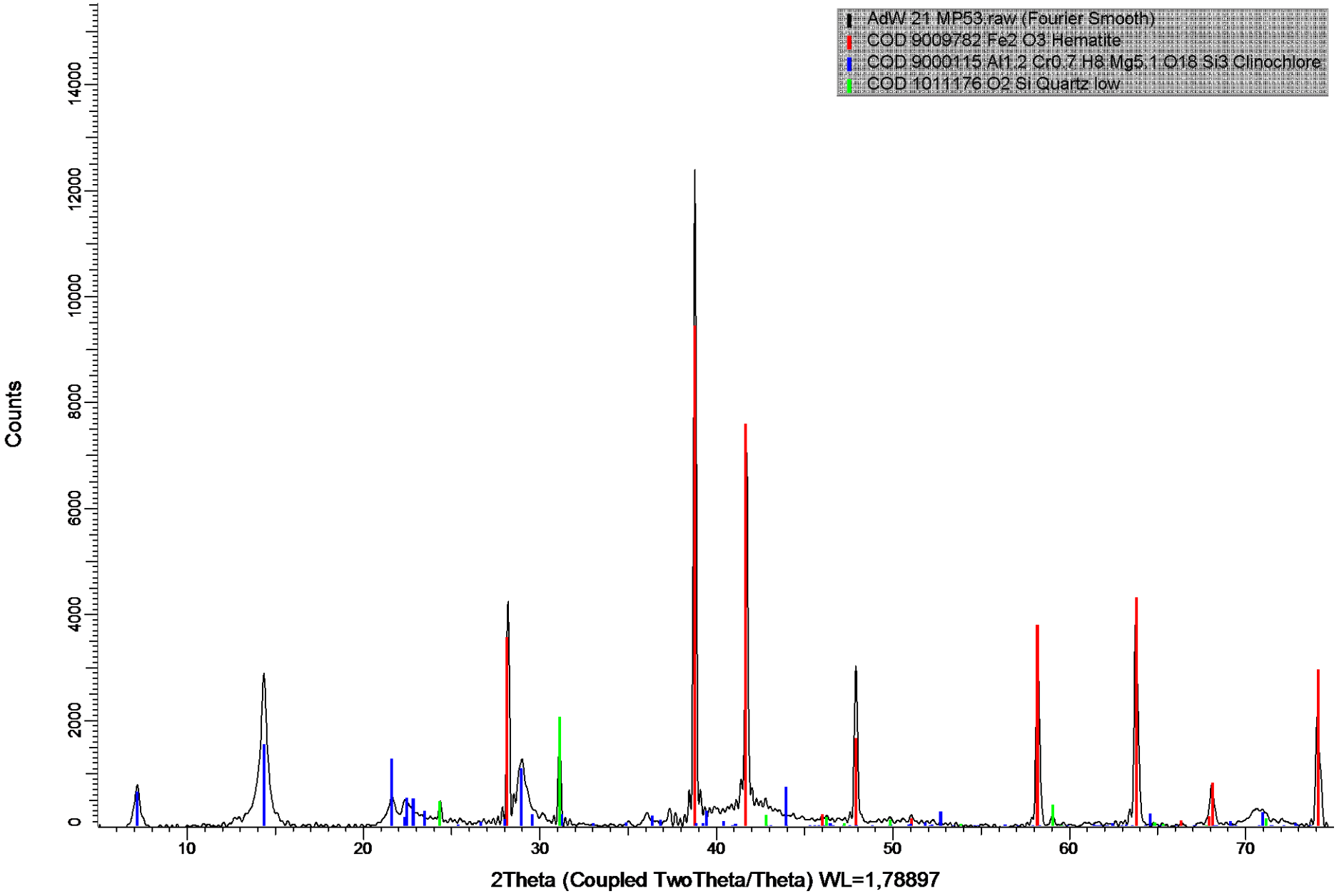
AdW 21 MP53 raw (Fourier Smooth)
COD 9009782 Fe2 O3 Hematite
COD 9000115 Al1.2 Cr0.7 H8 Mg5.1 O18 Si3 Clinochlore
COD 1011176 O2 Si Quartz low
Counts
0
2000
4000
6000
8000
10000
12000
14000
10
20
30
40
50
60
70
2Theta (Coupled TwoTheta/Theta) WL=1,78897

XVII: Appendix G: Complete Sulphur Extraction Protocol

Preface

The following text provides a description of the various extraction techniques for liberating different sulphur phases from different matrices for isotope measurements. This represents an extract from the original publications, and the analytical methods have been adapted/modified/optimized to suit our laboratory requirements.

Extraction of acid-volatile-S (AVS) and chromium-reducible-S (CRS)

AVS: Monosulfides like FeS, ZnS, ...
CRS: Disulfide (Pyrite; FeS_2) (Note that elemental sulphur, if present, will also be extracted!))
(Zhabina &Volkov, 1978; Canfield et al., 1986)

Chemicals:

- ethanol
- hydrochloric acid 25% (~ 8 M)
- chromium(III)chloride solution, 1 M
- silver nitrate solution, 0.1 M
- zinc acetate solution (4%) with acetic acid
- ammonia solution, 5%

Methods:

Preparation of different solutions

- 1 L chromium (III) chloride solution (1 M): weigh out 266 g $CrCl_3x6H_2O$ into a >1000 ml beaker and fill with deionised water up to 1000 ml.
- 1 L silver nitrate solution (0.1 M): weigh out 16.99 g $AgNO_3$ into a >1000 ml beaker and fill with deionised water up to 1000 ml.
- 1 L zinc acetate solution with acetic acid: dissolve 40 g zinc acetate in 100 ml H_2O, add 30 ml concentrated acetic acid, then fill up to 1000 ml with deionised water.
- 500 ml ammonia solution (5%): take 100 ml ammonia (25%ig) and fill up to 500 ml with deionised water

Reduction of chromium (III) chloride to chromous (II) chloride:

Add 450 ml of 1M chromium (III) chloride and 50 ml HCl (25%) into an Erlenmeyer flask together with a sufficient amount of granular elemental zinc (Zn^0). After one day, you should observe a colour change from green to blue.

Valence: $\overset{0}{Zn} + 2\,H\overset{+1}{Cl}\overset{-1}{} \rightarrow \overset{+2}{Zn^{2+}} + 2\,\overset{-1}{Cl^-} + \overset{0}{H_2}$ and

redox reaction:

Valence: $2\,\overset{+3}{Cr}\overset{-1}{Cl_3} + \overset{0}{H_2} \rightarrow 2\,\overset{+2}{Cr}\overset{-1}{Cl_2} + \overset{-1}{Cl^-} + 2\,\overset{+1}{H^+}$

redox reaction:

During the wet chemical extraction of different sulphur species, chromium (III) chloride will be the redox partner for pyrite (and elemental) sulphur. The sulphur will be reduced to sulphide that will ultimately form zinc sulphide.

Analytical set-up:

- weigh out the sample according to the (known) concentration of sulphide sulphur in the sample (the final yield should be 30 mg Ag_2S on the filter); record the weight
- place the sample powder into the round bottom flask (S extraction flask), add a magnetic stir bar
- add ca. 10 ml ethanol (acts as a catalyst)

- assemble all the glass ware (see figure 1):

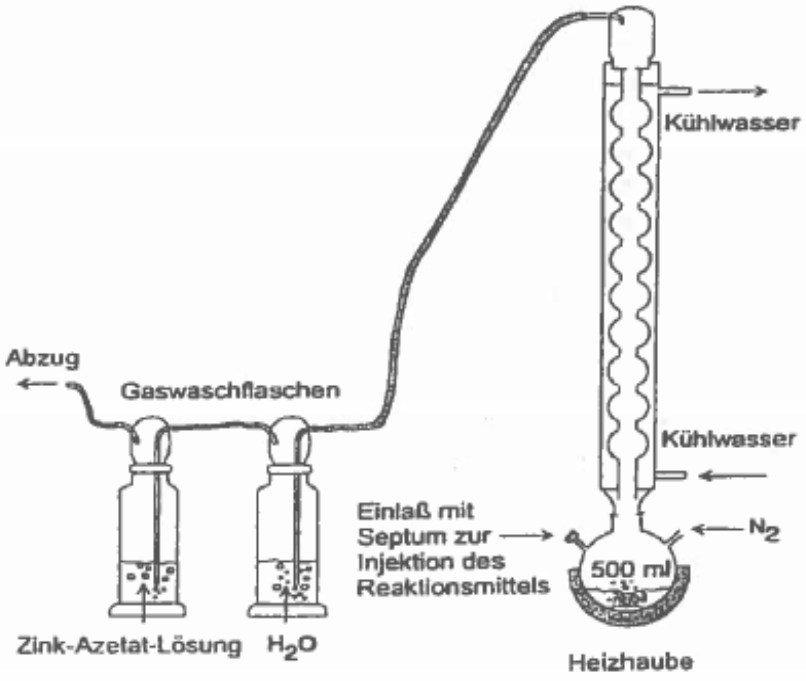

Fig 1: analytical set-up for wet chemical extraction of sulphur

- fill the first flask with deionised water (approx. half full)

- fill the second flask with zinc acetate solution (approx. half full)

- set up the glass ware accordingly; use water on the ground glass joints

- turn on the nitrogen flow (should be about 2 gas bubbles per second in the flasks) and wait for the system to be flushed (approx. 10 minutes; the systems need to be O_2-free!)

- eine Weile mit Stickstoff spülen, um 0_2 zu verdrängen

First step (AVS): liberation/removal of monosulphides (and carbonates):

- add ca. 20 ml HCl (25% = 8M) with a syringe though the septum (Caution: no HCl on the heating mantle, electrical problems!!!)

- let the reaction proceed for one hour at room temperature; in case the sample contains abundant carbonate, you may have to add more HCl

During the reaction, acid volatile sulphides (like FeS, ZnS, ...) will be liberated from the sample as hydrogen sulphide. This will pass the first flask with deionised (any acid fumes will be collected here). The hydrogen sulphide will be transferred to the second flask containing the zinc acetate solution. Here, hydrogen sulphide will be precipitated as zinc sulphide (forms a while precipitate, somewhat milky colour in the liquid). Please note that the zinc acetate will precipitate at the tip of the glass tube if there is only little sulphide in the original sample.

- When the reaction is finished, transfer the entire content of the second flask (including the zinc sulphide precipitate) into a beaker. Rinse the flask with deionised water. If some precipitate covers the tip of the glass tube, use a small wire to remove this and add it to the solution. Be rather meticulous as the sulphide yield will be calculated!

- Add 10 ml of 0.1 M silver nitrate solution to the beaker with the solution and the white precipitate. Silver sulphide (Ag_2S) will precipitate and the solution turns black (finely disseminated microcrystalline silver sulphide). Place the beaker with the black solution onto a heating plate and heat until it starts boiling. The finely disseminated silver sulphide will coagulate and can subsequently be filtered more easily. Remove from the heating plate and let it cool prior to filtration.

- Precipitate will be filtered (use a pre-weighed 0.45 micron cellulose nitrate filter) using a filtration device and a membrane pump. After filtration, rinse the precipitate with 10 ml ammonia solution (5%) and plenty of deionised water. Place the filter with the precipitate in a plastic petri dish and place into the drying oven (45°C). Once dry, weigh out the filter with your precipitate, determine the yield of silver sulphide and calculate the sulphur abundance. Record all weights.

For the second step (CRS): liberation of chromium reducible sulphur:

Rearrange the analytical set-up (basically new flasks). The sample is still in the round bottom flask, but the AVS has been extracted already and carbonate has been removed as well.

- Prepare the two flasks again; the first one with deionised water, the second one with zinc acetate solution.

- Adjust the nitrogen flow if necessary.

- Turn on the circulation cooler.

- Add ca. 30 ml of chromous (II) chloride solution using a syringe (again, avoid "colouring" the heating mantle).

- Turn on the heating mantle so that the solution almost starts to boil (ca. bei 85°C; level 2 at the heating mantle)

During the reaction, chromium reducible sulphur (FeS_2, but also elemental S) will be liberated from the sample as hydrogen sulphide. This will pass the first flask with deionised (any acid fumes will be collected here). The hydrogen sulphide will be transferred to the second flask containing the zinc acetate solution. Here, hydrogen sulphide will be precipitated as zinc sulphide (forms a while precipitate, somewhat milky colour in the liquid). Please note that the zinc acetate will precipitate at the tip of the glass tube if there is only little sulphide in the original sample.

Calculating the starting weight of your sample for the sequential sulphur extraction

For the routine EA-IRMS measurements, we need approximately 0.2 mg Ag_2S (180-230µg). Since we routinely perform duplicate runs, 0.4 mg Ag_2S is needed. However, so little sample is difficult to scrape off a filter. The goal is to obtain approximately 30 mg of Ag_2S.

M Ag: 108 g/Mol
M S: 32 g/Mol
M Ag_2S: 248 g/Mol → 32/248 = 0129 = factor

$$\Rightarrow \frac{\frac{M_S}{M_{Ag_2S}} \cdot M_{yield}}{\underbrace{10 \cdot wt\%S}_{mg/g \text{ to get mg yield}}} = M_{weigh\text{-}in}$$

→ 30 mg Ag_2S x 0.129 = 3.87mg S (in 30 mg Ag_2S)

Result from CS-Mat analysis: e.g. 2 wt.-% S x 10 = 20 mg S / g sample

Calculation: 1 g Probe – 20 mg S
x g Probe – 3.87 mg S → x = 0.2 g sample as starting weight for S-extraction

$0{,}129 \cdot A$ or $A = 30$ mg

$$\frac{3.87}{wt.\%\ S \times 10} = Y \text{ g starting weight for S-extraction}$$

$$Y = \frac{A \cdot \frac{S}{Ag_2S}}{10 \cdot wt\%} = \frac{mg}{mg/g} = g \qquad (A \text{ in mg};\ \frac{S}{Ag_2S} = 0{,}129)$$

Expected Yield: $A = \frac{10 \cdot wt\% \cdot Y}{0{,}129}$

If you anticipate significant amounts of monosulfide in addition to pyrite, take approximately twice a much sample powder.

During cleaning wash anything that has been in contact with Zn-Acetate/ZnS with HCl. This will remove remnants of S. Can be smelled as H_2S but may be invisible

Subsequent extraction of water soluble/acid soluble sulfate (precipitation of sulfate) and of organically bound (i.e. kerogens bound)

(Eschka* – ASTM 1970, 1977)

Following the liberation/extraction of AVS and CRS, the round bottom flask contains the green chromium chloride solution and the remaining sample powder. The solution contains acid soluble sulphate, the sample powder contains organically bound sulphur.

In order to prepare these two fractions, the content of the round bottom flask will be passed through a paper filter. This will separate the solids from the solute. Rinse with plenty of deionised water in order to remove acid residue and the dissolved sulphate from the solid sample powder. Place the paper with the sample powder into a drying oven (40°C).

The (green) solute will be filtered again through a cellulose nitrate filter (0.45 micron membrane filter). From this solute, the dissolved sulphate will be precipitated as barium sulphate using a $BaCl_2$ solution (8.5%).

- place the beaker with green solute on a heating plate and heat just below boiling
- add ca. 30 ml $BaCl_2$ solution
- heat to boiling, then keep the solution warm (70°C) for additional two hours (this way, barium sulphate crystals grow bigger and are easier to filter off), then cool down prior to filtration
- filter off $BaSO_4$ precipitate using a pre-weighed cellulose nitrate filter (0,45 micron)
- place filter with precipitate in drying oven (40°), when dry, weigh out and calculate the yield.

From the solid residue (sample powder), organically bound sulphur (OBS) can be extracted using Eschka reagent (OBS will be oxidized to sulphate).

- place the dry sample residue (from previous AVS/CRS extraction) into a porcelain beaker, mix it with Eschka (1:3) and cover the mixture with additional Eschka
- place the porcelain beaker into the muffel furnace for 2.5 hrs. at 800°C (initially, increase the temperature every 15 min by 200°C up to 800°C, then keep at this temperature for additional 90 minutes), then cool down
- remove the cold mixture from the porcelain beaker into a glass beaker, add 200 ml of hot deionised water, stirr well; after 45 minutes filter it off through a paper filter and rinse well with warm water; collect the solute that contains the dissolved sulphate of interest
- bring the filtrate to a pH <2, using HCl. Caution: after the Eschka treatment, the initial pH is approx. at 14! Carefully add the HCl, but a significant volume is necessary.
- filtrate the solute through a membrane filter (0,45 micron)
- place beaker with solute on a heating plate and heat just below boiling
- add 30 ml $BaCl_2$ solution
- heat to boiling, then keep the solution warm (70°C) for additional two hours (this way, barium sulphate crystals grow bigger and are easier to filter off), then cool down prior to filtration
- filter off $BaSO_4$ precipitate using a pre-weighed cellulose nitrate filter (0,45 micron)
- place filter with precipitate in drying oven (40°), when dry, weigh out and calculate the yield.

* Eschka : strong oxidant, mixture comprising 65% MgO and 35% Na_2CO_3

Thode-Extraction for sulphates (Thode et al., 1961)

Thode solution:	500 ml HI (57%ig)	or	250 ml HI
	816 ml HCl conz.		408 ml HCl conz.
	245 ml H_3PO_2 (50%ig)		122,5 ml H_3PO_2

thoroughly mix all volumes and boil for 45 minutes

zinc acetate acetic acid (Sasaki et al.): dissolve 40 g zinc acetate in 100 ml deionised water add 30 ml concentrated acetic acid and fill up to 1000 ml

The analytical set-up (glassware) is identical to the one used for the AVS/CRS extraction. However, use separate round bottom flasks specifically labeled „Thode"

Amount of sample material: 10 – 20 mg of $BaSO_4$

Analytical procedure:

0. NO ETHANOL in the beginning!
1. Set-up glass flasks as previously described, i.e. the first flask after the extraction is half filled with deionised water, the second one with zinc acetate solution.
2. turn on the circulation cooled
3. add a magnetic stirring bar to the round bottom flask with your sample powder
4. check all connections and joints
5. flush the entire set-up sufficiently long with N_2
6. add 30 ml Thode solution to each sample using a syringe
7. slowly stir the mixture with the stirring bar; turn on the heating mantle at level 2
8. let the reaction proceed for 3 hrs., then the reaction should be complete
9. after three hours, remove the second flask (the zinc acetate trap now containing the zinc sulphide precipitate) from the set-up, transfer the solute and precipitate into a glass beaker
10. add 10 ml $AgNO_3$, heat up the solution to boiling in order to have the silver sulfide co-agulate; then take the beaker off the heating plate and let it cool prior to filtration
11. record any unusual observations, e.g., a colour other than black
12. once cooled off, filter off (0.45 micron cellulose nitrate membrane filter) the silver sulphide precipitate, rinse with ammonia solution (5%) and carefully wash with deionised water afterwards
13. place the filter into the drying oven (45°C)
14. when dry, weigh out the filter, calculate the silver sulphide yield

Extraction of elemental S with acetone

(Zhabina &Volkov, 1978; Rice et al., 1993)

- place the sample powder into a PE bottle and mix with acetone (ca. 10 g sample in 100 ml acetone)

- shake the sample – acetone slurry for 18 hrs.

- filter the sample, initially using a paper filter; subsequently utilize a Whatman GF/F filter

- transfer the filtrate (solute) into the round bottom flask fort he sulfur extraction, add a stirr bar, turn on heater and magnet stirrer, and vapourize the acetone until it is nearly dry; then cool down the round bottom flask (it should never dry up completely as this might cause loss of elemental sulphur)

- assemble the extraction set-up as usual and flush the system with nitrogen

- add chromous (II) chloride and the reaction will proceed just like for the CRS fraction

If the sample potentially contains elemental sulfur, then this would be the first step in the sequential sulfur extraction. Hence, following the acetone extraction, the reaction can now proceed as previously described, i.e. followed by AVS and subsequently CRS and OBS extractions.

Filter zerstören

In those cases, where limited sample material and/or limited silver sulfide yields are encountered, the cellulose nitrate filter can be destroyed in order to obtain the silver sulphide for an isotope measurement

for $BaSO_4$: destroy (ash) the filter at 500 °C for 1 hour in the muffle furnace

for Ag_2S: place the filter with the silver sulfide precipitate in a Falcon tube (centrifuge tube) and add 10 ml of acetine. Shake well which will completely dissolve the filter paper. Place the Falcon tube in a centrifuge, spin down and decant (or use a pipette) the acetone. Repeat the process. Finally, take up the silver sulfide residue with water, transfer it into a small glass vial and place the vial into the drying oven. When the water has evaporated, the silver sulphide can be taken from the glass vial and subjected to an isotope measurement.

XVIII: Appendix H: Original Sample Names and Core Information

Sample name in this study	Original sample name	Core	Core depth (m)
GAS S1	GAS box 31 GS-1	GASESA-1	181
GAS S2	GAS box 33 GS-2	GASESA-1	195.3
GAS S3	GAS box 34 GS-3	GASESA-1	202
GAS S4	GAS box 35 GS-4	GASESA-1	204.8
GAS S5	GAS box 36 GS-5	GASESA-1	211.35
GAS S6	GAS box 36 GS-6	GASESA-1	212.2
GAS S7	GAS box 37 GS-7	GASESA-1	216.3
GAS S8	GAS box 40 GS-8	GASESA-1	239.2
GAS S9	GAS box 40 GS-9	GASESA-1	239.4
GAS S10	GAS box 42 GS-10	GASESA-1	247.6
GAS S11	GAS box 43 GS-11	GASESA-1	255
GAS S12	GAS box 43 GS-12	GASESA-1	255.1
HEX S1	HEX-5 S5 -o top B. shale (Adj. to stromatolites)	HEX5	705 *
HEX S2	HEX-5 S4	HEX5	708.3
HEX S3	HEX-5 S3	HEX5	914
ARP S1	ARPAN S2	AARPAN5	534.4
ARP S2	ARPAN S1	AARPAN5	570.2
ARP S3	ARP S1	AARPAN5	669.27-669.31
ERI S1	ERIN BS, 8.60m below diamictite contact	ERIN03	375 *
ERI S2	ERIN S5	ERIN03	414.8
MP53	MP53 Black shale in BIF	Middelplaats	???

* Samples indicates with this symbol had no associated depth and therefore depths were estimated.

No sample depth was provided for sample MP53. It was sampled from the Hotazel formation, where it was part of a shale layer located directly below the uppermost of three thick manganese-rich layers (H. Tsikos, personal comm.).

Statement of originality of the MSc thesis

I declare that:

1. this is an original report, which is entirely my own work,

2. where I have made use of the ideas of other writers, I have acknowledged the source in all instances,

3. where I have used any diagram or visuals I have acknowledged the source in all instances,

4. this report has not and will not be submitted elsewhere for academic assessment in any other academic course.

Student data:

Name: AART (A.R.W.) van der Waal

Registration number: 3866874

Date: 10-03-2016

Signature: